NONLINEAR OPTICAL SPECTROSCOPY WITH ULTRAFAST LASER PULSES AND CONTROLLING LASER-MATTER INTERACTIONS

By

Gennady Rasskazov

A DISSERTATION

Submitted to
Michigan State University
in partial fulfillment of the requirements
for the degree of

Chemistry – Doctor of Philosophy

2017

ABSTRACT

NONLINEAR OPTICAL SPECTROSCOPY WITH ULTRAFAST LASER PULSES AND CONTROLLING LASER-MATTER INTERACTIONS

By

Gennady Rasskazov

The goal of my dissertation work was to study nonlinear laser-matter interactions and to obtain a better understanding of the various processes occurring during these interactions. Advances in femtosecond laser technology have become widely adopted in a nonlinear laser spectroscopy and photochemistry. With the extreme temporal and spatial confinements it becomes possible to induce nonlinear responses of the material and to study them with high temporal resolution. The complexity of the medium response to the excitation field necessitates control the excitation process in order to figure out its origin, for example, inter-or intra-molecular dynamics. Therefore, over the last two decades, femtosecond pulse-shaping methods have been developed to reach an unprecedented level of control over the ultrafast laser waveforms where spectral amplitude and phase can be specified in accordance to expected response. The characterization and tailoring of femtosecond pulses was central for my research projects.

Experimental results are presented in three chapters. Chapter 2 focuses on two topics: (1) generation of flat top temporal shape pulses with sharp on and off fronts and no loss of spectral bandwidth for particular spectroscopic applications; (2) characterization of noisy ultrafast laser sources, namely, pulse-to-pulse stability, caused by spectral phase or amplitude noise. Chapter 3 presents the fundamentals of Raman spectroscopy and development of a non-contact no-reagents system operating in the eye-safe 1600-1800 nm wavelength range for standoff trace detection of explosives and high-speed imaging, 0.06 ms per pixel. The system used in this project is based on the latest ideas in coherent Raman spectroscopy and technologies to perform selective coherent vibrational excitation of a particular chemical compound with sensitivity of sub-$\mu g/cm^2$. Chapter 4 describes time-resolved transition-state spectroscopy of sodium iodide (NaI) by taking advantage of modern lasers and pulse shaping to better

map the low-lying electronic states. High-level ab initio multi-reference configuration interaction and density matrix calculations were used to simulate time dependent wave packet dynamics of NaI pumped to the A 0^+ state.

The results in this dissertation demonstrate the utility of tailored ultrafast laser pulses. Using advanced laser technology and photonic control methods we gain a better understanding of time-resolved dynamics of a chemical reaction and nonlinear spectroscopy. During my work I got to develop new approaches for characterization of the laser source itself and how to tailor it using pulse shaping. The work presented here should serve future studies on nonlinear laser-matter interactions with a novel photonic control schemes.

ACKNOWLEDGEMENTS

I remember the moment when I was introduced for the first time to one of the best public colleges in the United States, Michigan State University (MSU), and the outstanding Dantus Research Group by my advisor Prof. Olga Smirnova at Bauman Moscow State Technical University. Since that time until now, I could not have asked for a better graduate school experience. I would like to thank her for the substantial support, care, and encouragement to have such a great opportunity in my life.

I would like to thank my advisor at MSU, Prof. Marcos Dantus, for giving me a chance to work in a world-class laboratory with modern, top-notch equipment. I am grateful for his tremendous support, time and experience, which saved me a lot of time in the lab and always brought me closer to my goal. I learned from him how to work on a tight deadline, how to stay focused and think strategically to successfully finish all the requirements, and how to think "big picture". He is a great teacher, not only in science, but in life too. I will always remember his lessons, critical thinking, and optimism.

During my graduate career I have been fortunate to be surrounded by great people and I would like to thank all former and current members of the Dantus Research Group with whom I had the honor to work: Dr. Marshall Bremer, Dr. Bai Nie, Dr. Arkaprabha Konar, Dr. Alexander van Rhijn, Dr. Rachel Glenn, Dr. Christopher Mancuso, Dr. Nagitha Ekanayake, Muath Nairat, Orin Yue, Jay Shah, and Soumen Ghosh. You were very helpful in answering all the questions I had in chemistry, physics, lasers, optics and other fields. Many thanks to my lab mates Dr. Anton Ryabtsev and Dr. Ilyas Saytashev. I am very grateful to have such good friends like them. Special thanks go to Dr. Vadim Lozovoy, a great theoretician and teacher, for his lessons, ideas, and care. I would like to thank Dr. Dmitry Pestov for all his insights into the nuts and bolts of ultrafast lasers and for all our collaborative projects.

I would like to acknowledge our collaborators from Cornell University, Prof. Chris Xu, Kriti Charan, and Tianyu Wang. Thank you for your dedication and hard work in the lab, which resulted in publication.

I would like to thank my committee members: Profs. Gary J. Blanchard, Warren W. Beck, and Benjamin G. Levine for their suggestions and interesting scientific discussions during my graduate education.

Last, but not least, I would like to thank my family: grandparents, parents, sister, wife and my daughter for their great support, dedication and for believing in me.

TABLE OF CONTENTS

LIST OF FIGURES

KEY TO ABBREVIATIONS

ANSI	American National Standard for Safe Use of Lasers
BS	Beam splitter
CARS	Coherent anti-Stokes Raman scattering
CASSCF	Complete active-space self-consistent field
CPA	Chirp pulse amplification
CW	Continuous waveform
ECP	Effective core potential
EM	Electromagnetic
FC	Franck-Condon
FEL	Free-electron laser
FFT	Fast Fourier-transform
FLASH	Free Electron LASer in Hamburg
FROG	Frequency resolved optical gating
FTS	Femtosecond transition state
FWM	Four-wave mixing
FWHM	Full-width half-maximum
GDD	Group delay dispersion
GVD	Group velocity dispersion
HWG	Hollow core waveguide
IMS	Ion-mobility spectrometry
IR	Infrared
KDP	Potassium dideuterium phosphate
LCOS SLM	Liquid crystal on silicon SLM
LC SLM	Liquid crystal SLM

LIBS	Laser induced breakdown spectroscopy
LMA	Large mode area
MEM	Maximum entropy method
MIIPS	Multiphoton intrapulse interference phase scan
MRCI	Multireference configuration interaction
NLC	Nematic liquid crystals
OD	Optical density
OKE	Optical Kerr effect
OPCPA	Optical parametric chirped-pulse amplification
OR	Optical rectification
OSA	Optical spectrum analyzer
PBS	Polarizing beam splitter
PEC	Potential energy curves
PES	Potential energy surface
QC	Quantum cascade
SA	State-averaged
SESAM	Semiconductor saturable absorber mirror
SHG	Second-harmonic generation
SLM	Spatial light modulator
SO	Spin-orbit
SOD	Second-order dispersion
SPIDER	Spectral phase interferometry for direct electric-field reconstruction
SPM	Self-phase modulation
SRS	Stimulated Raman scattering
TATP	Triacetone triperoxide
TBP	Time-bandwidth product

THG	Third-harmonic generation
THz	Terahertz
TL	Transform-limited
TOD	Third- order dispersion
UV	Ultraviolet
XFEL	X-ray free electron laser
ZDW	Zero-dispersion wavelength

Chapter 1 Introduction

Since the development of the first laser system in 1960 [1] a new era in light-matter interactions began. Lasers became the most practical tool in many scientific, industrial, and everyday applications. For instance, searching the word “Laser” in the Web of Knowledge reveals more than 860,000 publications. In particular, lasers helped to advance scientific disciplines such as chemistry and physics: from studying atomic structure to the investigation of complex dynamics of matter in different states as a result of interaction with electromagnetic waves. According to the Bohr model, each atom is comprised of a nucleus surrounded by electrons that move around the nucleus in a well-defined set of energy orbitals. This intrinsic property allows for the identification of not only atoms but molecules as well. Under normal conditions an atom is found in the ground state, which is the most stable state where all electrons occupy the closest orbitals to the nucleus. By absorbing some quantum of energy, an electron can move to another allowed orbital. It stays there for some time and then relaxes back to the ground state by emitting a photon with an energy corresponding to the energy difference between the excited and ground states. This energy-level spacing defines a unique quantization of vibrational and rotational degrees of freedom in a specific system. By knowing these levels one can make a conclusion about molecular structure including chemical bond lengths in a molecule [2]. The first spectroscopic experiments carried out by R. Bunsen and G. Kirchhoff were based on the excitation of individual narrow energy levels of elements using tunable monochromic light. Those cases correspond to stationary states, for which momentum and position does not change with time.

Pulsed lasers opened new possibilities to study time-resolved dynamics of systems directly, since more than one eigenstate can be simultaneously populated by a sufficiently short pulse [3]. The idea to capture fast motions came to E. Muybridge in the 19^{th} century, where he used a fast shutter to decrease the exposure time in a photographic film camera. In other words, to obtain a time-resolved picture the shutter should work much faster than the time needed for the object to move a distance considerably smaller than its size. For example, in order to freeze a hummingbird’s wings $\sim 5 \cdot 10^{-5}$ s resolution is

required, and in order to study quantum gravitational effects one needs to have resolution as small as Planck time: $5.39 \cdot 10^{-44}$ s [4]. In chemistry, biology, and physics several processes occur at fundamental timescales defined by the spacing between their quantum energy levels; see Figure 1. The x-axis here is time, and gives us an understanding of how fast the various processes occur. The first observation of intermediates of chemical reactions, with microsecond time resolution, was accomplished by R. G. W. Norrish and G. Porter in 1949 [5]. The chemical intermediates observed then were long lived when compared to the fundamental timescales for bond cleavage and formation. Those timescales can be estimated through knowledge of vibrational periods. Therefore, it was known that capturing the fundamental chemical bond processes would require pulses that were 10-100 fs in duration (1 fs = 10^{-15} s). Approximately forty years later, the process of bond cleavage was finally observed using femtosecond lasers [6] and fifty years later in 1999 the Nobel Prize was given to A.H. Zewail for the real-time observation of dynamics of chemical reactions based on unimolecular photodissociation [6-8].

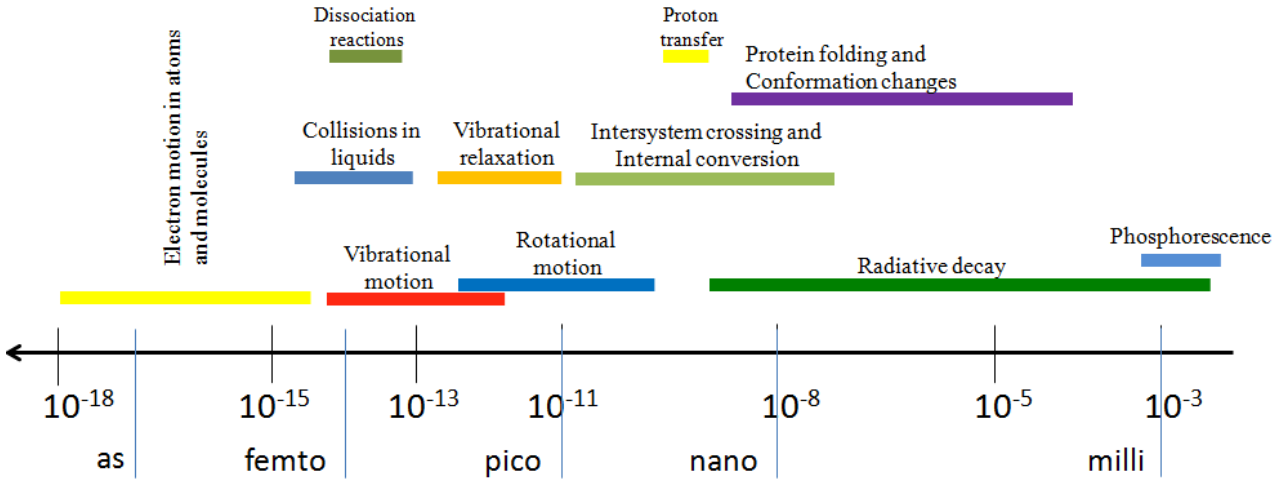

Figure 1. Time scales for typical processes in physics, chemistry, and biology.

Towards the end of the last century significant steps were made in laser development that allowed for the routine generation of sub-10 fs pulses using solid-state Titanium-doped sapphire (Ti:Sapphire) lasers [9]. Lasers became indispensable tools in science. More recently, the previously inaccessible regimes of light-matter interaction, such as electronic processes, became possible with the invention of

attosecond (1 as = 10^{-18} s) lasers systems in 2001 [10, 11]. Generation of attosecond pulses proceeds through the reliable preparation of intense femtosecond laser pulses. Therefore, some work in this thesis may prove useful in attosecond science.

Compressing broadband laser pulses to their shortest possible duration and having control over the pulse waveform became crucial for discovering new properties of matter through the interaction with light. The compressibility of a laser pulse given its spectral bandwidth is governed by the Heisenberg uncertainty principle. The length of a pulse profile without spectral phase distortions is defined by its spectral components. Therefore, in order to investigate spectroscopic studies on the timeframes mentioned above, see Figure 1, the laser pulses have to satisfy the following requirement:

$$\Delta E \Delta t > \frac{\hbar}{2}, \tag{1}$$

where ΔE and Δt are the uncertainties for the energy and time respectively, and $\hbar$ is Plank's constant. In accordance with the uncertainty principle, the shorter the pulse, the broader the energy spectrum. These two physical quantities are related to each other through a Fourier transformation. From quantum mechanics' point of view, longer pulses can individually probe energy levels, but shorter pulses can catch the quantum dynamics, namely the dynamics of the superposition of rotational and vibrational energy states. The frequency-time uncertainty relation can be rewritten as follows:

$$\Delta t \Delta \nu \cong TBP, \tag{2}$$

where $\Delta \nu$ is the spectral width and TBP is a time-bandwidth product which is different for different transform-limited (TL) pulses. The $\Delta \nu$ can be rewritten as $c\Delta \bar{\nu}$, where c is the speed of light, $\Delta \bar{\nu}$ is the spectral bandwidth measured in cm^{-1}. For example, a Ti:Sapphire laser system producing Gaussian pulses (TBP = 0.44) on the order of femtoseconds, ~ 5 fs, [12] possesses a ~3000 cm^{-1} bandwidth. This bandwidth can greatly enhance the capabilities of spectroscopic and imaging applications such as coherent Raman spectroscopy or two-photon fluorescence microscopy because it overlaps the entire relevant range of vibrations in chemistry [13, 14]. Combining this laser with a pulse shaper enables it to perform selective excitation [15, 16].

Another advantage of modern ultrafast lasers is the ability to deliver a precisely timed electric field with a magnitude which can easily generate a nonlinear response in matter or even exceed the strength of the electron binding field, which in a hydrogen atom is ~ 10^{11} V/m [17]. Such a strong field can modify the potential energy surface (PES) and may act as a catalyst of chemical reactions by favoring a specific pathway [18, 19].

Thus, an ultrashort laser source is a very unique and versatile tool, which facilitates the study of different fundamental phenomena occurring during the light-matter interaction and also provides deep insights into the structure and properties of the matter. This thesis focuses on gaining a better understanding of nonlinear optical processes and how to control them by using adaptive pulse shaping.

1.1 Generation of ultrashort pulses

A high-power source of coherent and broadband light is the basic tool of nonlinear laser spectroscopy. In order to generate these pulses, there are a few methods which can be utilized such as mode-locking [20, 21], gain-switching [22], and pulse compression [23]. The latter requires a coherent laser pulse. In all of my research projects I have been working with mode-locked laser sources with passive stabilization schemes known as Kerr-lens mode-locking [24, 25] or a semiconductor saturable absorber mirror (SESAM) [26]. It is known that mode-locking is achieved when there is a fixed phase relationship between the allowed longitudinal modes, *n*, inside the laser cavity, see Figure 2(a). The superposition of longitudinal modes causes the formation of pulses which are shown in Figure 2(b). The collection of longitudinal modes determines the laser pulse spectral bandwidth, see Figure 3(a). In the case of a transform-limited pulse, the corresponding time profile is given in Figure 3(b). The electric field of the pulse in the frequency domain can be written as:

$$E(\omega) = \sum_{n=1}^{N} E(\omega_n) \exp(-i\varphi(\omega_n)), \tag{3}$$

where $E(\omega_n)$ and $\varphi(\omega_n)$ are the magnitude and phase of the nth longitudinal mode, respectively. For broadband laser pulses, such as in femtosecond lasers, the phase relationship between the different modes

plays a crucial role in mode-locking. The output parameters of the laser system can be deteriorated with the presence of high order phase distortions within the cavity as well as outside the cavity. In order to avoid such effects, phase compensation techniques are required.

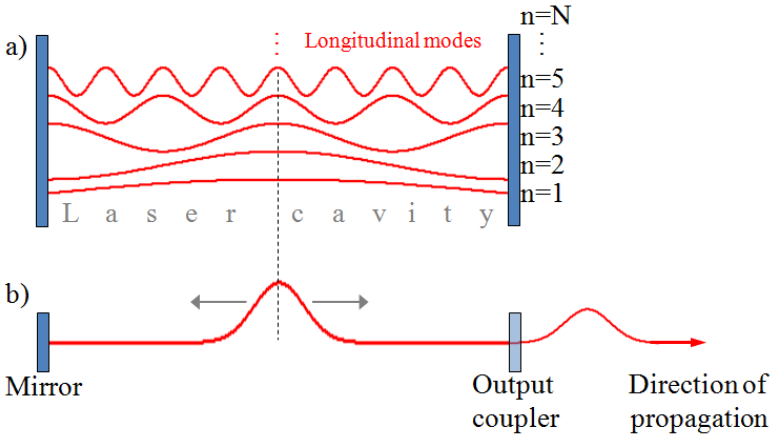

Figure 2. Mode-locking mechanism. (a) Laser cavity and its allowed longitudinal modes, *n*=1...*N*. (b) Intensity profile of the pulse formed from constructive interference between all modes.

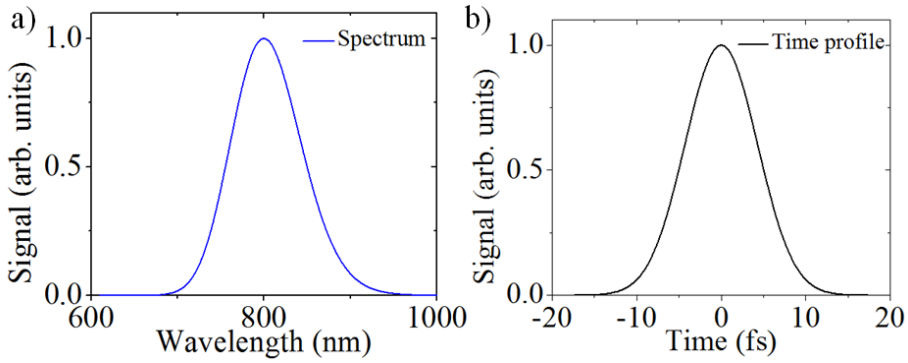

Figure 3. Laser spectrum (a) and corresponding transform-limited time profile (b) of the 10fs laser pulse measured at full-width half-maximum (FWHM).

The spectral phase of the laser pulse can be expanded in a Taylor series:

$$\varphi(\omega) = \varphi_0 + \frac{\varphi'(\omega_0)}{1!}(\omega-\omega_0) + \frac{\varphi''(\omega_0)}{2!}(\omega-\omega_0)^2 + \frac{\varphi'''(\omega_0)}{3!}(\omega-\omega_0)^3 + \ldots + \frac{\varphi^n(\omega_0)}{n!}(\omega-\omega_0)^n, \qquad (4)$$

where φ_0 is a constant phase, $\varphi'(\omega_0)$ is a group delay, $\varphi''(\omega_0)$ is a second-order dispersion (SOD, also known as chirp), $\varphi'''(\omega_0)$ is a third- order dispersion (TOD), and $\varphi^n(\omega_0)$ is a *n*-order dispersion. The influence of individual spectral phase components on the temporal pulse profile is presented in Figure 4.

A 10 fs FWHM pulse duration was used for the numerical simulation. The case in Figure 4(a) shows an electric field instead of an intensity profile. A demonstration of the effect of a constant phase shift can be seen in Figure 4(b). Figure 4(c) and (d) show the group delay effect, Figure 4(e) and (f) show the chirp effect, and Figure 4(g) and Figure 4(h) show the TOD effect on pulse temporal profile.

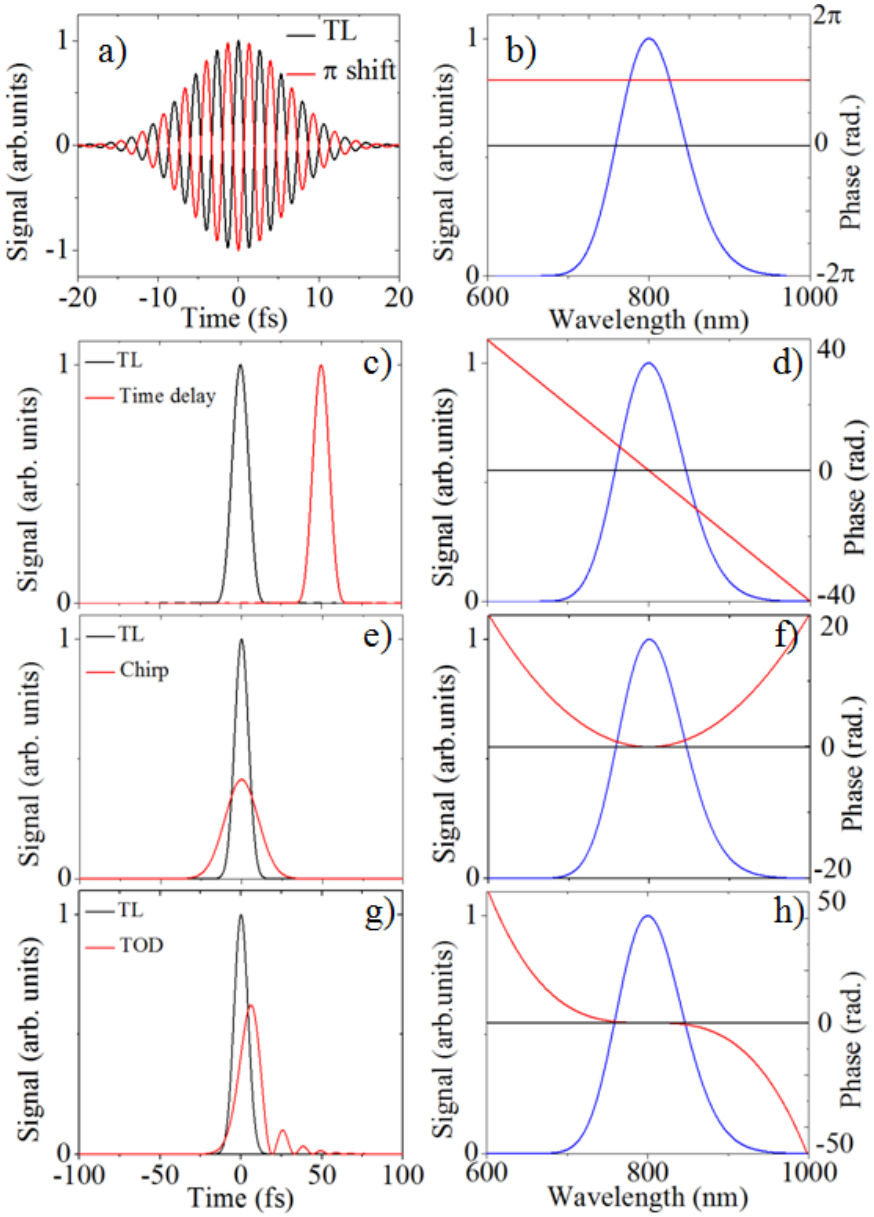

Figure 4. Numerical simulation. The influence of spectral phase on the temporal pulse profiles. The left column shows the temporal domain with and without phase distortion, the right column shows the corresponding laser spectrum and spectral phase distortions. For the simulation, the pulse duration was set to 10 fs. (a) and (b) show the case for a constant phase shift of π. (c) and (d) show the case for a group delay of +50 fs. (e) and (f) show the case for a chirp of 80 fs^2. (g) and (h) show the case for a TOD of +1000 fs^3.

1.2 Material dispersion and group velocity dispersion

Material dispersion is an intrinsic property of a medium, and defines the phase velocity of each spectral component (λ) in the laser pulse. If the ratio $dn/d\lambda$ is less than zero then the medium is considered to have normal dispersion, meaning that the index of refraction, *n*, decreases with increasing wavelength. In a normal dispersion medium, the laser pulse gains positive chirp and the opposite is true for anomalous dispersion. In the positively chirped pulse the low frequency components travel faster than the high frequency components, see Figure 5. Since an ultrashort laser pulse has a broad bandwidth, material dispersion distorts the temporal profile of the pulse, stretching it in time and reducing the peak power due to group velocity dispersion (GVD). The GVD is proportional to the second derivative of the index of refraction with respect to the wavelength [27].

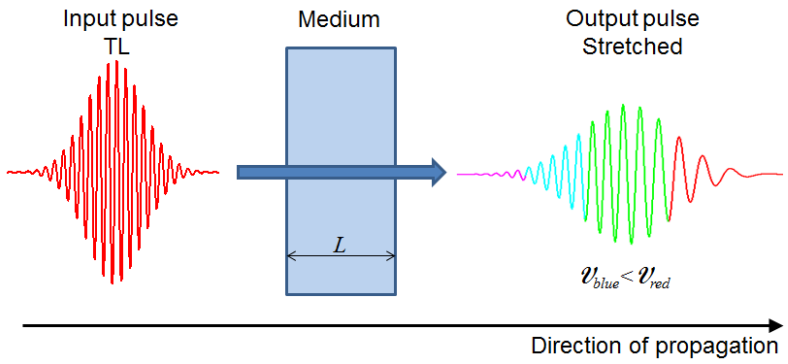

Figure 5. Dispersion of the medium with length *L* causes pulse broadening. v_{blue}, v_{red} are the speeds of blue and red wavelength, respectively.

1.3 Phase compensation techniques

Dispersive effects are usually the limiting factor in systems where short pulses are used. Even propagation through the air can effect the pulse duration. For example, a transform-limited pulse with 10 fs pulse duration at FWHM and central wavelength at 800 nm will be stretched to 55 fs at FWHM after propagating 10 meters in air. For applications which require the shortest pulse width at the target, pulse compression needs to be implemented. The intrinsic nature of pulse compression is to rearrange the phase of individual spectral components to minimize the pulse duration [23].

There are a number of methods for temporal compression of optical pulses, such as a pair of prisms or gratings, chirped mirrors, or a fiber Bragg grating. The disadvantage of the last two techniques is the lack of flexibility, since they are designed to compensate for a specific dispersion profile. In a Ti:Sapphire oscillator (Micra, Coherent inc.), for example, intracavity dispersion is compensated by a prism-pair compressor [28]. The principle behind this approach is to use angular dispersion or the frequency-dependent index of refraction as the light propagates through a dispersive medium. The prism-pair introduces negative chirp, since the bluer frequencies undergo greater angles of refraction than the redder frequencies and, therefore, travel a longer distance inside the compressor, see Figure 6. After the second prism, Prism 2, spatially displaced and collimated frequencies are sent back along the same optical path by a reflectng mirror. This configuration is called a folded compressor, otherwise two more prisms need to be added symmetrically with respect to the first pair. In order to provide a uniform quadratic spectral phase for all the wavelengths, a low dispersion material is used.

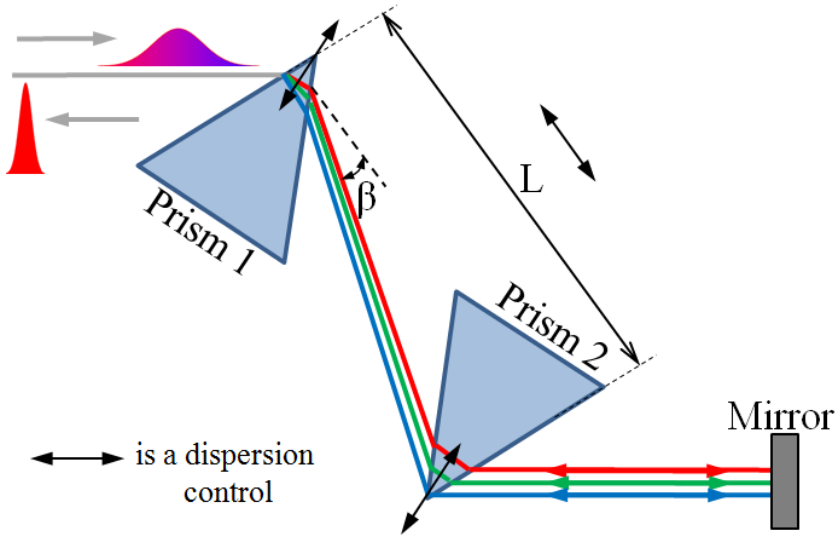

Figure 6. The prism-pair compressor in a folded configuration. The distance between the two prisms is *L*. The angle of the dispersed ray is β. Prism 1 disperses the beam, Prism 2 collimates the rays. Dispersion control is provided by varying the pathlength through the prisms or by adjusting the length, *L*.

To minimize the Fresnel reflection loss, the apex angle of each prism should be cut at Bruster's angle. Control over the chirp sign and magnitude is provided through changing the distance, *L*, between

the two prisms or by varying the pathlength through the prisms. The amount of chirp, or group delay dispersion (GDD) introduced by the prism-pair compressor can be calculated from the following equation [29]:

$$GDD \approx \frac{\lambda^3}{2\pi c^2}\left[-8\left(\frac{dn}{d\lambda}\right)^2 L\cos\beta + 4\left[\frac{d^2n}{d\lambda^2} + (2n - n^{-3})\left(\frac{dn}{d\lambda}\right)^2\right] L\sin\beta\right], \quad (5)$$

where λ is the wavelength, n is the index of refraction, L is the prism separation length, and β is the refraction angle. The first term is always negative whilst the second term is positive in the infrared (IR) and visible spectral ranges. The advantage of using a prism-pair is their low energy loss, but the disadvantages are a low dynamic range of the GDD control for a given laser cavity and the absence of flexibility in controlling higher orders of dispersion [21, 30].

On the other hand, a grating-pair compressor provides a larger dynamic range of control over the magnitude and sign of the GDD and TOD. However, its angular dispersion is strongly dependent on the groove spacing. The disadvantage of this compressor is considerably lower throughput than that of the prism-pair. In order to maximize the efficiency in a certain diffraction order, blazed gratings are used. The first optical grating-pair compressor was developed in 1969 [31] and since that time it has been used for many applications, in particular, chirp pulse amplification (CPA) systems [32]. The grating-pair compressor is shown in Figure 7. The principle behind its operation is similar to a prism-pair compressor; the incident light gets diffracted by Grating 1 at the angle, β_d, and collimated by Grating 2. After reflection from the mirror the rays travel the same distance back and get recombined by Grating 1. Most gratings, fabricated to be utilized in grating-pair compressors, operate in m= -1 order of diffraction, therefore they introduce negative dispersion. By varying the distance between the two gratings, L, one can compensate for initial dispersion of the laser pulse, see Figure 7.

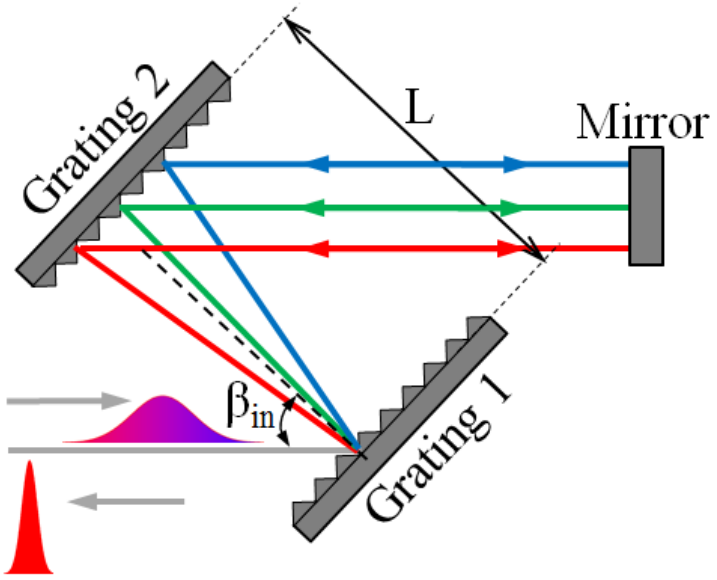

Figure 7. The geometry of a grating-pair compressor in a folded configuration. Grating 1 diffracts the beam at the angle β_d, Grating 2 collimates the rays. Dispersion control is provided by varying the distance between the two gratings, *L*.

The amount of GDD and TOD introduced by the grating-pair compressor can be calculated from the following equations [29]:

$$GDD = -\frac{m^2\lambda^3 L}{\pi c^2 d^2}\left(1-\left(\frac{\lambda}{d}-\sin\beta_{in}\right)^2\right)^{-\frac{3}{2}}, \tag{6}$$

$$TOD = -GDD\frac{6\pi\lambda}{c}\frac{\left(1+\frac{\lambda}{d}\sin\beta_{in}-\sin^2\beta_{in}\right)}{\left(1-\left(\frac{\lambda}{d}-\sin\beta_{in}\right)^2\right)}, \tag{7}$$

where d is the grating period, m is the diffraction order, β_{in} is the angle of incidence.

All the pulse compression techniques described above are, in their own way, elementary pulse shapers due to their dual nature in changing the pulse intensity profile, namely compressing or stretching the pulses by varying the spectral phase of the input pulse. Amplitude modulation is possible using a transmission mask located at the Fourier plane [33-35].

When complete control over the spectral phase and amplitude is required, then adaptive pulse-shaping techniques are used. Most of them utilize Fourier synthesis as a key principle. Here, a computer-controlled liquid crystal spatial light modulator (SLM) [36-40], an acousto-optic modulator [41], or a deformable mirror, located at the Fourier plane of a 4-f optical setup, are the pivotal components in the system [42]. A broad range of applications with adaptive pulse shapers include optical control of laser-matter interaction [43-45], laser pulse characterization and compression [46-52], and high-speed communication [53, 54]. As for my research projects, I have been extensively using SLM-based pulse-shapers, therefore it is worth elaborating on this technology.

The setup was initially conceived by Froehly [33] for picosecond (10^{-12} s) pulses. It consists of two diffraction gratings, two lenses, and a fixed transmission mask separated by one focal distance, *f*, see Figure 8. The lenses form a telescope with unit magnification. This condition guarantees a zero-dispersion configuration, provided that the mask is not present in the setup. The configuration is called a "4-*f* pulse shaper". In Figure 8, the incident light experiences angular dispersion after it bounces off the first grating. Then, the lens focuses spatially separated frequency components at the Fourier plane, where the transmission mask is placed. The mask may be composed of two masks: phase and amplitude. The phase mask can retard any of the frequency components whereas the amplitude mask regulates the magnitude of the field. The second lens collects and collimates all the spectral components and sends them to the second grating, which recombines them into a single beam.

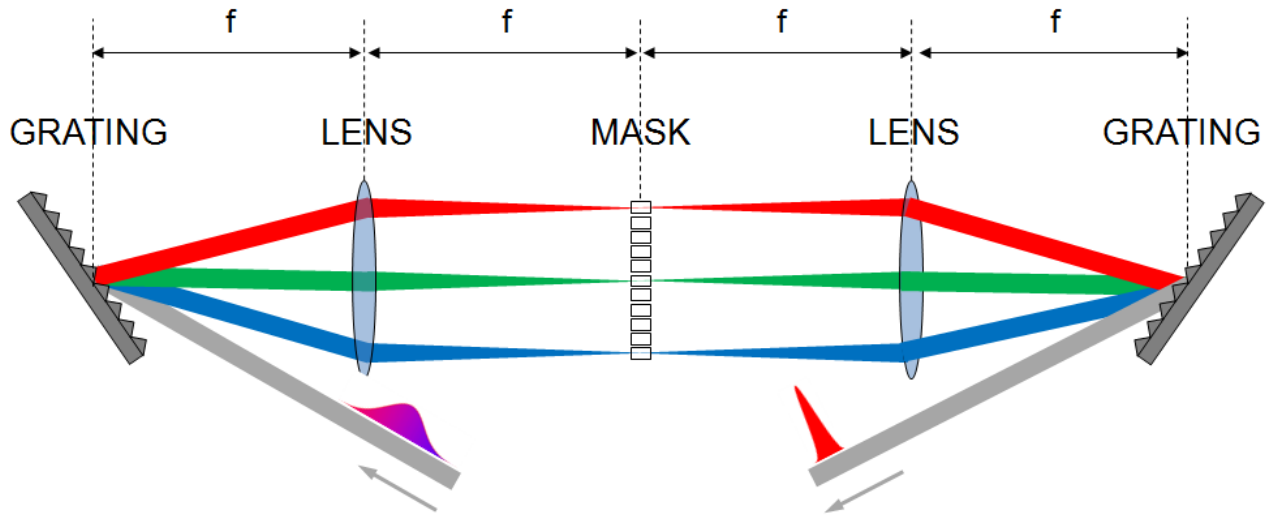

Figure 8. The 4-*f* pulse shaper with transmission mask in the Fourier plane. The output pulse is compressed to the transform-limited pulse duration.

Using a programmable pixilated mask, or SLM, instead of a fixed mask allows one to impose any user-defined phase and amplitude profiles and provides continuous variable control over the individual pixel. In many applications, for example in strong field ionization [55], it is required to have separate control over each term in the Fourier expansion of the phase, see Eq. (4). There are two types of SLM used in my research projects. The first one is a liquid crystal SLM or LC SLM. The second one is a liquid crystal on silicon SLM or LCOS SLM. Both devices are made of nematic liquid crystals (NLC) sandwiched between two electrodes which establish a pixel. The typical LC SLM and LCOS SLM have 128 or 640 and 800×600 pixels respectively. When an electric field is applied, the liquid crystal molecules tilt, causing an index of refraction change. For complete phase control a phase change of 2π is required. For LC SLM and LCOS SLM the modulation of light with respect to phase and amplitude occurs in either transmission or reflection regimes, respectively. The maximum performance of the pulse shaper at a given number of SLM pixels strongly depends on the number of pixels covered by the spectrum and the focusing spot size of the single frequency in the Fourier plane, provided that all the components are optimized to work in the particular spectral region. The more pixels used, the higher the dynamic range of phase variation, and the smaller the focal spot, the less amount of light is diffracted out from the spacing between the pixels.

The multiphoton intrapulse interference phase scan (MIIPS) algorithm, developed by the Dantus Research Group, allows one to characterize and compensate phase distortions of any complexity in a laser pulse [50, 56-59]. MIIPS is a self-referenced method that takes advantage of the inherent sensitivity of a non-linear optical signal, such as second-harmonic generation (SHG), to measure and compensate phase distortions. The method collects the spectrally resolved nonlinear optical signal and tracks the position of its local maximum as a function of a single scan parameter of the calibrated reference phase. The second derivative of the phase is then directly measured and the spectral phase is calculated without use of any evolutionary algorithms. Once the compensation phase mask is obtained the phase shaper introduces it to achieve a transform-limited pulse. The method is fast, making it possible to implement multiple iterations within a few minutes.

Knowledge of the initial conditions is very important, especially in science. The reason of defining them is to establish the boundaries within which an experiment is going to be carried out and for better understanding of the phenomena under investigation. In particular, in the study of laser-matter interactions it is very crucial to have a well-characterized laser pulse, as an entry condition, to get unambiguous information on material response or laser-matter mutual modifications.

1.4 The wave equation and linear response of optical media

Laser-matter interactions can be described mathematically. Starting from the observation that the mass of an electron is much smaller than the mass of an atom, the electronic response can be treated classically as a harmonic oscillator. In the absence of an external force, the system remains at equilibrium. By applying an external driving force with frequency of ω the electron starts oscillating at the same frequency with respect to its equilibrium position. Such displacement is characterized by a local dipole moment, $\bar{\mu}$, shown in Figure 9. If we select a small enough volume, V ($\lambda > \sqrt[3]{V}$) the electric field, $\bar{E}$, can be considered uniform over the volume varying with time.

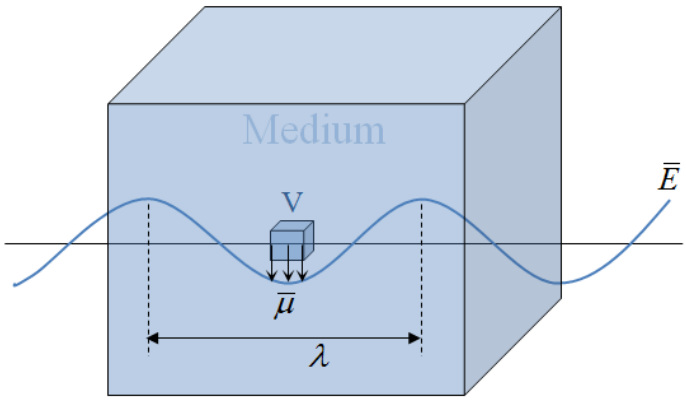

Figure 9. Propagation of an electromagnetic wave, $\bar{E}$, through a medium. Local volume, *V*, local dipole moment $\bar{\mu}$, and wavelength λ are shown.

Provided that this volume is homogeneous and the number of atomic dipoles (*N*) oscillate with the same frequency as an incident field, then the induced polarization depends linearly on the electric field strength. The speed at which the electron cloud can be distorted under the applied electric field depends on the polarizability of the medium, α. In order to mathematically describe laser-matter interaction one can use Maxwell's macroscopic equations [60]:

$$\nabla \cdot \bar{D} = \rho, \tag{8}$$

$$\nabla \cdot \bar{B} = 0, \tag{9}$$

$$\nabla \times \bar{E} = -\frac{\partial \bar{B}}{\partial t}, \tag{10}$$

$$\nabla \times \bar{H} = J + \frac{\partial \bar{D}}{\partial t}, \tag{11}$$

where $\bar{D}$ is the displacement field, ρ is the charge density, $\bar{B}$ is the magnetic field, $\bar{H}$ is the magnetizing field, and J is the current density. Assuming the nonmagnetic regions ($\bar{B} = \mu_0 \bar{H}$, μ_0 is the permeability of free space) where there are no free charges ($\rho = 0$) and no free currents ($J = 0$), the field $\bar{D}$ can be written as the following:

$$\bar{D} = \varepsilon_0 \bar{E} + \bar{P}, \tag{12}$$

where ε_0 is the permittivity of free space, and $\bar{P}$ is a polarization vector. Combining the four Maxwell equations with Eq. (12), the wave equation can be written as:

$$\nabla^2 \bar{E} - \frac{1}{c^2}\frac{\partial^2}{\partial t^2}\bar{E} = \frac{1}{\varepsilon_0 c^2}\frac{\partial^2 \bar{P}}{\partial t^2}, \tag{13}$$

where c is the speed of light in free space and $\bar{P}$ is the polarization vector. In the linear regime the light-induced polarization vector is proportional to $\bar{E}$ and oscillates at the light frequency. From the equation of motion one can derive that macroscopic polarization $\bar{P}$ is proportional to $\frac{Ne^2}{m_0}\left(\frac{1}{\omega_0^2 - \omega^2 - i\gamma\omega}\right)\bar{E}$, where m_0 is the mass of an oscillator, e is the charge, γ is the damping constant, ω and ω_0 are the frequency of the incident light and resonance frequency, respectively. At low frequencies, the electrons can directly follow the electric field variations in time. At higher frequencies, a phase shift occurs and at frequencies far above the resonance frequency, ω_0, the driving field and the induced polarization are out of phase.

Susceptibility is the macroscopic parameter describing the degree of polarization in a dielectric material with respect to an applied electric field. When the intensity of the electromagnetic field is high, such as in pulsed lasers, the origin of the nonlinear response comes from the anharmonic motion of bound electrons under the applied field. An induced polarization vector can be expressed as a power series [61]:

$$\bar{P} = \varepsilon_0(\chi^{(1)}\bar{E} + \chi^{(2)}\bar{E}^2 + \chi^{(3)}\bar{E}^3 + ...), \tag{14}$$

where $\chi^{(1)}$, $\chi^{(2)}$ and $\chi^{(3)}$ are the first, second, and third order susceptibilities. Such nonlinearity drives the electron further away from its equilibrium causing the polarization of the medium to oscillate at a complex frequency, which in turn, leads to the generation of new frequencies other than the one from the initial electromagnetic field.

1.5 Origin of nonlinear light-matter interaction

The nonlinear dependence of the polarization on the magnitude of the propagating field, described in Eq. (14), is due to the superposition of linear and nonlinear responses. The linear response is responsible for linear absorption and the well-known refractive index of materials, while the vast majority of the nonlinear responses are related to second and third order terms. By substituting each response into the wave equation, Eq. (13), one can derive a new radiation field with a new frequency. Processes such as second-harmonic generation, optical rectification (OR), and optical parametric processes correspond to the second-order susceptibility [60]. Processes such as third-harmonic generation (THG), optical Kerr effect (OKE), stimulated scattering, two-photon absorption, and cascaded processes, for example generation of the THG through SHG and SFG in nonlinear medium, are related to the third-order susceptibility [60]. Due to structural characteristics of the material, for example having a center of inversion symmetry, causes even-numbered optical processes to interfere destructively. Therefore, for such materials the most common nonlinear effect is $\chi^{(3)}$. When the initial field with a frequency of ω propagates through a medium with third-order nonlinearity, it generates a field with a frequency of 3ω, see Figure 10:

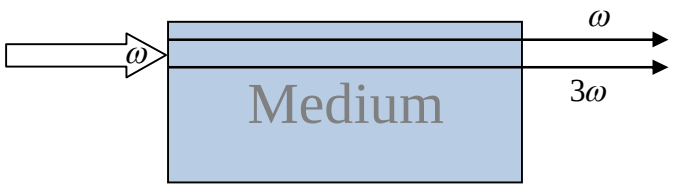

Figure 10. Nonlinear propagation of a light in media without inversion symmetry.

In this case, the equation for the initial electromagnetic wave propagating in *z* direction is the following:

$$\bar{E}(t) = E_1 \cos(k_1 z - \omega t), \tag{15}$$

where E_1 and k_1 are the amplitude and wave vector, respectively. Upon interaction with the medium it induces a new field that oscillates at a frequency of 3ω. This can be shown by substituting Eq. (15) into Eq. (14) and neglecting the first and second order terms:

$$\bar{P}_{NL} = \bar{E}_1^3 \cdot \frac{3\cos(k_1 z - \omega t) + \cos(k_3 z - 3\omega t)}{4}, \tag{16}$$

where k_3 is the wave vector of the wave at 3ω and is generated through a nonlinear interaction. Equation (16) shows that an initial wave causes a net dipole moment oscillating with frequency 3ω.

In general, the propagation of the field at frequency ω can be written as:

$$\nabla^2 \bar{E}^{(\omega)} - \frac{1}{\varepsilon_0 c^2} \frac{\partial^2 \bar{E}^{(\omega)}}{\partial t^2} = \frac{1}{\varepsilon_0 c^2} \frac{\partial^2 \bar{P}_{NL}}{\partial t^2}. \tag{17}$$

Propagation of the field at frequency 3ω in the nonlinear medium can be described by the following equation:

$$\nabla^2 \bar{E}^{(3\omega)} - \frac{1}{\varepsilon_0 c^2} \frac{\partial^2 \bar{E}^{(3\omega)}}{\partial t^2} = \frac{1}{\varepsilon_0 c^2} \frac{\partial^2 \bar{P}_{NL}}{\partial t^2}. \tag{18}$$

From Eqs. (16) - (18) one can see that $\bar{E}^{(\omega)}$ generates $\bar{P}_{NL}$ which, in turn, generates the $\bar{E}^{(3\omega)}$. Furthermore, $\bar{E}^{(\omega)}$ and $\bar{E}^{(3\omega)}$ together induce additional $\bar{P}_{NL}{}^{(\omega)}$ which, in turn, influences the initial $\bar{E}^{(\omega)}$. From this sequence it follows that a high intensity electromagnetic wave propagating through the medium not only changes the property of the medium but changes itself through nonlinear interaction.

The nonlinear response of the medium described above is fast and, depending on resonance conditions, can vary by orders of magnitude. The magnitude of the nonlinear response of a material depends on the physical processes involved. These processes have different origins, namely, electronic polarization, nuclear response, electrostriction and thermal response. The third-order susceptibility can therefore be decomposed in a sum of terms corresponding to each contribution:

$$\chi^{(3)} = \chi^{(3)}_{elec} + \chi^{(3)}_{nuc} + \chi^{(3)}_{str} + \chi^{(3)}_{th}. \tag{19}$$

The magnitude of the contribution from each of the components depends on the medium as well as on pulse duration and repetition rate of the laser [62-65]. The electronic response is quasi-instantaneous: less than one femtosecond [66]. It is due to the spontaneous nonlinear distortion of the electronic cloud around the nuclei and it is independent of temperature. The nuclear response corresponds to the rearrangement of

the nuclei's position due to induced dipole moment. But if the laser pulse is less than 50 fs the nuclear contributions are very small [67]. There are two other responses: electrostrictive and thermal, but they occur in nanosecond or microsecond time scales respectively [68] and they will not be considered here.

1.6 Nonlinear index of refraction

Third-order nonlinear optical effects underlay important physical phenomena such as self-phase modulation (SPM), self-focusing, and supercontinuum generation which occur within a single optical pulse. All these self-action processes require high-peak-power light pulses to propagate through a transparent medium. Depending on the intrinsic properties of the medium, such as the nonlinear index of refraction (n_2), the effect can be enhanced or suppressed for certain applications. The nonlinear contribution to the linear refractive index is proportional to $\frac{3}{4}\frac{\chi^{(3)}}{\varepsilon_0 c n_0^2}$, where n_0 is the linear index of refraction. The intensity-dependent refraction index, n, can then be expressed by the following first-order formula:

$$n(t) = n_0 + n_2 \cdot I(t), \tag{20}$$

where $I(t)$ is the intensity profile of the pulse. This effect was discovered by J. Kerr in 1875 and the first observation of self-phase modulation was made by F. Shimizu [69, 70].

1.6.1 Self-phase modulation

For an ultrashort laser pulse, the optical Kerr effect mostly originates from the quasi-instantaneous electronic contribution (electron reconfiguration is on the order of 0.1 fs) to the third-order susceptibility, which, in turn, leads to a variation of $n(t)$. This variation produces a nonlinear phase shift of the pulse within its pulse duration and results in a time-dependent frequency deviation, $\omega(t)$:

$$\omega(t) = \omega_0 - \frac{\omega_0}{c} L \frac{dn(I)}{dt}, \tag{21}$$

where L is a medium length. If the intensity, I, has a Gaussian intensity profile, see Figure 11(a), then the time-dependent frequency shift will look like it does in Figure 11(b). The leading edge of the pulse is

shifted to the lower frequencies (or longer wavelengths), whereas the back edge is shifted to the higher frequencies (or shorter wavelengths).

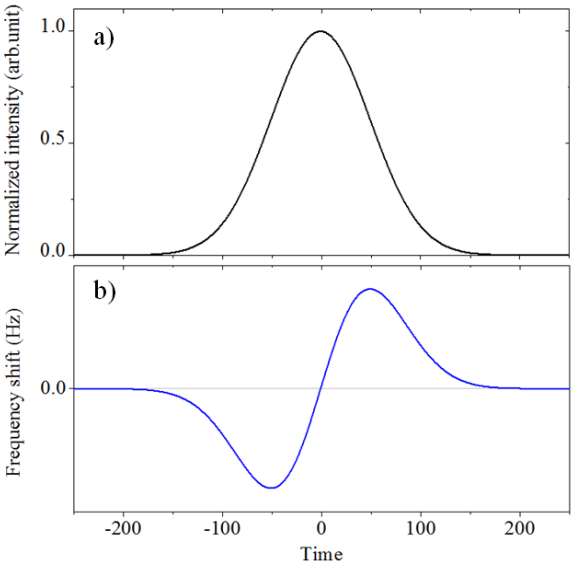

Figure 11. Self-phase modulation. (a) Temporal intensity profile of a Gaussian pulse. (b) Frequency shift due to time-dependent index of refraction. The front edge is shifted to the lower frequencies, the peak is not shifted, and the back edge is shifted to the higher frequencies.

Thus, the optical Kerr effect causes frequency chirp and the generation of additional frequency components. Self-phase modulation can be significant enough to create a laser rainbow, a process known as supercontinuum generation, when a certain power threshold is reached and the nonlinear interaction length (L_{NL}) is less than the propagation length (L), see Eq. (22):

$$L_{NL} = \frac{A_{eff} c}{P_0 n_2 \omega} < L, \tag{22}$$

where A_{eff}, in this case, is a beam area, ω is a carrier frequency, and P_0 is a peak power. For example, in 1 mm of fused silica, peak intensities on the order of 10^{11} W/cm^2 are below the threshold for supercontinuum generation, but are high enough to induce optical Kerr effects [71].

1.6.2 Self-focusing

Self-focusing is an optical Kerr effect in the spatial domain that can be explained using a similar equation to Eq. 20 but this time in the spatial domain:

$$n(r) = n_0 + n_2 I(r), \tag{23}$$

where r is a spatial beam coordinate, see Figure 12. This phenomena relates to the case when an intense laser pulse with a certain non-uniform intensity profile, for example a Gaussian profile, modulates the physical property of the medium. In this case the index of refraction has the greatest changes in the center of the beam than at the wings [72]. This change of the refraction index forms a spatial index differential which acts like a positive lens and forces the beam to come to focus inside the material. In gases, the process that prevents the beam from collapsing into one point is ionization defocusing, which acts like a negative lens. The balance between self-focusing and diffraction leads to the formation of filaments in gases, so the beam acts as its own waveguide. This effect occurs when the laser pulse carries a certain critical power, P_{cr} :

$$P_{cr} = \frac{\pi (0.61)^2 \lambda^2}{8 n_0 n_2} \tag{24}$$

Power more than P_{cr} leads to beam breakup [60].

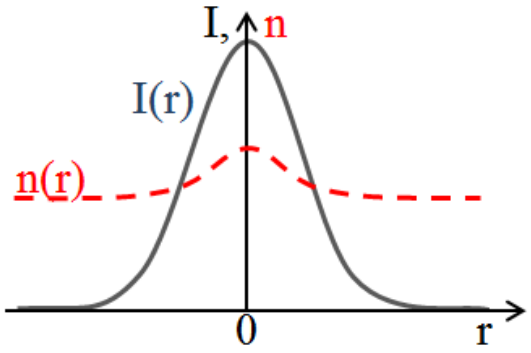

Figure 12. Self-focusing. Solid line corresponds to transverse Gaussian intensity profile. Dashed line is an index of refraction. The special variation of the intensity causes the special variation of the index of refraction.

1.6.3 Supercontinuum generation

In the earlier experiments, the primary mechanism which led to spectral broadening was self-phase modulation [73, 74]. Increasing the laser power to a critical level of catastrophic collapse, associated with self-trapped filaments, guaranteed the appearance of a supercontinuum [75, 76]. There are a few

drawbacks associated with this method, namely small power efficiency due to short interaction lengths and low laser material damage. This challenge was solved through processes such as cascaded stimulated Raman scattering (SRS) [77] and four-wave mixing (FWM) [78, 79] in optical waveguides with high nonlinear properties [80, 81]. The gas-filled hollow core waveguide (HWG) [82], large mode area (LMA) fiber [83, 84], and microstructured optical fiber [85-89] are the most commonly used waveguides.

The processes responsible for supercontinuum generation using ultrashort laser pulses in waveguides can be divided into two distinct cases determined by the sign of the GVD, see Figure13 for all-silica-based fiber [90]. In this figure, zero-dispersion wavelength (ZDW) is the wavelength where total dispersion (material and waveguide dispersions) equal to zero.

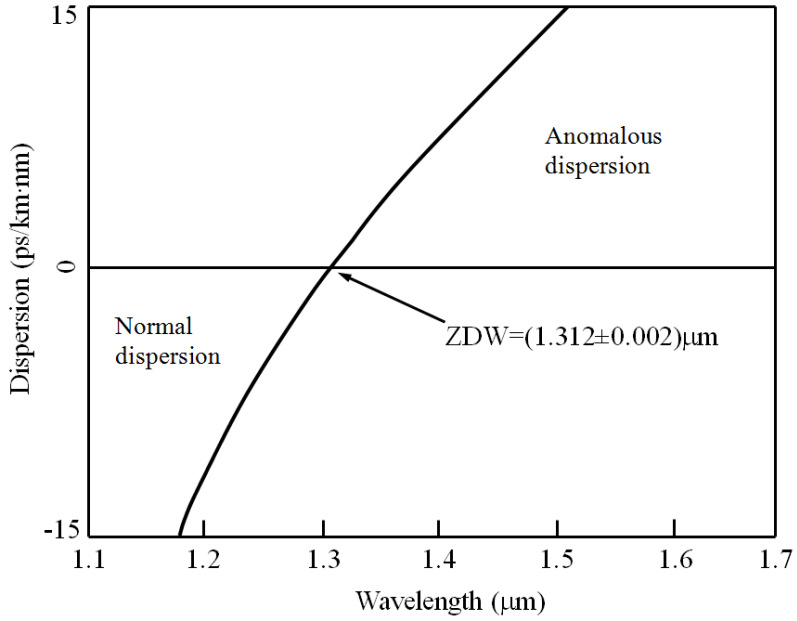

Figure 13. Dependence between dispersion and wavelength of an all-silica-based fiber.

For the case of normal GVD pumping the spectral broadening is dominated by self-phase modulation and self-steepening [91]. When pumping wavelengths are in the anomalous dispersion region, supercontinuum generation results from soliton-related dynamics [92, 93], namely, the initial spectral broadening and self-compression, soliton fission, intrapulse stimulated Raman scattering, and dispersive wave emission [94, 95]. Pumping in the anomalous dispersion regime may provide the generation of a much broader spectrum with a finer structure than pumping in the normal dispersion regime, but due to

the power fluctuations it causes more noticeable coherence degradation [96]. By optimizing waveguide parameters, such as core size or fiber structure, one can control the dispersion of the guided modes, enhance the interaction length and thus, the third-order nonlinear-optical processes.

1.7 Coherent Raman Scattering

All the third-order nonlinear processes described above relate to elastic scattering, i.e. the case when the kinetic energy of the incident photon is conserved after the interaction with a medium. The opposite to this phenomena is inelastic scattering, which causes the energy of the particle to increase (anti-Stokes Raman scattering) or decrease (Stokes Raman scattering) by an amount proportional to the molecule's vibrational frequency, ω_{vib}, see Figure 14.

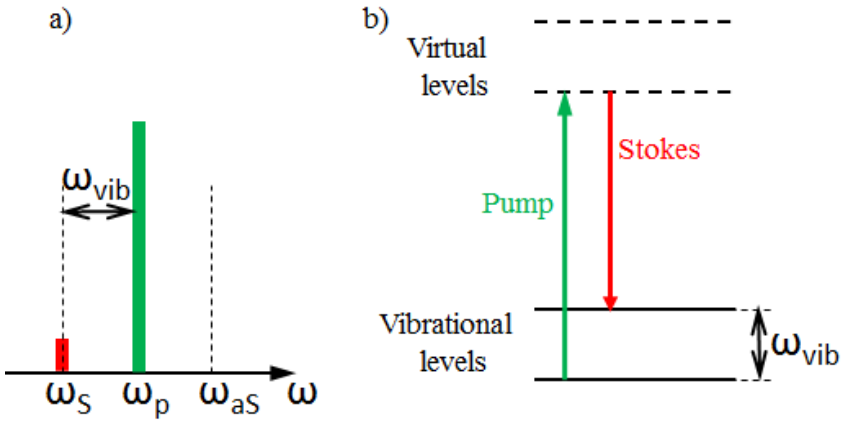

Figure 14. Inelastic scattering. (a) Monochromatic excitation (ω_p) and Stokes (ω_S) line. Note that the Stokes line is more intense than the anti-Stokes line (not shown) due to the low probability of a molecule to be in the excited state prior to excitation. (b) Corresponding energy diagram of Stokes Raman scattering. ω_{vib} is a vibrational frequency.

For different materials the induced dipole moment is different due to the molecular structure and nature of the bonds. This property of the medium is connected to polarizability and depends on the position of the individual atoms. The classical description of Raman scattering considers an incident electromagnetic (EM) field with frequency ω_0 and causing spontaneous emission at $\omega_0 - \omega_{vib}$, matching the molecule's quantized vibrational modes, ω_{vib}. In the presence of the field, electrons in a molecule are displaced from their equilibrium position by [97]:

$$dQ(t) = Q_0 \cos(\omega_0 t)\,, \tag{25}$$

where $dQ(t)$ is a current displacement of the nuclear coordinate and Q_0 is a magnitude of the displacement. Note this is similar to the polarization process described earlier. For a small displacement the polarizability can be expanded in Taylor series. Including Eq. (25) the polarizability can be expressed as:

$$\alpha = \alpha_0 + \frac{d\alpha}{dQ} Q_0 \cos(\omega_0 t)\,, \tag{26}$$

where α_0 is a polarizability at equilibrium. Given that the dipole moment is a product of both the polarizability and the oscillating electric field, $E_0 \cos(\omega_0 t)$, in combination with Eq. (26) can be written as follows:

$$\bar{\mu} = \alpha_0 E_0 \cos(\omega_0 t) + \frac{\partial \alpha}{\partial Q} \frac{Q_0 E_0}{2} \left[\cos(\omega_0 - \omega_{vib})t) + \cos(\omega_0 + \omega_{vib})t)\right], \tag{27}$$

Equation (27) describes the appearance of secondary radiation which oscillates at two new frequencies, namely $(\omega_0 - \omega_{vib})$ and $(\omega_0 + \omega_{vib})$, the Stokes and anti-Stokes lines respectively. Therefore, vibrational modes with asymmetric differential polarizability, $\frac{\partial \alpha}{\partial Q}$, are considered to be Raman active. The first term relates to the ensemble of molecules, which oscillates at the same frequency as the incident field and cause Rayleigh scattering. The first term does not carry any information about molecular structure. The second and the third terms contain information about molecular structure and the normal modes of molecular vibration, ω_{vib}.

Spontaneous Raman scattering is a weak optical process (more than 8 orders of magnitude weaker than elastically scattered light in solids [98] due to a small scattering cross-section. A strong fourth power dependence on the inverse of the excitation frequency makes this signal even harder to observe when using long excitation wavelengths. At low temperatures, < 500 K, Stokes Raman scattering

usually is a more favorable process than the anti-Stokes Raman scattering due to the negligible population probability of vibrational overtones.

The Raman signal can be considerably enhanced, by more than six orders of magnitude, using a joint action of the incident fields with frequencies ω_S and ω_p. If the frequency difference between them matches one of the molecule's vibrational modes it causes the variation of the refraction index and leads to frequency shift, Ω, with respect to probing frequency:

$$\omega_{aS} = \omega_{pr} + (\omega_p - \omega_S) = \omega_{pr} + \Omega. \tag{28}$$

The spectrum of the coherent Raman process for narrow lines and its energy diagram are presented in Figure 15.

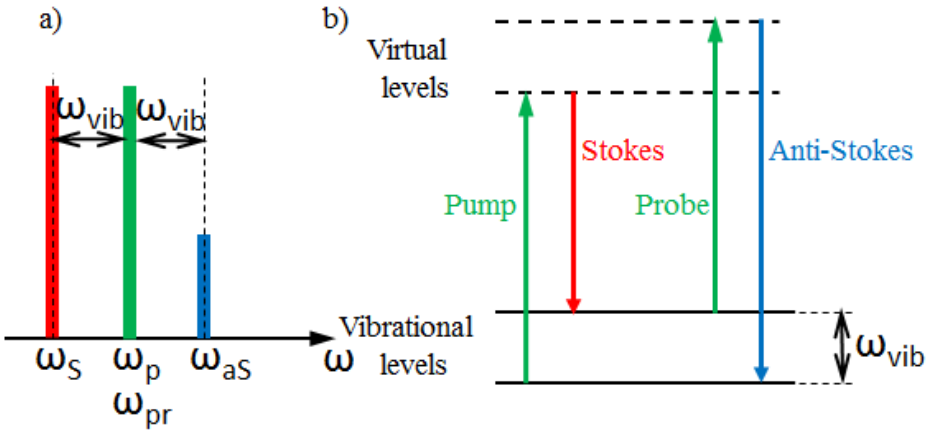

Figure 15. Coherent Raman scattering. (a) Excitation lines, ω_p and ω_S, and scattered line, ω_{aS}. (b) Energy diagram of the coherent Raman scattering. In this case, pump (ω_p) and probe (ω_{pr}) frequencies are the same.

The third order susceptibility in a classical model is given by:

$$\chi^{(3)}(\Omega) = \frac{N}{6m\varepsilon_0}\left(\frac{\partial\alpha}{\partial Q}\right)^2 \frac{1}{\omega_{vib}^2 - \Omega^2 - 2i\Omega\gamma}, \tag{29}$$

where N is the molecular number density, m is the reduced mass of the molecule, and γ is the damping constant determining the natural line width of the Raman vibrational mode. The intensity of the coherent anti-Stokes Raman (CARS) signal has the following dependence:

$$I(\omega_{aS}) \propto \left|\chi^{(3)}\right|^2 I_p I_S I_{pr}\,, \tag{30}$$

where I_p, I_S, I_{pr} are the intensities of the pump, Stokes, and probe beams, respectively. Since the process is coherent, there is a fixed phase relationship between incident and scattered fields. Scattered fields in coherent processes are added up. Therefore, the intensity is proportional to the number of scatterers squared, as it is shown in Eqs. (29) and (30). In comparison to the spontaneous Raman signal, the CARS signal arises directly due to the phase-matching requirement.

Chapter 2 Photonic control and pulse-to-pulse characterization of high-repetition rate lasers

The development of solid-state femtosecond laser has enabled a vast amount of fundamental scientific research in physics, chemistry, and biology. A key concept in this field of research is that the superposition of many monochromatic optical waves allows for the generation of ultrashort pulses, and provides the possibility to manipulate each of the spectral components to create any desired shape in both the spectral or temporal domains. The ability to control the time of arrival of each spectral component is used in many research laboratories that study applications related to coherent control. One of these applications includes the generation of a square-shaped temporal pulse profile, which will be covered in Section 2.1. Square-shaped pulses with steep back and front edges were produced using phase-only modulation with no loss of spectral bandwidth. We have demonstrated numerically and experimentally the conversion of 40 fs pulses into pulses 150 times longer duration. Such pulses can be used for efficient pumping of a gain medium in optical parametric chirped-pulse amplification (OPCPA) apparatus [99], which, in turn, is utilized as a seeding source for free-electron laser (FEL) systems, such as FLASH or X-ray FEL (XFEL).

Nonlinear optical applications depend on the pulse duration and coherence of the laser pulses. Knowing the exact properties of the laser source is of great importance for applications based on nonlinear effects. Traditional pulse characterization methods, such as autocorrelation, are subjected to misleading averaged pulse duration measurements. Characterization of high-repetition rate pulsed laser sources can be complicated by their pulse-to-pulse instabilities. In Section 2.2 I introduce a quantitative measurement [100] that can be used to determine the pulse-to-pulse fidelity of ultrafast laser sources. Numerical simulations and experiments illustrate the effect of spectral phase and amplitude noise on second- and third-harmonic generation.

This chapter has been adapted with permission from (Opt. Express **23**, 27105-27112 (2015)), (Opt. Express **23**, 23597-23602 (2015)), and (Opt. Express **23**, 12037-12044 (2015)).

2.1 Phase-only synthesis of ultrafast stretched square pulses

Self-action processes, which manifest as self-phase modulation or self-focusing, limit the peak intensity that can be transmitted through an optical medium. When the light pulses are ultrashort ($< 10^{-12}$ s), the threshold for self-action processes can be reached with very low energies. The introduction of chirped-pulse amplification (CPA) and OPCPA were significant steps in the scaling of ultrafast laser pulse energy [32, 101-103]. The lower peak intensity of the square-shaped pulses implies a higher gain that a CPA system can sustain without damage. Generation of square pulses using spectral phase modulation, as presented here, is advantageous because the pulses can be recompressed to their original duration by applying the inverse spectral phase. Conventional grating pair stretcher can make pulse significantly longer, but in case of a Gaussian pulse profile, a huge portion of this pulse is not involved in amplification process, thus lowering the conversion efficiency [104, 105]. For a Gaussian pulse the peak of the pulse is near the self-action threshold but the rest of the pulse is well below the threshold. Clearly, a different pulse shape would be able to satisfy the condition of maintaining peak intensity below the threshold while occupying a smaller temporal footprint. The square-shaped pulse is the optimal solution for minimal pulse duration while not exceeding the self-action threshold, as illustrated in Figure 16. For example, a square-shaped pulse with the same FWHM as a Gaussian pulse is three times shorter than the Gaussian pulse, T_{Gauss}. The discussion here is relevant to ultrafast laser pulses, therefore, the square-shaped pulse must maintain the entire spectral bandwidth of the original pulse. Only such pulses can be recompressed to their original pulse duration by introducing the inverse phase used to create them. In this chapter we show how such square-shaped pulses can be created starting from laser pulses with any spectral shape.

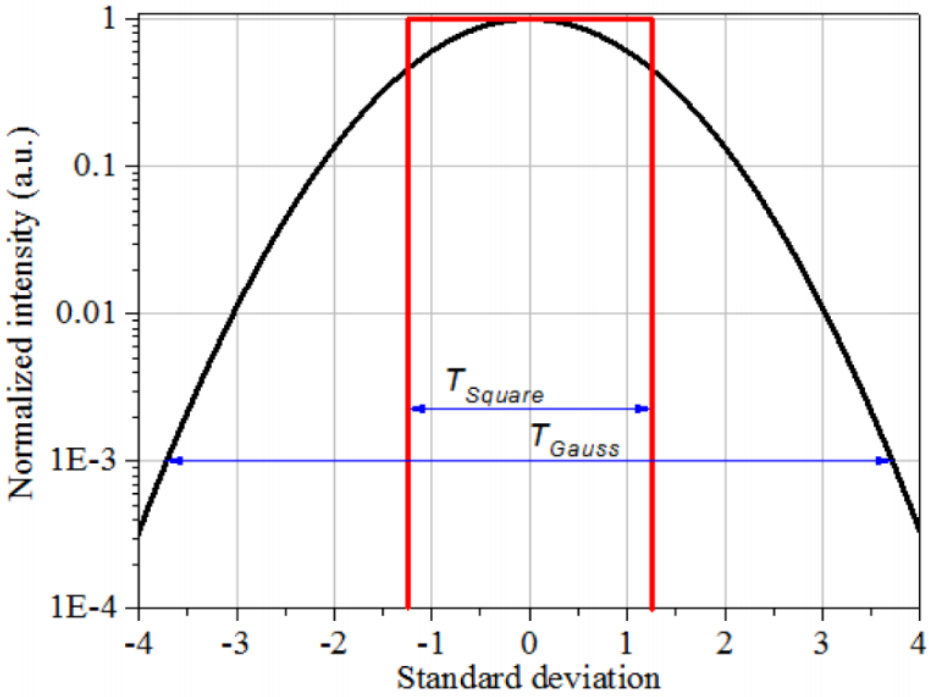

Figure 16. Simulated intensity of a Gaussian (black) and square-shaped (red) pulses with equal peak power and FWHM as a function of time in units of Gaussian standard deviation. T_{Square} and T_{Gauss} are the bottom-to-bottom pulse durations for square and Gaussian pulses, respectively.

A number of approaches have been explored for the generation of square-shaped pulses starting with femtosecond pulses. The first approach uses a pulse shaper that introduces a phase and amplitude mask in the frequency domain that corresponds to the Fourier transform of the square pulse in the time domain. This method was implemented using a microlithograhically etched mask [106], and later using a liquid crystal spatial light modulator [107]. The main drawback to this approach is the resulting spectral narrowing caused by the amplitude mask. This approach could not provide a viable alternative for CPA because of irreversible pulse broadening in the time domain. Second, flat-top 200 fs FWHM pulses were created using a phase mask generated by both a genetic algorithm and a Gerchberg-Saxton algorithm [108]. This approach works; however, for every input laser spectrum and final square-shaped pulse duration, the phase needs to be redetermined by the optimization algorithm. Third, an approach, which limits the spectral bandwidth with a super-Gaussian spectrum and an optimally designed phase was explored numerically but has not been implemented experimentally [109]. Finally, there is an intriguing

approach that is based on the concept of stacking pulse replica one after the other in order to create a flat-top pulse with pulse duration proportional to the number of pulses stacked in time [110]. The advantage of this method is its simplicity. The disadvantage is that spectral interference among the replicas results in the sync-function spectrum of the output square-shaped pulse, which is much narrower than the input pulse spectrum.

2.1.1 Theoretical concept

The phase-only generation of a stretched square-shaped pulse is based on the following concept. In the limit of large linear chirp the temporal shape of a stretched pulse approaches its spectral intensity, $I(\omega)$. In this case, the delay $\tau(\omega) = d\varphi(\omega)/d\omega$ is a linear function, and its derivative, i.e. local stretching $d\tau(\omega)/d\omega = d^2\varphi(\omega)/d\omega^2$, is a constant. Therefore all frequency components are linearly delayed or advanced and stretched equally such that the spectral shape is mapped to the pulse shape. For example, consider a pulse with a Gaussian spectrum. Linear chirp stretches the pulse but its shape remains Gaussian, see Figures 17(a) and (b). To make a square pulse one has to adjust the local stretching $d\tau(\omega)/d\omega$ to account for changes in spectral intensity: higher intensity requires more stretching, lower intensity - near the wings - requires less stretching, see Figures 17(c) and (d). If $d\tau(\omega)/d\omega$ is proportional to the spectral intensity of the pulse:

$$\frac{d\tau(\omega)}{d\omega} = \frac{d^2\varphi(\omega)}{d\omega^2} \propto I(\omega) \tag{31}$$

then the pulse shape becomes a square for any arbitrary spectrum, $I(\omega)$.

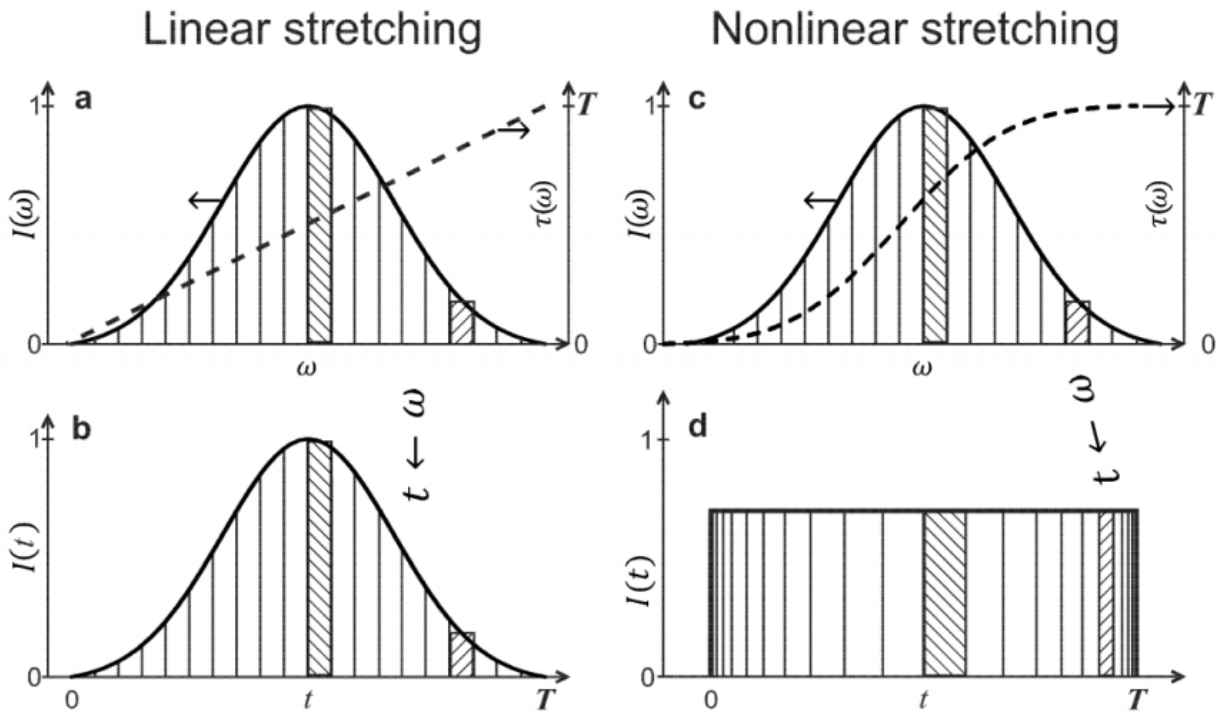

Figure 17. Pulse stretching with linear chirp, (a) and (b); or with a nonlinear function (c), (d) based on Eq. (31). The dashed line corresponds to $\tau(\omega)$.

The duration of the stretched pulse is the difference between delay values for the extreme spectral components, $T = \tau(\omega_{\max}) - \tau(\omega_{\min})$, see Figure 18(b). To satisfy this condition for the pulse duration T, the delay and the spectral phase should have the following forms, respectively:

$$\tau(\omega) = \frac{d\varphi(\omega)}{d\omega} = T\frac{\int_0^{\omega} I(\omega')d\omega'}{\int_0^{\infty} I(\omega)d\omega}, \tag{32}$$

$$\varphi(\omega) = \int_0^{\omega} \tau(\omega')d\omega'. \tag{33}$$

Figure 18 demonstrates the concept of square-shaped pulse generation. Here, the initial spectrum is set equal to the second derivative of the phase (Figure 18(a)) and is used to determine the spectral delays (Figure 18(b)), which then are used to generate the spectral phase, see Figure 18(c). It is worth noting that using phase distortion with opposite sign compresses the pulse to its original duration and shape.

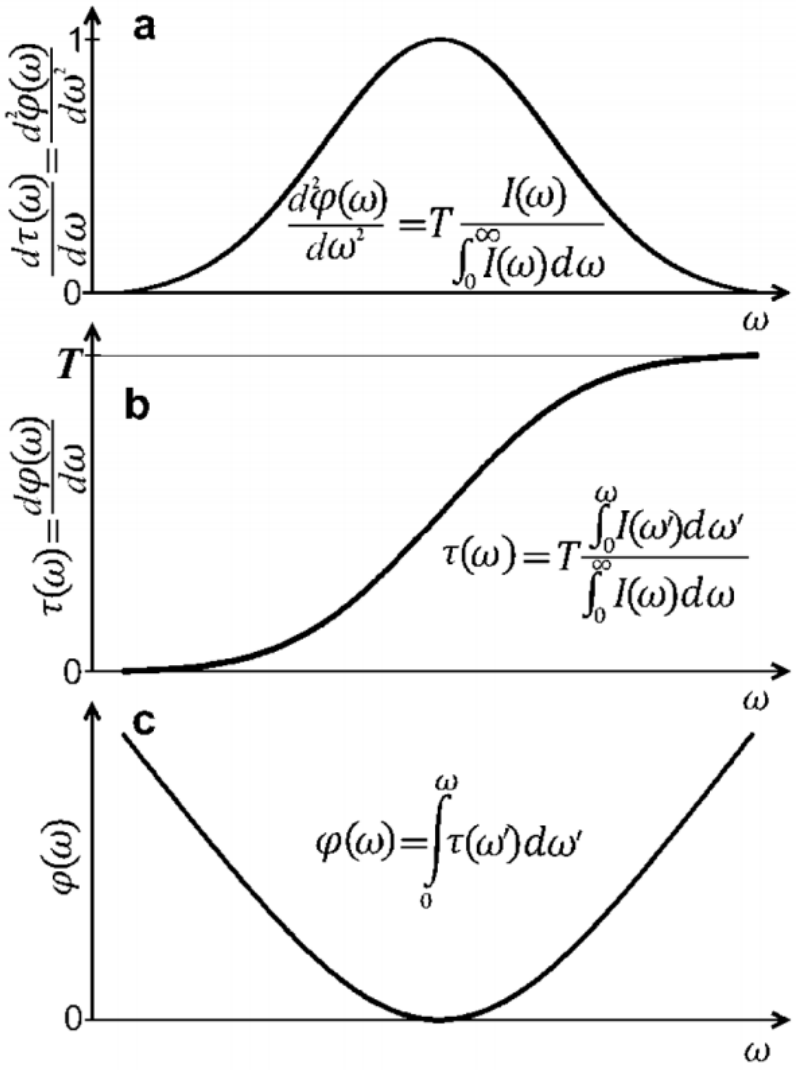

Figure 18. Phase modulation in the frequency domain generates a square-shaped pulses in the time domain. (a) The second derivative of the phase, equivalent to the local stretching. (b) The first derivative of the phase, equivalent to delay of the frequency components. (c) The spectral phase required to convert the original pulse into a square-shaped pulse in the time domain.

The proposed method works well for large stretching ratios $T/\tau > 10$, where τ is the initial pulse duration . For smaller stretching ratios the pulse profile is limited by the inherent rise time of the pulse. Figure 19 shows simulated pulse profiles for different stretching factors, where the initial pulse duration was changed, while keeping the final pulse duration, T, the same.

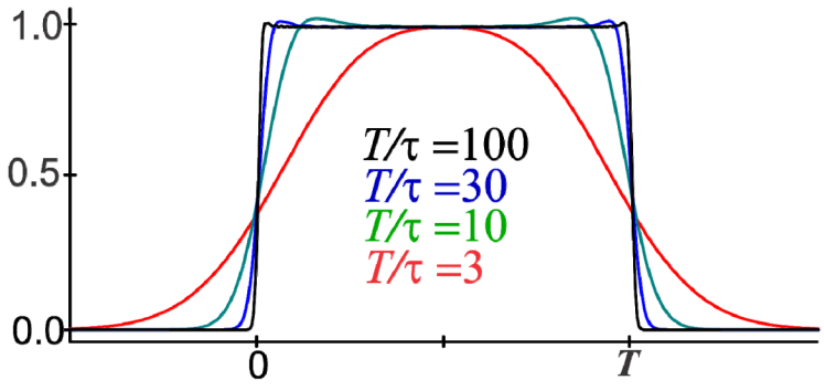

Figure 19. Square-shaped pulses in the time domain with the different stretching parameters.

2.1.2 Experimental results

Implementation of the expressions given above in the laboratory is straight forward when using a well calibrated pulse shaper that is capable of eliminating unwanted phase distortions (starting with a Fourier-limited pulse) [111-113]. The experimental setup shown in Figure 20 consists of a Ti:Sapphire oscillator (Micra, Coherent, Inc.), a pulse shaper (FemtoFit, BioPhotonic Solutions, Inc.), and a Ti:Sapphire regenerative amplifier (Legend, Coherent, Inc.). The output was split into two beams that form a cross-correlator, shown in a Figure 20 as '1' and '2'. Beam 1 goes through an optical delay line, and beam 2 goes through a second pulse shaper (MIIPS Box640 PA, BioPhotonic Solutions, Inc.) where the desired phase is introduced.

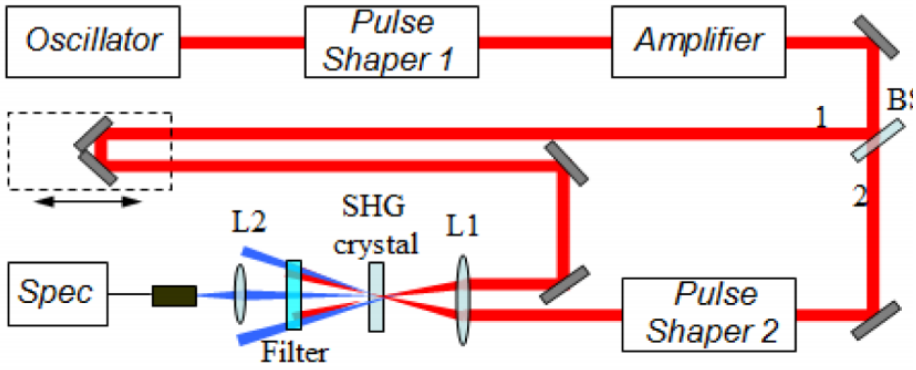

Figure 20. Experimental setup. BS, beam splitter; L1, L2 are lenses; Beams 1 and 2 after the beam splitter are recombined at the SHG crystal, where the pulses are measured.

Both beams were then focused in a nonlinear crystal (KDP crystal) by a 400 mm focal length lens. The SHG signal was recorded with a spectrometer (USB 4000, Ocean Optics). The pulses in both beams are first compressed to transform limited duration (40 fs at FWHM) using MIIPS [111-113].

The experimental demonstration of square-shaped pulse generation is shown in Figure 21(a), where the black curve shows the cross-correlation measurement of the resulting square-shaped pulse. The blue curve shows the cross-correlation of the input transform-limited pulses, and the red curve shows a linearly chirped pulse with $-39{,}000\ \mathrm{fs}^2$. Both square and linearly chirped pulses have the same peak power and energy. The phase mask for the square pulses is calculated according to Eq. (31), using the experimental laser spectrum and selecting the desired duration, T. The phase is introduced by Pulse Shaper 2. Figures 21(b) and (c) show the spectrally resolved cross-correlation for both the square and linearly chirped pulses, respectively. From these plots one can see that the SHG intensity is evenly distributed in time within the 3 ps window for the square-shaped pulse, however, for the chirped pulse the SHG is concentrated within the central picosecond. This illustrates an even distribution of the peak intensity inside the square-shaped pulse. It is worth noting, that phase modulation does not affect the SHG laser pulse spectrum, or the fundamental (800 nm wavelength range) spectrum.

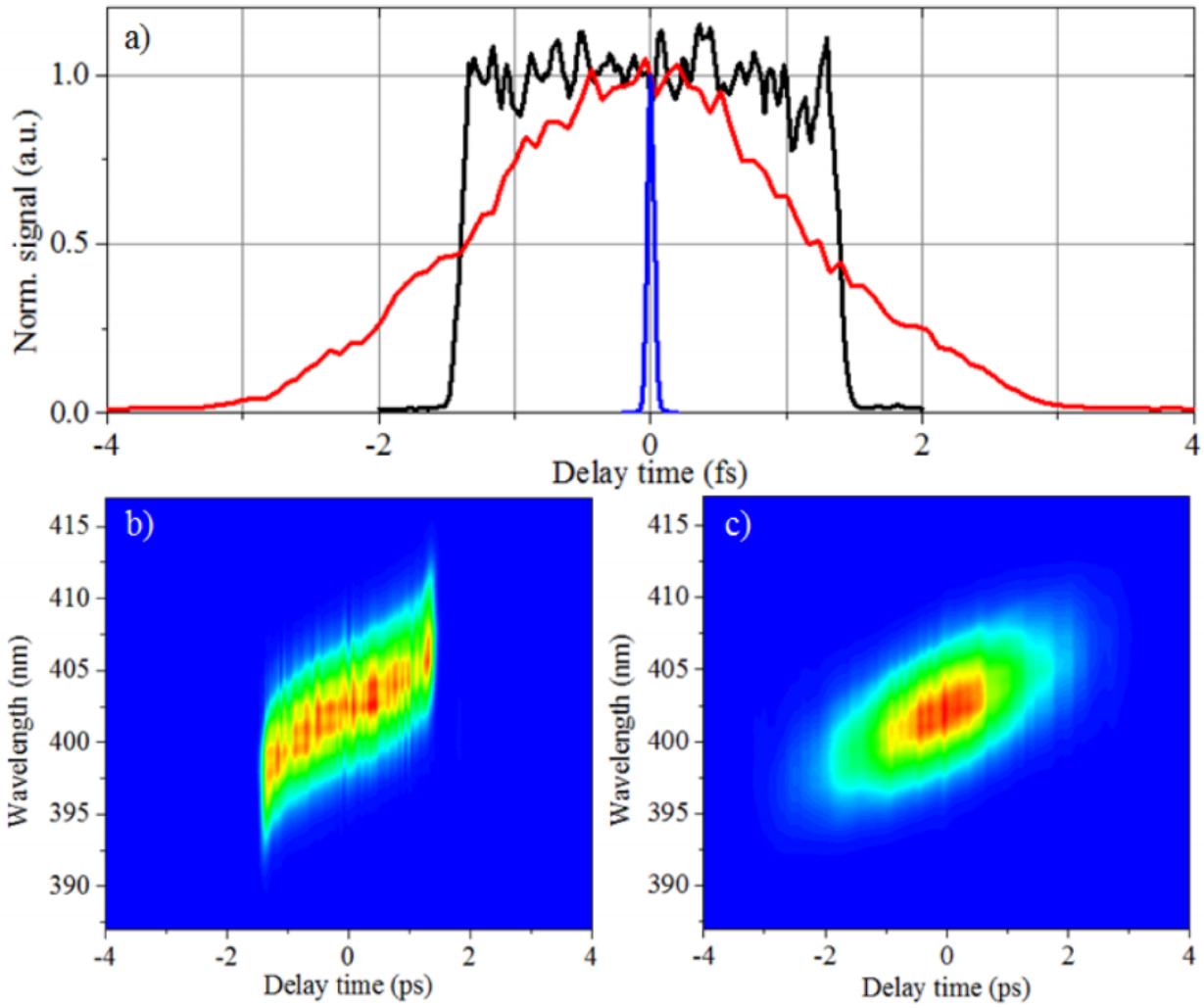

Figure 21. Experimental cross-correlation measurements. (a) Integrated SHG intensity for the input transform limited pulse (blue), the linearly chirped pulse (red) and the square-shaped pulse (black) as a function of delay. (b) Spectrally resolved cross-correlation measurements of the square-shaped pulse; (c) Spectrally resolved cross-correlation measurement of the linearly chirped pulse.

The approach, described for generating square-shaped pulses, is only limited by the number of pixels in the pulse shaper. A non-pixelated device such as a deformable mirror does not have this limitation. The maximum stretching factor $T_{\max} / \tau$ equals the number of pixels within the FWHM of the laser spectrum. We show experimental results for stretching a 40 fs pulse 75, 100 and 150 times in Figure 22(a). The results are plotted in logarithmic scale to show the steep front and trailing edges of the pulses and the low background with no satellite pulses. No additional special effort was made to reduce the background level

below 1% in the square pulses. In Figure 22(b) we also show that the proposed method for creating stretched square-shaped pulses does not affect the fundamental laser spectrum, therefore pulses can be recompressed.

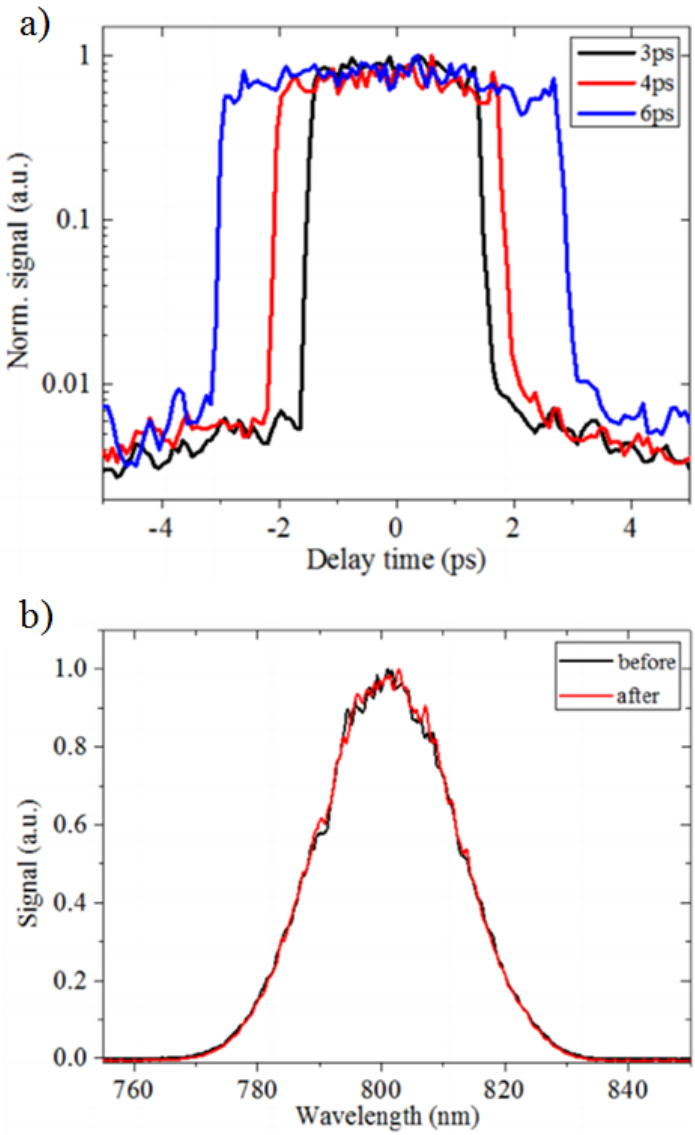

Figure 22. (a) Experimental cross-correlation measurements (logarithmic scale) of square-shaped pulses at different pulse durations. The input pulses duration is 40 fs. (b) Fundamental laser spectrums before and after 10x stretching. Note, that the phase required to create square-shaped pulses does not affect the spectrum of the pulse.

One of the motivations for phase-only square-shaped pulse generation is that the pulses can be fully recompressed. We test this hypothesis by introducing the phase desired to create 10x stretched pulses at

the output of the amplifier using Pulse Shaper 1. We then use Pulse Shaper 2 to recompress the pulses. In Figure 23(a) we show the phase applied by Pulse Shaper 1, and the phase retrieved by Pulse Shaper 2 in order to recompress the pulses. Note that it is essentially the same phase as introduced by Pulse Shaper 1. Figure 23(b) shows the autocorrelation of the pulses without stretching and after stretching by Pulse Shaper 1 and recompression by Pulse Shaper 2. Full implementation of this approach for CPA will require considerable thought regarding the most reliable and cost-effective optics to be used for stretching and compression. Similarly, design and cost considerations will determine whether the final laser system will include static optics or a programmable pulse shaper.

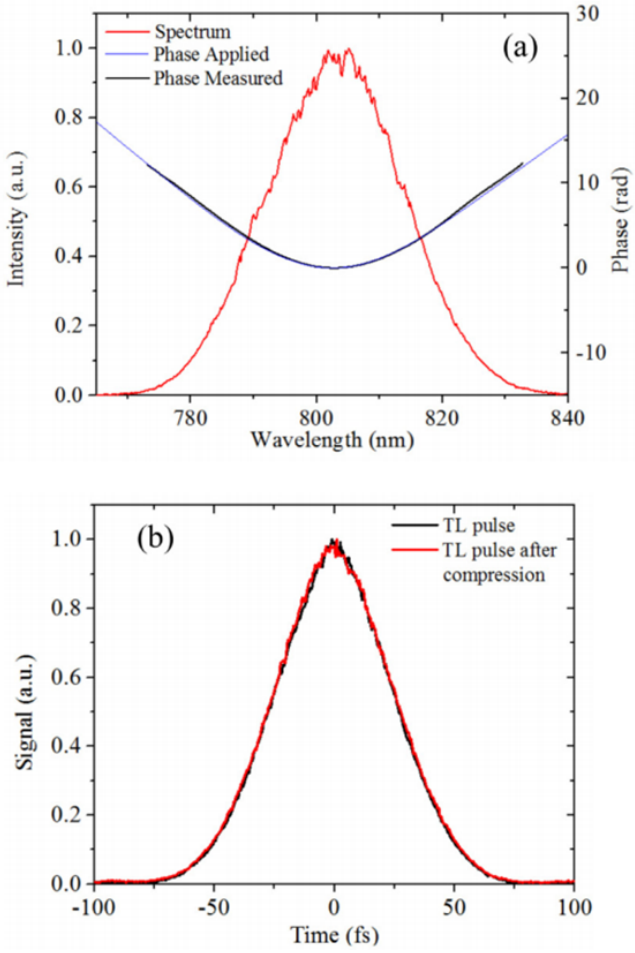

Figure 23. (a) Experimental laser spectrum (red). Blue curve is the applied spectral phase by Pulse Shaper 1. Black curve is the measured spectral phase by Pulse Shaper 2. (b) Experimental autocorrelation measurements of the amplified laser output pulses without stretching (black) and after 10x square-pulse stretching by Pulse Shaper 1, amplification, and compression by Pulse Shaper 2 to TL duration (red).

2.1.3 Conclusion

We have presented an analytic solution to the generation of square-shaped pulses in the time domain starting from essentially any arbitrary spectrum. MatLab code is shown in Appendix A. The premise of this work is that linear chirp is not always an efficient approach to mitigate self-action processes which are highly sensitive to peak power of a pulse. Numerical and experimental results testing this hypothesis demonstrate that the square-shaped pulses result in significantly more compact pulses in the time domain than the corresponding linearly chirped pulses. The approach causes no spectral bandwidth loss and is reversible. This means, in order to recover the original input pulse one needs to introduce the complementary phase to the one used to stretch the pulse. Applications of our findings range from an alternative to CPA amplification to other applications where self-action mitigation is important, for example, in fiber optic communications and nonlinear optical imaging using a fiber-based endoscope. In comparison to a chirped pulse, a square pulse with the same peak intensity has a three times smaller temporal duration, requires less stretching and thus smaller spectral dimension on the compression grating. Square-shaped picosecond laser pulses with sharp front and trailing edges are desirable for the production of high-brightness electron beams used in free-electron lasers, Compton scattering light sources, and MeV electron microscopes [114-116]. There are other scientific applications for square-shaped pulses with very fast turn on/off , for example, quasi-phase-matched conversion to soft X-ray photon energies, where the fast turn on initiates ionization and the flat top maintains the high-peak intensity [117], and time-resolved coherent anti-Stokes Raman scattering [118]. From a practical sense, while the use of a dedicated pulse shaper is ideal for the generation of square pulses, having an analytic solution should simplify the implementation of this approach for stretching and compressing ultrafast pulses using specially designed dispersive optics such as chirped mirrors and volume/fiber Bragg gratings that takes into account the spectrum of the input pulse.

2.2 Multi-shot coherent artifact in high repetition rate pulsed lasers

Given that the characterization of high repetition rate lasers depends on the quantities averaged over multiple pulses, it is difficult to determine pulse-to-pulse variations and to quantify their effect on a pulse duration. Pulse-to-pulse instabilities can be expressed in terms of intra- (spectral amplitude or phase) or inter- (timing jitter) fluctuations. The causes of such fluctuations are varied. They range from beam pointing instabilities, peak power or temperature variations or quantum noise. As the laser industry continues the development of different stabilization schemes, these types of instabilities are getting less dominant but still exist. For example, a train of varying pulses could imitate an average pulse with a pulse duration different than the individual pulse duration and therefore cause ambiguities in data interpretation [119]. Therefore, we have set out to develop a method for quantitative characterization of ultrafast laser sources based on easy to measure averaged quantities.

Applications such as two-photon excited fluorescence microscopy and second harmonic generation (SHG) imaging depend on the pulse duration [120, 121]. Pulse duration can therefore be an important criterion for predicting the expected nonlinear optical signal when comparing different laser sources. Unfortunately, the pulse characterization of noisy or partially incoherent laser sources is challenging given the appearance of the so-called autocorrelation coherent artifact [122]. In recent publications, frequency resolved optical gating (FROG) [123] and spectral phase interferometry for direct electric-field reconstruction (SPIDER) [48] were evaluated for their ability to quantify pulse shape instabilities [124-126]. The growing number of ultrafast laser sources that take advantage of self-phase modulation to increase spectral bandwidth, a process that in some cases leads to phase and amplitude noise, and this raises the question of how to accurately characterize their output based on averaged measurements. Microstructured fibers, for example, have been used to generate short pulses. However, the pulse-to-pulse reproducibility may be compromised [127]. Some fiber lasers are known to operate in both soliton-like and noise-like regimes [128, 129]. Quantifying noise and its impact on practical nonlinear optical applications is therefore a high-priority endeavor. In this work, we introduce a

measurement that can be used to determine the pulse-to-pulse fidelity of a laser, which quantifies the performance of the laser for nonlinear optical processes and helps distinguish between spectral phase and spectral amplitude fluctuations when the laser spectrum changes from pulse-to-pulse. Previous indicators of laser performance include basic techniques for measuring the amplitude noise or relative intensity fluctuations of continuous wave lasers [130-132]. Some methods have evolved to measure the noise and jitter of metrology sources, where it becomes important to know how close the source's contribution is to the noise floor [133]. More recently, the shot-to-shot coherence and spectral fluctuations of noise-like ultrafast fiber lasers were characterized by making use of Young's-type interference and single shot spectrometry at megahertz repetition rates [134, 135]. Such measurements clearly show the lack of coherence in noise-like pulse trains. Analysis of noise in pulse trains from mode-locked laser pulses is best illustrated by the work of von der Linde, where the power spectrum of the pulse train is shown to contain important information about the noise characteristics [136]. Periodic signals, as well as laser pulses, can be analyzed in terms of cyclostationary theory [137, 138]. Aspects such as jitter, amplitude and duration fluctuations can be detected in the frequency comb spectrum [139, 140].

The metric presented here and referred to as "fidelity" is best suited to characterize laser sources being used for nonlinear applications, using tools usually found in an ultrafast laser laboratory. The fidelity of a pulsed laser is an indicator of expected statistically-averaged laser performance. Fidelity is insensitive to intensity fluctuations, which are easily measured by a simple photodiode. Given two laser sources with similar TL pulse durations (based on averaged laser spectra), repetition rates and energy per pulse, the one with higher fidelity will lead to more efficient SHG and brighter multiphoton microscopy images.

2.2.1 Theoretical concept

It is tempting to tie expected laser performance to average pulse duration; unfortunately, measuring the average pulse duration of a noisy laser by conventional methods such as autocorrelation is not reliable

because of the aforementioned coherent spike. The duration of the spike depends on the coherence time τ_c of the source, defined by the spectral width and shape of the pulse.

Here we define fidelity based on the attenuation of a nonlinear optical process such as SHG as a function of added linear chirp, later we discuss other nonlinear optical processes such as third harmonic generation (THG). We introduce an expression that can be used in the laboratory to determine the pulse-to-pulse fidelity function or curve as defined by Eq. (34):

$$\left\langle F(\varphi^{"})\right\rangle = \frac{I_{\varphi^{"}}^{SHG} / I_{TL}^{SHG}}{\left\langle I_{\varphi^{"}}^{SHG}\right\rangle / \left\langle I_{\varphi^{"}=0}^{SHG}\right\rangle} = \frac{I_{Theory}^{SHG}(\varphi^{"})}{\left\langle I_{Experiment}^{SHG}(\varphi^{"})\right\rangle}, \tag{34}$$

where $\varphi^{"}$ is the amount of chirp in the frequency domain, $I_{Theory}^{SHG}(\varphi^{"})$ and $\left\langle I_{Experiment}^{SHG}(\varphi^{"})\right\rangle$ are the calculated and experimental normalized SHG intensity measurements as function of chirp. The intensities in the numerator are calculated assuming coherent noiseless pulses with a spectrum identical to the averaged laser spectrum being characterized. The denominator corresponds to averaged values measured for the second harmonic intensity of the laser source for the case, where the pulse has an amount $\varphi^{"}$ of linear chirp, divided by the second harmonic intensity when the output has no added chirp. The ratio between the averaged measurements makes the measurement insensitive to simple intensity fluctuations. Note that a noisy ensemble of pulses, with low fidelity, produces more SHG than one with high fidelity in the presence of a large chirp. This is because the low-fidelity source, on average, has pulses that are longer than the coherence time τ_c and, therefore, is less affected by chirp. Thus, a laser output with $\left\langle F\right\rangle = 1$ is highly coherent, while the one with $\left\langle F\right\rangle = 0$ is incoherent. The key is that Eq. (34) can be used to determine the practical performance of a laser, whilst avoiding the coherent artifact that is inherent to autocorrelation measurements. For large chirp values the intensity of nonlinear optical processes like SHG divided by the intensity of the same pulse when TL decays as $1/\varphi^{"}$. Therefore Eq. (34) reaches asymptotically a value for large chirp values $\left|\varphi^{"}\right| >> \tau_c^2$. The definition above considers pulse trains that

average to Fourier-limited pulses, measurements on non-Fourier-limited pulses will be discussed later in the chapter.

2.2.2 Numerical simulations

Armed with a functional measurement for fidelity, we test a number of possible sources of noise that may be found in ultrafast lasers. For example, in mode-locked oscillators, random processes such as spontaneous emission, cavity-length fluctuations, or active beam alignment by a piezoelectric-actuated mirror cause fluctuations. In regenerative Ti:Sapphire amplifiers, the shot-to-shot variations may occur because of spontaneous emission and gain fluctuations from spectral turbulence inside the stretcher and compressor compartment or timing jitter associating with firing the Pockels cells. In all cases, we consider conditions that affect individual pulses but are difficult to detect by averaged measurements. In particular we considered (a) spectral jitter, where the spectrum experiences small random shifts towards shorter or longer wavelengths that average to zero; (b) random positive and negative chirp values that average to zero; (c) random high-order phase distortions that average to zero; (d) random phases on pulses that have random spectral amplitudes that satisfy a certain temporal window. The longer the temporal window used the lower the fidelity. Cases (a)-(c) can be found in oscillators, especially when operating at high pumping powers and in the presence of small air fluctuations. Case (d) is unusual for oscillators but has been found in the generation of ultrafast pulses from free-electron lasers [141] and has been used to simulate noisy pulses [124, 126]. For each simulation, we generate a train of 100 ‘noisy’ pulses, and calculate their corresponding averaged characteristics including the fundamental spectrum and the SHG spectrum as a function of linear chirp. From this data, we calculated their fidelity as a function of chirp introduced according to Eq. (34). For each case, we varied the noise magnitude to simulate output with fidelity values that ranged from 0.1 to 1.0. For all cases, we compared with ideal transform-limited 36 fs pulses. When calculating the train of noisy pulses we made sure that on average they had no phase distortion; that is, any pulse characterization method that measured their average phase would indicate they are transform limited. If one introduces linear chirp and collects the SHG spectrum at the same time,

one obtains a chirp-scan. Chirp scans have been shown to provide accurate pulse characterization, especially when one considers the linear chirp introduced as a reference phase [111, 112, 142, 143]. The chirp-scan, or multiphoton intrapulse interference phase scan, provides a direct measurement of the second derivative of the spectral phase [111]. Such scans are presented below for a set of ideal 36 fs pulses and for noisy pulses obtained by applying a random amount of positive or negative chirp, see Figure 24. The maximum SHG intensity at zero chirp observed for both cases indicates that both sets of pulses have no systematic spectral phase such as linear chirp or third order dispersion. The ensemble of noisy pulses, however, shows a much broader distribution of intensities because within the ensemble there are pulses with a wide range of chirp values.

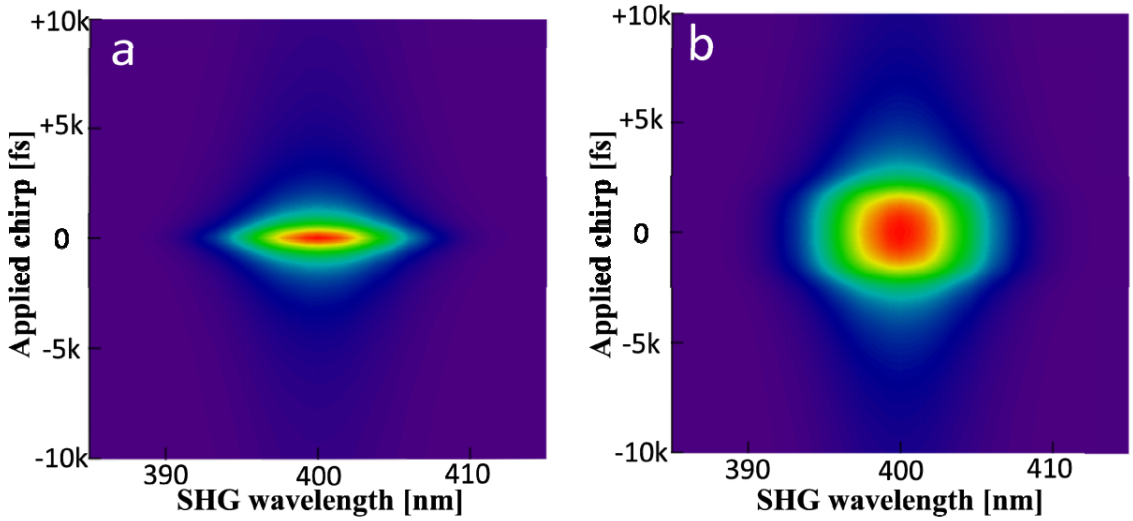

Figure 24. Numerical simulations of a MIIPS scan, where the SHG spectrum is plotted as a function of chirp, obtained for an ideal ensemble of coherent 36 fs transform-limited pulses with unit fidelity (a) and for an ensemble of noisy pulses with random amounts of positive and negative chirp (b). The SHG spectrum in both cases is the average of the entire ensemble of pulses.

From the simulations shown in Figure 24, it is possible to calculate fidelity. We present such analysis for an ensemble of pulses having random magnitudes of positive and negative linear chirp such that the asymptotic fidelity equals 0.5. In Figure 25(a) we show how SHG intensity varies for ideal pulses (dashed line) and for the ensemble of noisy pulses (bold line) as a function of introduced linear chirp. Note that the noisy train of pulses is less sensitive to linear chirp. Figure 25(b) corresponds to the reciprocal

dependence shown in Figure 25(a) showing that for large chirp the dependence of SHG on chirp becomes linear. The fidelity curve and asymptotic value $\langle F \rangle$, as defined by Eq. (34) is shown in Figure 25(c).

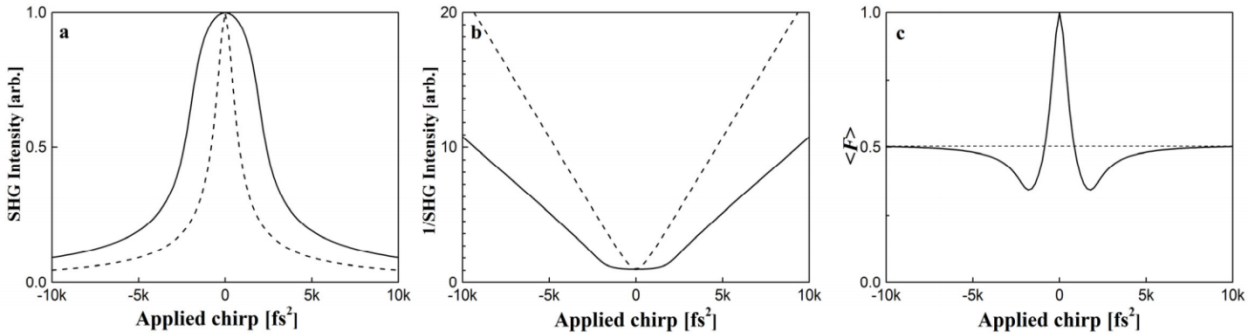

Figure 25. Numerical simulations corresponding to Fourier-limited (dashed line) and noisy pulses (solid line) having a distribution of positive and negative chirps; see text. The dashed line in figure (c) indicates the asymptotic fidelity.

We now examine in more detail signatures from different types of noise. For example, we illustrate spectral amplitude noise Figure 26(top), random spectral phase noise Figure 26(middle) and a mixture of phase and amplitude noise Figure 26(bottom). We find that the fidelity curve is distinctively different depending on the source of noise. Amplitude noise results in an averaged spectrum that is broader, which incorrectly could assume to correspond to shorter pulses. This leads to a sharp feature in the fidelity curve, see Figure 26(top). For the case of random phase noise, pulses are much less sensitive to small amounts of chirp given the additional phase modulation. This leads to the appearance of features below the asymptotic fidelity value, see Figure 26(middle). The fidelity curves are instrumental to determine if the source of noise is phase or amplitude spectral fluctuations (the spectrum changes from pulse to pulse). For completion, a case in which the noise comes from both amplitude and phase fluctuations is shown in Figure 26(bottom). In this case the central feature in the fidelity curve is broad.

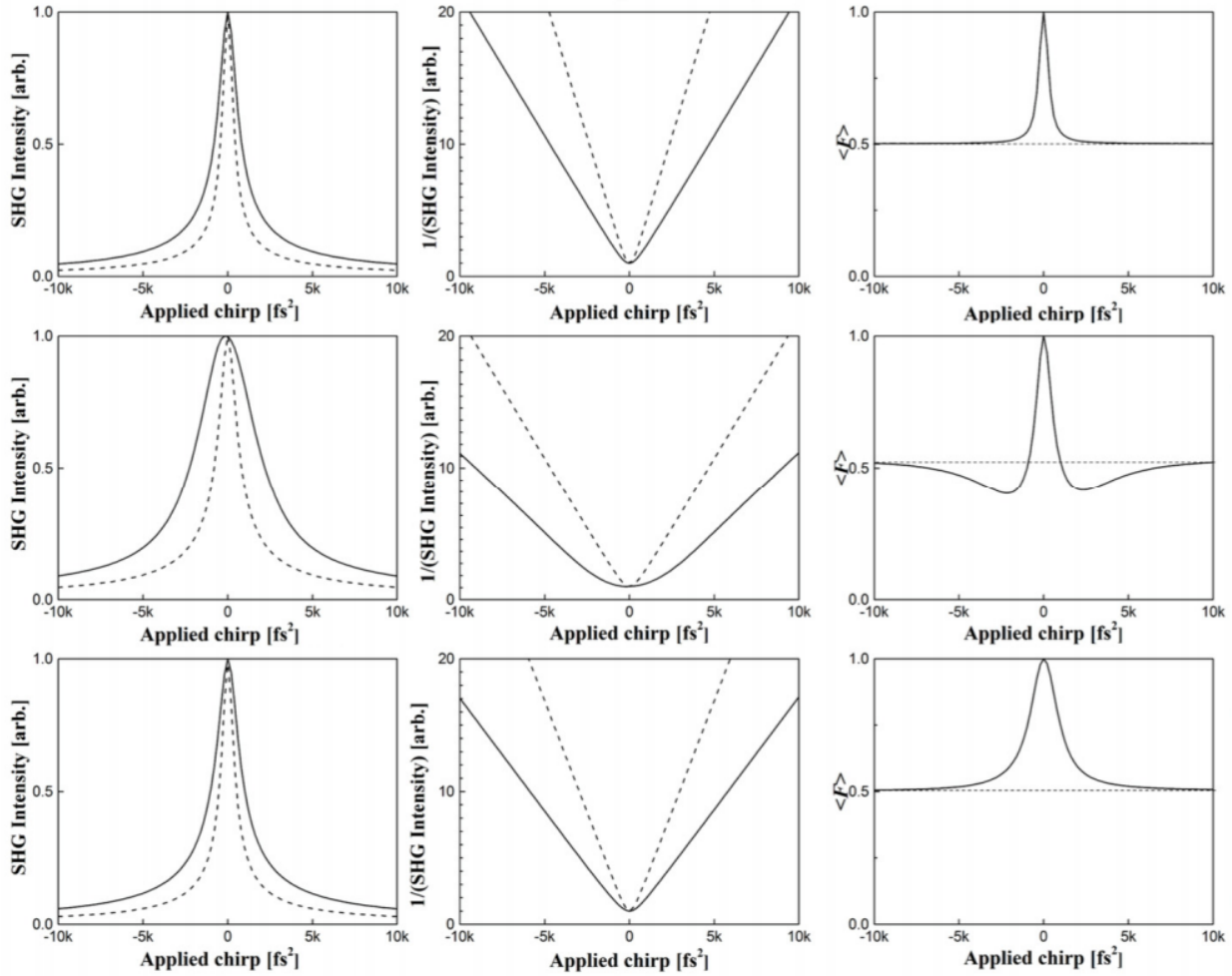

Figure 26. Numerical simulations corresponding to Fourier-limited (dashed line) and noisy pulses (solid line) having (top) spectral jitter, (middle) random phase modulations, and (bottom) a mixture of phase and amplitude modulations. The dashed line in the third column indicates the asymptotic fidelity.

It is important to determine how a fidelity value translates into practical applications such as two-photon excited fluorescence or SHG imaging. The correlation between fidelity (x-axis) and relative intensity of SHG or THG are plotted in Figure 27. We have found that the source of noise changes the dependence; therefore, we introduce Eq. (35).

$$\left\langle I^{SHG}_{\ddot{\varphi}=0} \right\rangle = I^{SHG}_{TL} \left\langle F(\ddot{\varphi}) \right\rangle^{n} \tag{35}$$

where the SHG or THG attenuation experienced by the ensemble of pulses compared to a fully coherent source depends on the asymptotic fidelity value to the n^{th} power. The asymptotic fidelity value can be

used to determine the effective attenuation or nonlinear optical signal caused by noise. The power dependence, *n*, in Eq. (35) depends on the type of noise and nonlinear optical process as shown in Figure 27. For spectral amplitude noise, the SHG/THG intensity correlates with fidelity to the order *n*=0.5/*n*=1. For phase and amplitude noise, SHG/THG correlates with fidelity to the order *n*=0.6-0.7/*n*=1.5. For phase noise, SHG/THG correlates with fidelity to the order *n*=1/*n*=2. Measuring a fidelity curve, Eq. (34), reveals the dominant contribution to noise (phase or amplitude). The asymptotic fidelity value obtained for large chirp tells us, through the Eq. (35), by how much a nonlinear process such as SHG or THG is attenuated due to noise.

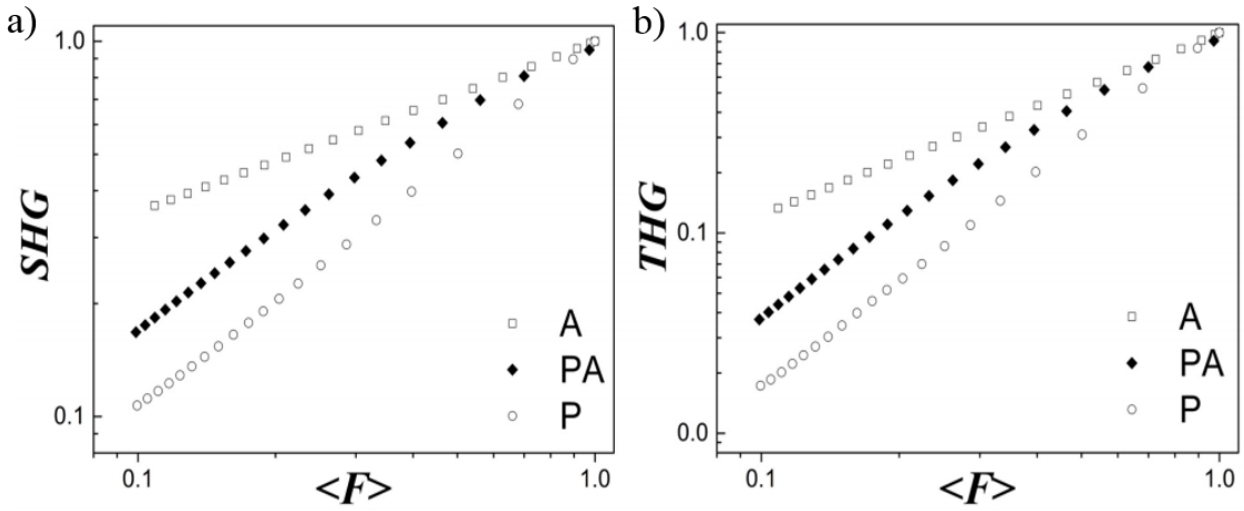

Figure 27. Numerical simulations showing the power dependence of expected SHG (a) and THG (b) intensity on fidelity: A for amplitude noise, PA for phase and amplitude noise, and P for phase noise.

Consider a pulsed laser output with $\langle F \rangle = 0.5$ being used for nonlinear optical imaging such as SHG or THG microscopy, it is important to know how the low fidelity value affects signal intensity. In the most common case of phase fluctuations, SHG/THG decreases to ½ and ¼ of the expected value for noiseless pulses, respectively. In the rare case of large spectral jitter, SHG/THG would decrease by a factor of $\sqrt{2}$ and ½, respectively. In the case of mixed phase and amplitude noise, SHG/THG signal would be reduced by a factor of ~0.6 or ~1/3, respectively.

Fidelity measurements are also possible for pulse trains that do not average to Fourier-limited pulses. If the ensemble of laser pulses being measured has a net positive chirp, the MIIPS trace shifts to a negative chirp value. The opposite sign results because the maximum SHG is obtained when the net chirp of the laser is compensated by the chirp introduced by MIIPS. Numerically shifting the SHG intensity scan so that at all wavelengths the maximum SHG is centered at zero dispersion results in a plot similar to the MIIPS data shown in Figures 24(a) and (b), from which a value for fidelity can be easily obtained. Fidelity measurements can also be obtained for lasers having a combination of linear chirp and third-order dispersion (TOD). TOD causes a MIIPS trace to appear as a diagonal feature [111, 112], as shown in Figure 28(middle column). In Figure 28 if high order dispersion is uncorrected, then values for positive $\langle F_+ \rangle$ and negative $\langle F_- \rangle$ chirp are quite different; however, simply shifting each spectrum to zero dispersion yields the correct value for fidelity. It should be clear that any combination of linear chirp and TOD can be easily treated by shifting as shown in Figure 28(right column) to obtain reliable fidelity measurements. If higher-order phase distortions are present it is necessary to measure and compensate these distortions using iterative MIIPS [111, 112] or other pulse shaper based method capable of compensating arbitrary phase distortions. Note that the MIIPS average spectral phase measurement and compensation are not affected by noise. The reported pulse duration by the MIIPS algorithm, which takes into account the laser spectrum, would be underestimated in the case of a laser with low fidelity. This highlights the importance of the proposed fidelity measurement.

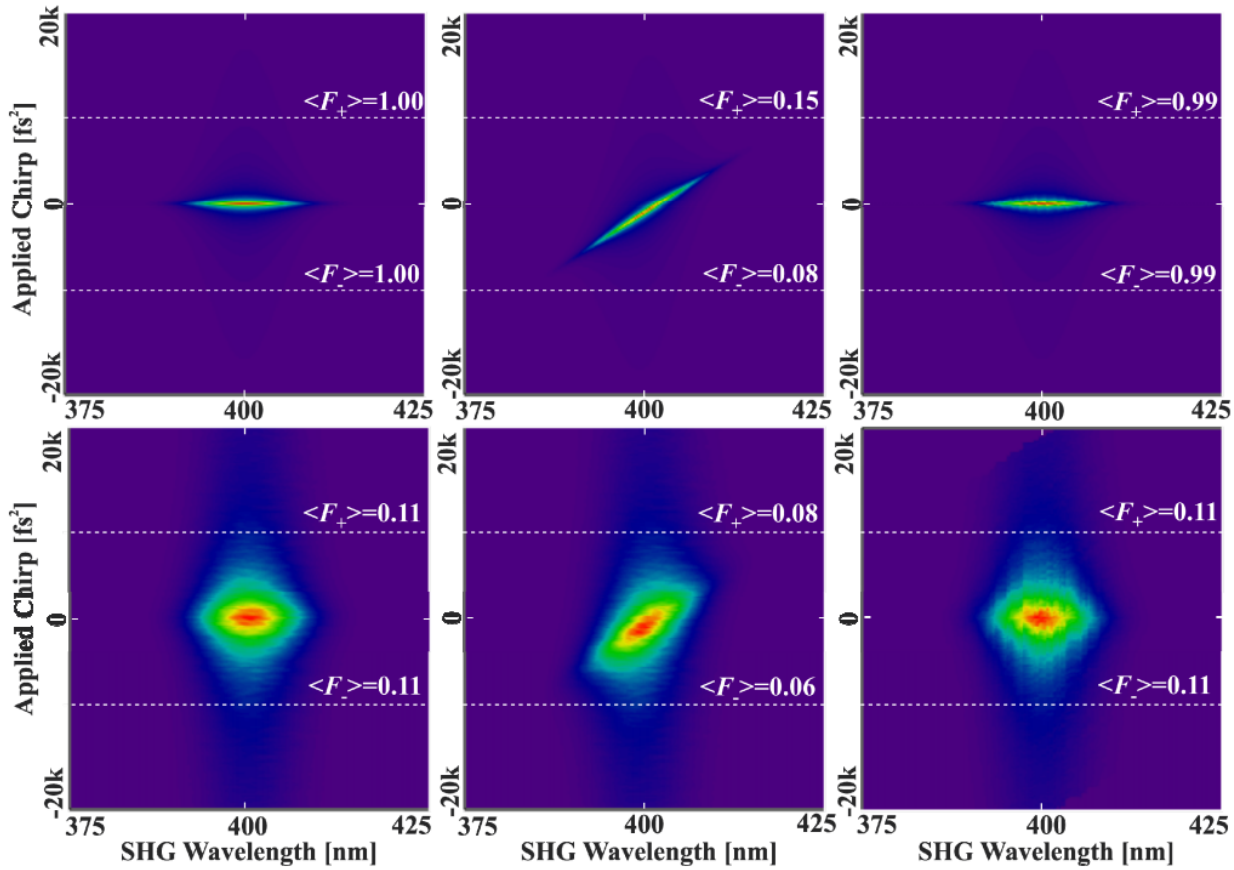

Figure 28. 2D MIIPS traces for an ensemble of random pulses with average phase distortion 900 fs^2 and 2.7×10^4 fs^3 starting with 30 fs TL pulses. Chirp is scanned ± 20000 fs^2 (vertical axis), and the spectral range (horizontal axis) is 375 nm to 425 nm. First row illustrates coherent pulses with unit fidelity. Second row is for random pulses with an average pulse duration of 300 fs. First column is for no dispersion, the second column is with dispersion, and third column is obtained by numerically shifting the spectral line to zero chirp. The dashed white lines correspond to ± 9000 fs^2. Each simulation corresponds to 1000 random pulses, each measured as a function of 500 different chirp values.

2.2.3 Experimental measurements

The experimental setup includes a Ti:Sapphire oscillator (Micra, Coherent, Inc.), a pulse shaper (FemtoFit, BioPhotonic Solutions Inc.) placed between the oscillator and amplifier, a Ti:Sapphire regenerative amplifier (Legend, Coherent, Inc.), home-built autocorrelator, focusing lens, nonlinear crystal (KDP crystal), blue filter (BG39) and spectrometer (Ocean Optics, USB 4000). The pulse shaper was used to measure and compensate the averaged dispersion of the laser pulses using MIIPS [111, 112], and to scan the linear chirp on the pulses. In Figure 29, we present experimental autocorrelation

measurements for regeneratively amplified pulses under three different conditions: (a) high fidelity, (b) spectral phase noise, and (c) presence of post pulses. For these measurements the two arms of the interferometer were crossed at the nonlinear crystal and the SHG was detected. As we can see from Figures 29(a)-(c), the intensity autocorrelations are comparable; autocorrelation measurements are insensitive to phase noise and to pre- or post-pulses.

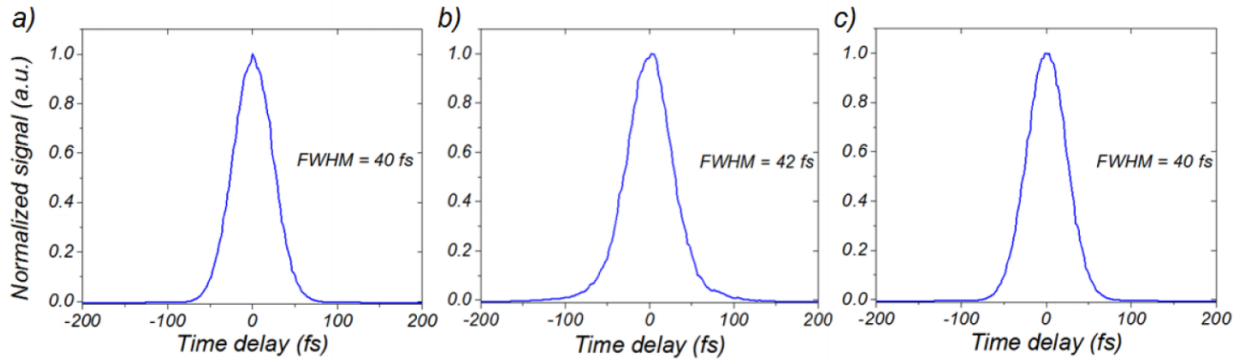

Figure 29. Non-collinear SHG autocorrelations for amplifier (a) without any distortions, (b) with airflow averaged 100 times, (c) with post-pulse. Note that autocorrelation is not sensitive to changes in pulse duration caused by spectral amplitude or phase noise.

In Figure 30 we show fidelity measurements after pulse compression using MIIPS [112]. The values for $\langle F_{-} \rangle$ and $\langle F_{+} \rangle$ were measured at the 10% normalized intensity level, see green dots, where the asymptotic value is reached and the signal to noise ratio is still good. From the plots we can conclude that laser pulses were compressed to TL duration and that the oscillator has a very good pulse-to-pulse reproducibility. The fidelity parameters, which are marked as green points, equal to 0.98 and 0.99 respectively. The pulse-to-pulse stability was measured analyzing 22,000 waveforms with the oscilloscope. After statistical analysis of the peak signal values, the relative standard error was calculated and found to be ~0.3% for the fundamental signal and ~1% for the SHG signal. Based on the fidelity curve one can conclude that the major source of pulse-to-pulse instability in the oscillator is spectral phase fluctuations.

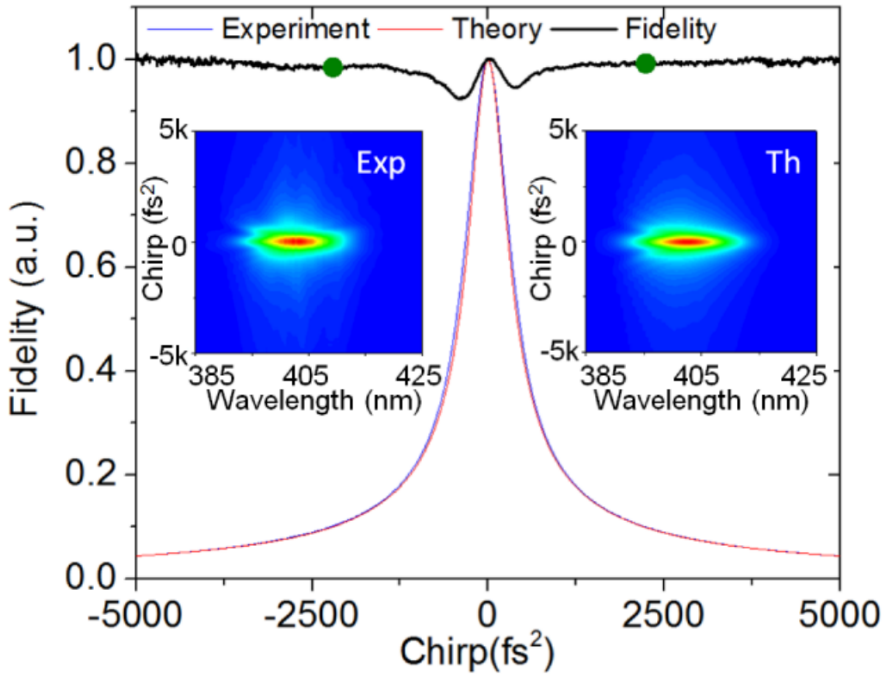

Figure 30. Fidelity measurements for a Ti:Sapphire oscillator (28 fs) when the pulses are fully compressed. The insets show the experimental and theoretical 2D SHG chirp scans. The fidelity asymptotic values, green dots, are 0.98 and 0.99.

Fidelity measurements for amplified TL pulses after pulse compression are shown in Figure 31(a). The fidelity drops from >0.98 to ~0.95 after amplification due to fluctuations of spectral phase introduced by the amplifier. Note that these are some of the best values measured in our lab from our best amplified system. The most pronounced source of noise in the amplifier is the stretcher where the spectrum is dispersed and vulnerable to spectral phase noise. In order to amplify such noise, the cover for the stretcher and compressor was removed. For these measurements, 100 chirp scans were averaged in order to smooth the instantaneous SHG intensity fluctuations. The results from this measurement are shown in Figure 31(b), where we see that the fidelity has dropped to 0.88. The pulse-to-pulse intensity fluctuations, measured with an oscilloscope, for these cases are ~1% for the fundamental and ~2% for the SHG signal. When the compressor and stretcher compartments are open the fluctuations increase to ~11% for the SHG signal only. The large difference between the fundamental and SHG signal confirms that the major source of noise is spectral phase fluctuations.

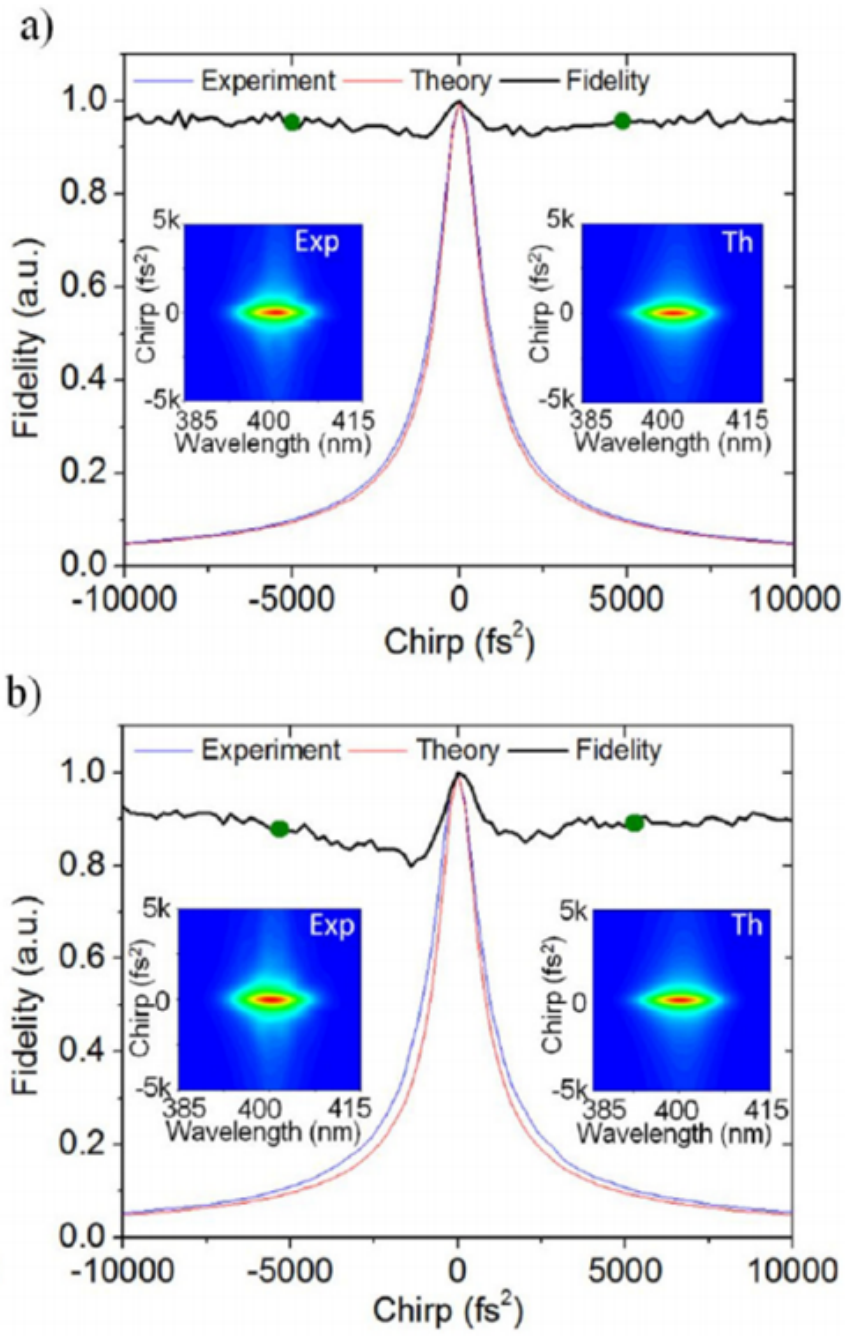

Figure 31. Fidelity measurements for compressed laser pulses after the regenerative amplifier (a) in the absence of distortions. Both positive and negative fidelity parameters equal to 0.95. (b) When the pulses are distorted by airflow in the stretcher and compressor. The fidelity parameters equal to 0.88 and 0.89, respectively. The pair of insets shows the experimental and theoretical 2D SHG chirp MIIPS scans respectively.

Beyond noise, it is important to determine if an amplifier generates pre- or post-pulses. A post-pulse was generated by misadjusting the timing of the second Pockels cell in the amplifier. The noise statistics for

the amplifier output were 1% for fundamental and 2% for SHG signals, which implies pre- and post-pulses cannot be detected by intensity fluctuations. Fidelity measurements for fully compressed amplified pulses that have a post-pulse are shown in Figure 32(a). Pre- or post-pulses show marked differences for positive and negative chirp and therefore a large difference in the fidelity values for positive or negative chirps. Figure 32(b) shows a comparison between the fidelity approach and a fast photodiode in measuring pre- and post-pulses in an amplifier. We find approximately similar sensitivity for both types of measurements. The inset shows how the oscilloscope waveform of the signal looks when the second Pockels cell delay time is set to 211.5 ns. The post-pulse can be seen at ~10 ns. Most commercial lasers have the same amount of dispersion in the regenerative amplifier per round trip, and therefore the appearance of pre- or post-pulses occurs near positive or negative 8,000 fs^2, respectively.

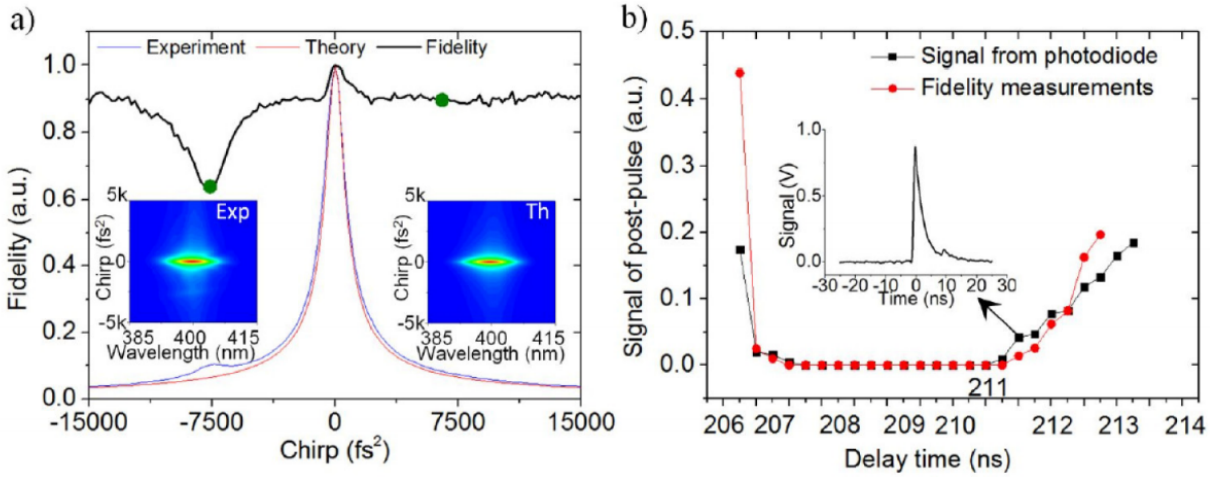

Figure 32. Fidelity measurements of a Ti:Sapphire amplifier with a post-pulse. The pair of insets in (a) shows experimental and theoretical 2D SHG chirp MIIPS scans. The fidelity parameters equal to 0.63 and 0.90 respectively (at the green dots). (b) Pre- and post-pulse detection using fidelity measurements and using a fast photodiode. The inset shows the oscilloscope waveform with a post-pulse ~10 ns after the main pulse.

2.2.4 Discussion and conclusion

We have performed fidelity measurements to characterize the random noise present in high repetition rate Ti:Sapphire femtosecond laser systems and have found that oscillators can be very quiet, with fidelity values approaching unity. On the other hand, we have found that regenerative amplifiers introduce spectral phase and amplitude bandwidth noise that reduces fidelity to ~0.95. By exploring situations that

decrease the fidelity of the amplified output, such as opening the stretcher to air and improper adjustment of Pockels cells, we showed that autocorrelation measurements for these situations fail to detect problems in the output. We demonstrate that fidelity measurements provide a robust approach to further characterize the output of ultrafast laser sources, especially for detecting spectral amplitude and phase noise, and for amplified systems to detect pre- or post-pulses.

Chapter 3 Standoff detection techniques. CARS spectroscopy

The ability to remotely identify trace quantities of materials is an ongoing challenge of high priority for many applications such as terrestrial field testing in outer space [144], combustion diagnostic [145], pollution mapping in atmosphere [146], and detection of explosives [147]. The latter application, discussed in this chapter, is intended to provide greater safety for the operator because it doesn't require direct or close contact with the materials under investigation like in the ion-mobility spectrometry (IMS) [148] or colorimetric kits [149]. Recent advances in the laser technology made a big step toward the developing of fast, label-free, noncontact, sensitive, selective, and safe systems for standoff chemical detection [147, 150-167]. Furthermore, the non-destructive acquisition of chemically resolved images would allow for follow up analysis by alternate methods and, when necessary, the collection of evidence.

In the Dantus Research Group we have developed a non-contact no-reagents system operating in the eye-safe 1560-1800 nm wavelength range for standoff trace detection of chemicals and high speed imaging based on CARS spectroscopy. Experimental results are provided for a number of chemicals on a variety of surfaces at sub-$\mu g/cm^2$ concentration. Chemically specific images were collected at 0.06 ms per pixel. Results from this effort indicate that the combination of modern industrial fiber lasers and nonlinear optical spectroscopy can address next generation eye-safe trace detection of chemicals.

This chapter has been adapted with permission from (Opt. Express **25**, 5832-5840 (2015)).

3.1 Experimental techniques for standoff detection

A wide variety of approaches have been explored, a testament to the difficulty of identifying sub-microgram per centimeter squared quantities of chemicals in the presence of a complex background on a variety of surfaces [147, 151]. Optical approaches, in turn, can be separated into two broad categories: linear and nonlinear. Linear processes include spontaneous Raman scattering, which is naturally enhanced for shorter wavelength lasers [158-161], IR absorption and diffuse scattering imaging spectroscopy [162-166]. Nonlinear optical methods take advantage of the coherent properties of lasers to enhance second- and higher-order optical processes, as in stimulated Raman processes [152-156], or for ablation and ionization of the sample as in laser-induced breakdown spectroscopy (LIBS) [157]. Some of the techniques are complimentary to each other. For example, IR absorption and Raman spectroscopies relate to the vibrational molecular motion, but both techniques are characterized by different selection rules.

The goal of all these efforts is to achieve fast (sub-second) imaging capable of detecting trace quantities of chemicals on a wide variety of surfaces and those which may be mixed in with many other chemicals. Ideally, this goal is achieved using a system that is eye-safe, or at least retina-safe. In this chapter, we have presented the development of a fast chemical-imaging system that shows great promise for eye-safe trace detection of chemicals, characterized by using wavelengths longer than 1400 nm according to the American National Standard for Safe Use of Lasers (ANSI) [168]. According to this document, the least amount of damage occurs due to the absorption of laser radiation in the vitreous body that protects the retina from exposure, see Figure 33. The lens in the eye does not focus the radiation, thus decreasing the thermal effect of water absorption. Exposure to the radiation in that spectral region may be harmful for the cornea and the lens, whereas the radiation in the region longer than 3 μm damages primarily the cornea.

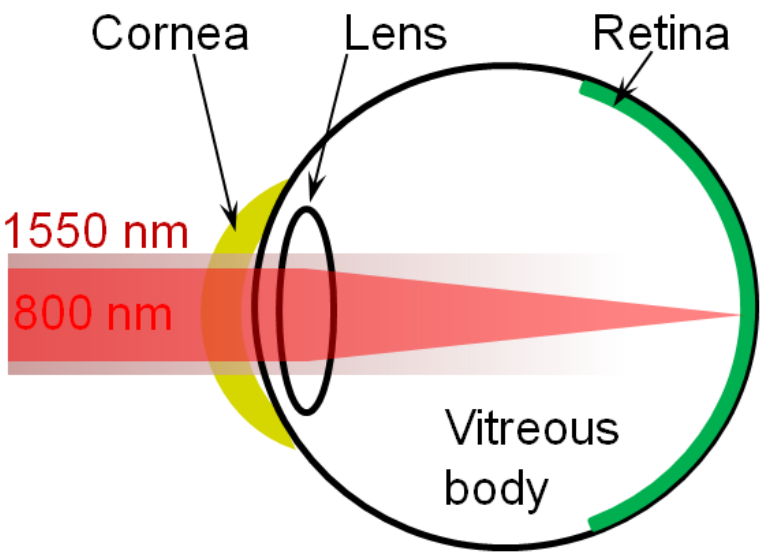

Figure 33. The sketch of an eye under the exposure to radiations from the eye-safe region (1550 nm) and outside that region (800 nm). Radiation at 1550 nm is not focused and it is absorbed by the vitreous body, whilst radiation at 800 nm is transmitted and focused on the retina, causing its damage.

Of the many spectroscopic methods available, infrared absorption, terahertz (THz) absorption, and Raman scattering can detect vibrational signatures useful for identifying specific chemicals in a complex chemical background. Vibrational features in Raman spectroscopy are naturally narrow (sub 5 cm^{-1}) with little or no background. Approaches based on absorption required the development of quantum cascade (QC) lasers, capable of producing very sharp lines that can be scanned in the millisecond time scale over vibrational bands of interest. Such lasers have made fast chemical imaging possible via backscatter or photothermal imaging [162-166]. Spontaneous Raman spectroscopy has the added advantage that it requires no laser tunability, but a disadvantage of having low efficiency ($<10^{-6}$). The intensity of the Raman signal, namely Stokes signal, is directly related to the secondary radiation emitted by the time-dependent induced dipole moment, and proportional to the power produced by such antenna:

$$I_S \propto N\left(\frac{\partial\alpha}{\partial Q}\right)^2 (\omega_0 - \omega_{vib})^4 \cdot I_0 , \tag{36}$$

where N is the number of scattering molecules and I_0 is the intensity of the incident radiation. The 4th-power frequency dependence of spontaneous Raman signals arises from spontaneous emission, as described by Einstein's coefficient for spontaneous emission Eq. (37),

$$A_{21} = \frac{16\pi^3 c}{3\varepsilon_0 h\lambda^3}\left|M_{21}\right|^2, \tag{37}$$

where λ is the wavelength of light, ε_0 is the permittivity of a vacuum, h is the Planck's constant, and M_{21} is the transition dipole moment. This wavelength dependence has led to great interest in the development of UV-Raman spectroscopy for trace chemical detection. In particular, systems using wavelengths shorter than 260 nm have been shown to avoid fluorescent signals [169] which can overwhelm the Raman signal. Conversely, near-infrared wavelength lasers have been considered impractical because the spontaneous Raman signal from a 1550 nm laser would be 1477 times weaker than the signal from a 250 nm laser, based on the inverse 4th-power wavelength dependence. Stimulated processes, such as CARS, do not have the same wavelength dependence because they are stimulated by the field. As such, they are described by Einstein's $B_{12} = B_{21}$ coefficients for stimulated processes, see Eq. (37), which lack the inverse wavelength dependence:

$$B_{21} = \frac{2\pi^3 c}{3\varepsilon_0 h^2}\left|M_{21}\right|^2. \tag{38}$$

One can thus deduce that longer wavelengths, such as the 1560 to 2000 nm region which is safest to skin and eyes [168], can be used for high sensitivity coherent Raman spectroscopy, avoiding the steep wavelength penalty of spontaneous Raman processes. Based on the above discussion, we use CARS for standoff detection of chemicals. Briefly, the CARS process (illustrated in Figure 34) involves coherent stimulated excitation of molecular vibrations by the pump and Stokes fields; the coherent vibrations formed in the ground state are probed by the probe beam. The resulting polarization results in the CARS emission. When broadband pulses are used, a Raman-like spectrum is obtained for all Raman transitions within the bandwidth of the pump and Stokes portion of the field, see Figure 34(b).

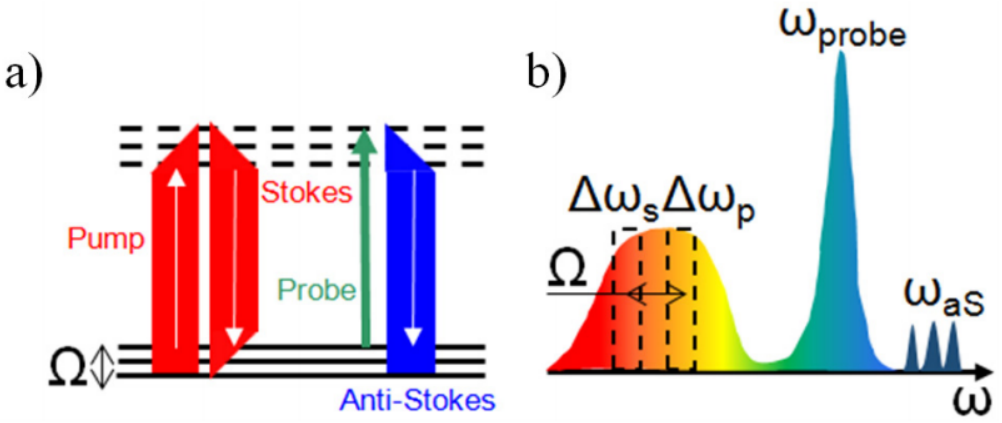

Figure 34. (a) Energy diagram showing how the redder wavelengths of the broadband laser spectrum act as both pump and Stokes to stimulate multiple Raman transitions (broad red arrows). The narrowband (green arrow) is the probe and leads to broadband anti-Stokes emission (broad blue arrow). (b) Broadband laser spectrum indicating how different portions act as pump $\Delta\omega_P$, Stokes $\Delta\omega_S$ and probe ω_{probe}. The diagram shows multiple Ω transitions probed simultaneously ω_{aS}.

Our approach involves coherent nonlinear spectroscopy, therefore we are interested in fields that coherently excite at certain energy levels, Ω, see Figure 34(a), through interaction with a broadband laser pulse:

$$\left|\int d\omega E(\omega)E^*(\omega-\Omega)\right|^2 = \left|\int d\omega A(\omega)A^*(\omega-\Omega_i)e^{i\varphi(\omega)-\varphi(\omega-\Omega_i)}\right|^2, \tag{39}$$

where $E(\omega)$ is the complex spectral field, Ω_i is a particular vibrational energy level, $A(\omega)$ is the field envelope, and $\varphi(\omega)$ is the spectral phase of the pulse. When the spectral phase function $\varphi(\omega)$ equals zero for all frequencies, the integral in Eq. (39) achieves a maximum value due to constructive interference among all different frequency pairs in the bandwidth that drive a particular vibration with frequency Ω coherently. A broadband source, Figure 34(b), can be used to obtain CARS signals from a single laser shot by using different spectral regions for the pump, Stokes, and probe [152, 154, 170].

In this process the probe beam is modulated by the coherent vibrations leading to emission proportional to the third-order susceptibility, $\chi^{(3)}$, which can be written as [171, 172]:

$$\chi^{(3)} = \frac{A_R}{\Omega_i - (\omega_{Pi} - \omega_{Si}) - i\Gamma_R} + \chi^{(3)}_{NR}, \tag{40}$$

where A_R is the Raman scattering constant, ω_{Pi} and ω_{Si} are pump and Stokes frequencies respectively, Γ_R is the line width and $\chi_{NR}^{(3)}$ is the nonresonant third-order susceptibility. Therefore, the induced third-order polarization can be approximated by the expression [170]:

$$P^{(3)}(\omega) = P_{NR}^{(3)}(\omega) + P_R^{(3)}(\omega)\,, \tag{41}$$

where

$$P_R^{(3)}(\omega) \propto \int_0^{+\infty} d\Omega \frac{1}{\Omega - \Omega_i - i\Gamma_R} E_{probe}(\omega - \Omega) \times \int_0^{+\infty} d\omega E_P^*(\omega) E_S(\Omega + \omega)\,, \tag{42}$$

$$P_{NR}^{(3)}(\omega) \propto \int_0^{+\infty} d\Omega \frac{1}{\Omega} E_{probe}(\omega - \Omega) \times \int_0^{+\infty} d\omega E_P^*(\omega) E_S(\Omega + \omega) \tag{43}$$

are the third-order resonant and non-resonant polarization components; $E_P(\omega)$, $E_S(\omega)$,and $E_{probe}(\omega)$ are the spectral amplitudes of the pump, Stokes and probe pulses respectively.

3.2 Nonresonant background

The total measured signal is a complex interplay between those two components shown in Eqs. (42) and (43) and in general, can have a significant nonresonant background. The nonresonant signal is the intrinsic property of the medium and originates from its electronic structure. In particular, the oscillations of electron cloud around nuclei are independent from Raman resonance at beat frequency, $\omega_P - \omega_S$, as it is shown in Figure 35 by dashed line.

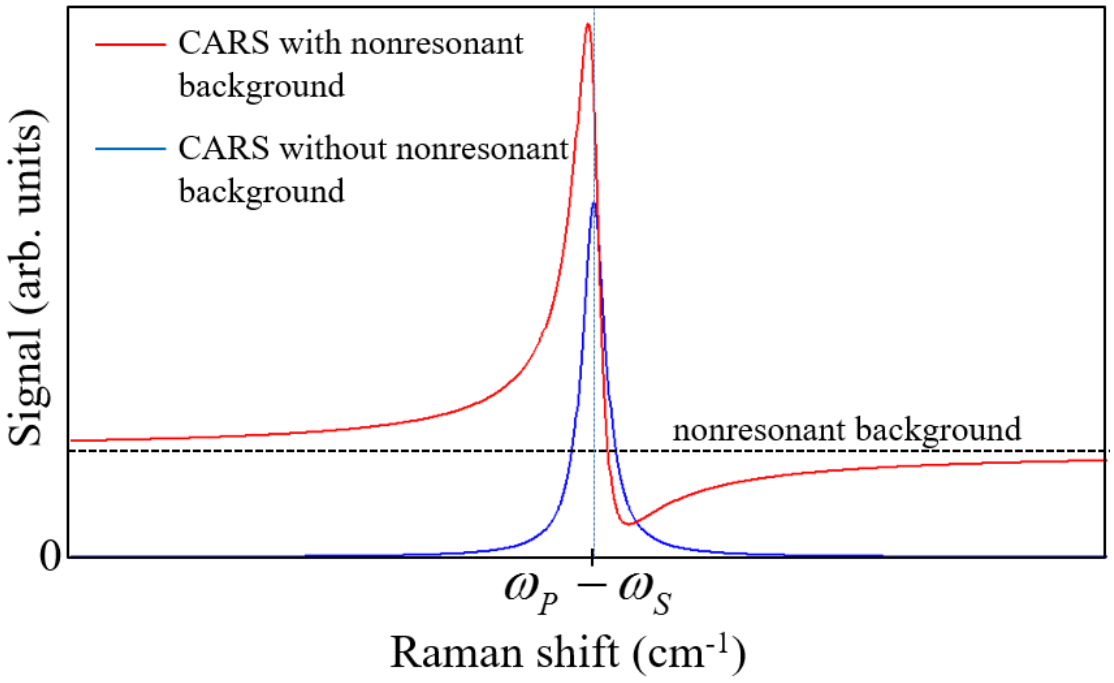

Figure 35. Coherent anti-Stokes Raman lines with (red) and without (blue) nonresonant background.

The CARS signal with nonresonant background is stronger than the signal without the background. It is due to the mutual contributions of electronic motion from nonresonant component and induced scattering from Raman vibrational mode, provided that phase between these two processes is locked. Nonresonant background imposes the asymmetry and shift on the CARS signal making the lineshape difficult to interpret. To minimize the non-resonant background, we used a probe pulse with perpendicular polarization [173, 174]. We also narrowed the bandwidth of the probe and delayed it from the pump and Stokes to obtained well-resolved CARS spectra[154]. In a published comparison CARS was shown to produce a 10^5 -10^6 times greater signal than spontaneous Raman scattering [175].

3.3 Experimental setup and results

The design of the laser system was predicated on the use of commercially available industrial fiber lasers, taking advantage of their compact size and reliability. We opted for wavelengths in the 1550-1800 nm range because this spectral region is considered the safest for eye and skin exposure [168], induce no fluorescence, and can be efficiently generated by an industrial fiber laser. We chose a fiber laser chirped-

pulse amplified system (Cazadero, Calmar Laser) generating 1.5 μJ sub-500 fs pulses at a 2 MHz repetition rate, with a bandwidth of 12 nm at full-width half-maximum at 1546 nm central wavelength. The output from this laser was split into two orthogonally polarized arms; the layout of the setup is shown in Figure 36. One arm (narrowband) was sent to a delay stage. The second arm was coupled into a photonic crystal (PC) rod (aeroChrome, NKT Photonics) with a 100 μm core diameter and 45 cm length. The anomalous dispersion of the PC rod leads to significant spectral broadening due to soliton fission and the soliton self-frequency shift effect [176, 177]. A pulse shaper (MIIPSbox640, Biophotonic Solutions Inc.) was used to select the pump and Stokes bandwidth with a slit at the Fourier plane and to compensate for the residual spectral phase of the soliton via the multiphoton intrapulse interference phase scan, pulse characterization and compression method [56, 111]. The spectrum of the laser system acquired with an optical spectrum analyzer (HP70950A) after combining the broadband and narrowband parts is shown in the Figure 36 inset. The beam was focused on the sample with a 75 mm focal length achromatic lens (L1) with a ~75 μm beam spot size at the $1/e^2$ intensity level. A pair of galvanometer-mounted mirrors (GVS012, Thorlabs) was used to raster scan the focused beam on a surface. The scattered light was collected 50 cm away with 2" diameter short focal length lens. The Raman signal was filtered out by a band-pass filter and focused on a photodiode (DET10N, Thorlabs). The electrical signal was then processed by a 600 MHz boxcar integrator (Zurich, UHF-BOX Boxcar Averager) with automated background subtraction. In terms of eye safety, we used 200 mW of 1546 nm laser pulses at 2 MHz with ~500 fs duration at the sample. The collimated beam diameter is ~3 mm, with a resulting power density of ~2.8 W/cm^2. According to [168], the maximum permissible exposure at this wavelength is 1 J/cm^2, therefore accidental exposure to the full beam for a second or longer could damage skin or the eye's cornea. Given that the person being exposed would feel the exposure, the time will likely be limited to a fraction of a second. Nevertheless, laser safety goggles with optical density (OD)>2 are recommended for system setup. For maximum safety, the system could be confined to a curtained region such as that used for x-ray scanning.

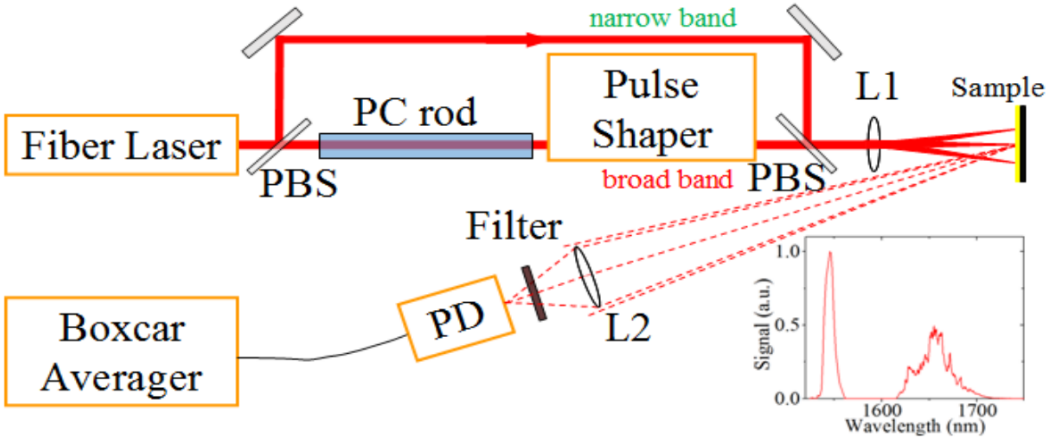

Figure 36. Experimental setup: L1, 2, are lenses; PBS is the polarizing beam splitter; PD is the fast photodiode. The inset shows a typical output spectrum after the second PBS. The delay stage and the scanning galvo-mirrors are not shown for simplicity.

The broadband pulse drives a vibrational coherence of the ground state and the narrowband pulse induces the third-order polarization responsible for the CARS blue-shifted emission. Figure 37 shows the spectra of both the narrow and broadband laser driving fields together with a typical CARS signal from powdered sulfur. We attenuated the laser pulses by 5 orders of magnitude to show them in the same scale with the CARS signal in Figure 37. Note that spontaneous Raman signal is not observed. This confirms that coherent Raman signals are orders of magnitude greater than spontaneous Raman signals at these wavelengths.

Initial experiments were carried out on sulfur powder, which has a strong Raman line at 217 cm^{-1} corresponding to the symmetric bend (umbrella) vibrational mode. Sub-microgram sensitivity was obtained as confirmed by imaging micron-sized particles weighing hundreds of nanograms (ng).

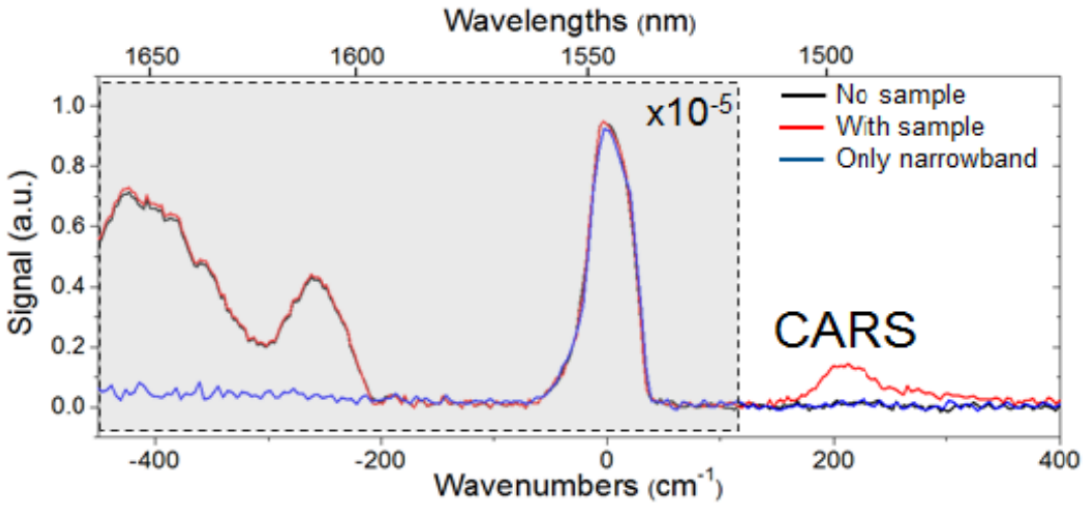

Figure 37. Spectra of narrowband and broadband laser parts and typical CARS signal (sulfur Raman line at 217 cm^{-1}). No spontaneus Raman signal is osberved from the narrowband pulses alone. The signal within the gray area corresponds to Rayleigh scattering from the substrate, attenuated by an OD5 filter. The signal for wavelengths shorter than 1525 nm corresponds to the CARS signal.

Quantitative assessment of speed and sensitivity of the system (shown in Figure 38(a)) was made by determining the number of laser shots (at 2 MHz) required for positive identification of micron sized particles of sulfur powder. Sample preparation is explained in Appendix B. We found that one-sigma (68.3%) is achieved at ~4 laser shots, two-sigma (95.5%) at 32 laser shots, and three-sigma (99.7%) at ~128 laser shots. Our laser scanner prevented us from speeds exceeding 0.06 ms/pixel, corresponding to 120 laser shots per pixel, however, a faster scanner would allow us to image several times faster. A single image of sulfur particles on a bare aluminum substrate obtained at the maximum speed is shown in Figure 38(c) and (d) without and with thresholding respectively.

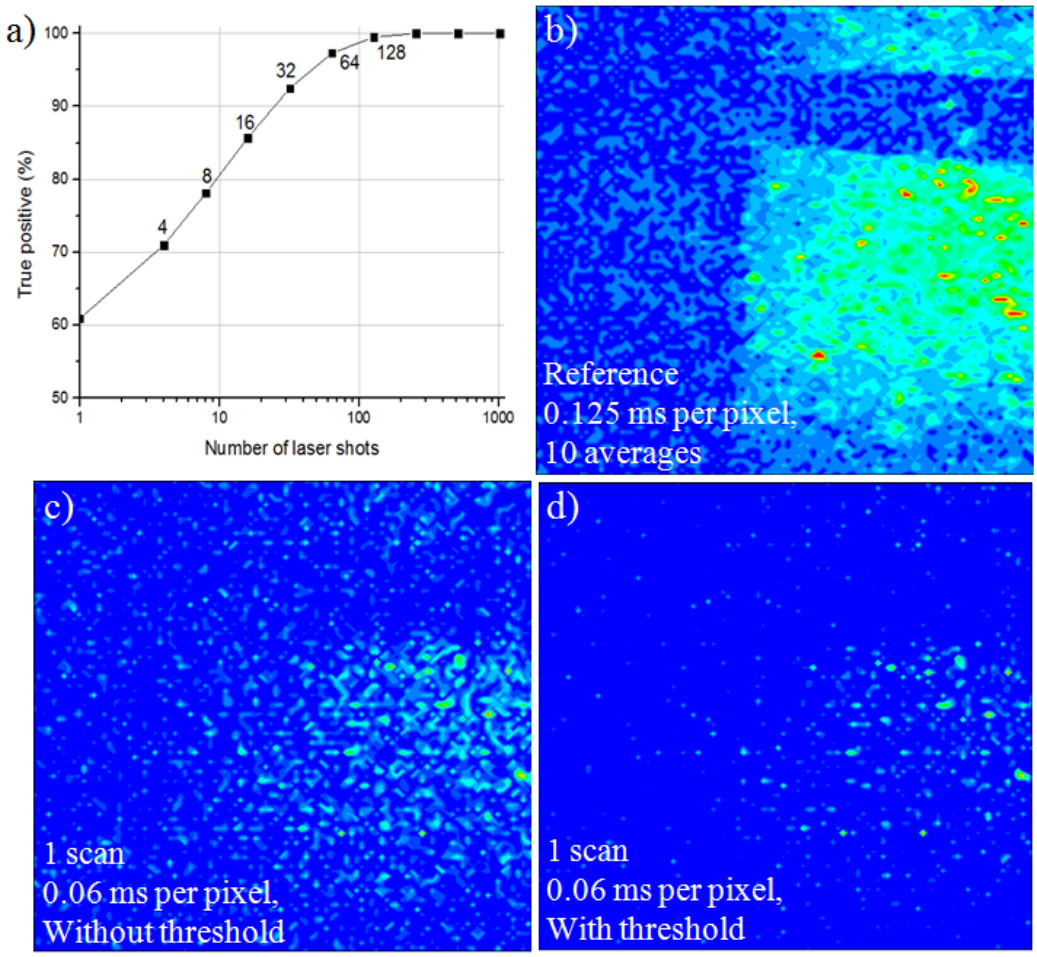

Figure 38. (a) Dependence between positive identification rate versus number of laser pulses in log scale. It shows that three-sigma probability is achieved with 128 laser shots at 2 MHz, which takes 0.06 ms per pixel. (b) Reference 100x100 pxl, 3x3 mm image (averaging of 10 scans) of sulfur particles (<75 μm diameter) on aluminum substrate, detecting the sulfur Raman line at 217 cm^{-1} obtained at 0.125 ms per pixel. The 100x100pxl, 3x3mm image (single scan) of sulfur particles (<75 μm diameter) on aluminum substrate, detecting the sulfur Raman line at 217 cm^{-1} obtained at 0.06 ms per pixel without a threshold (c) and with a threshold (d). Total acquisition time (0.6 s).

We imaged sulfur microparticles on an automotive panel, on the inside and outside surface of automotive glass, and on a nylon bag. The substrates were not prepared or cleaned for these measurements. Images 2×2 mm at 100×100 pixels were made at 0.25 ms per pixel, see Figure 39. For these measurements, we prepared natural fingerprints that included sulfur powder with a range in mass from 100 to 400 ng or sprinkled sulfur powder over the substrate. We observed clearly the sulfur Raman line at 217 cm^{-1},

without fluorescent interference from the car body panel as it would following excitation by UV or visible wavelengths.

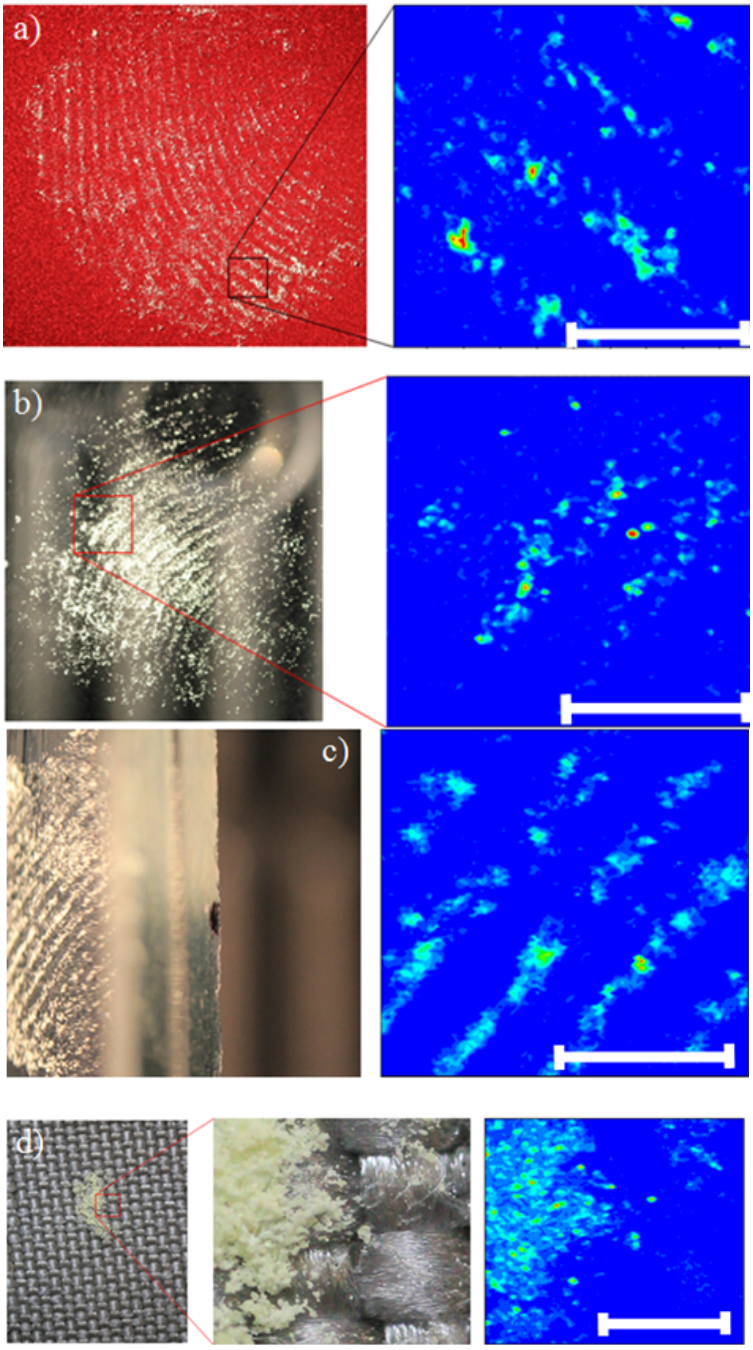

Figure 39. Images of sulfur microparticles, 2×2 mm, 100×100 pixels, obtained at 0.25 ms per pixel. (a) Sulfur fingerprint on a metallic red car body panel, showing average of 10 scans; (b) on the front and (c) back surfaces of a 6 mm thick laminated windshield, showing average of 5 scans. Note that (c) has a blurred edge showing both laser beam and Raman signal travel through a windshield. (d) Sulfur microcrystals on nylon, showing average of 20 scans. The scale bar is 1 mm.

Trace explosives detection included imaging potassium perchlorate crystals ($KClO_4$) on an aluminum plate and a car windshield as shown in Figures 40(a) and (b) respectively. The CARS signal corresponded to the potassium perchlorate Raman line at 463 cm^{-1}, which corresponds to a bending vibrational mode. We found the sensitivity for potassium perchlorate was lower than for sulfur, but we were able to detect one-microgram particles at 0.25 ms per pixel. Triacetone triperoxide (TATP) ($C_9H_{18}O_6$) microcrystals sublimed from a canine training swab were deposited and imaged on automotive glass, see Figure 40(c). The CARS signal at 300 cm^{-1} corresponded to the C-C-C bending vibrational mode of TATP.

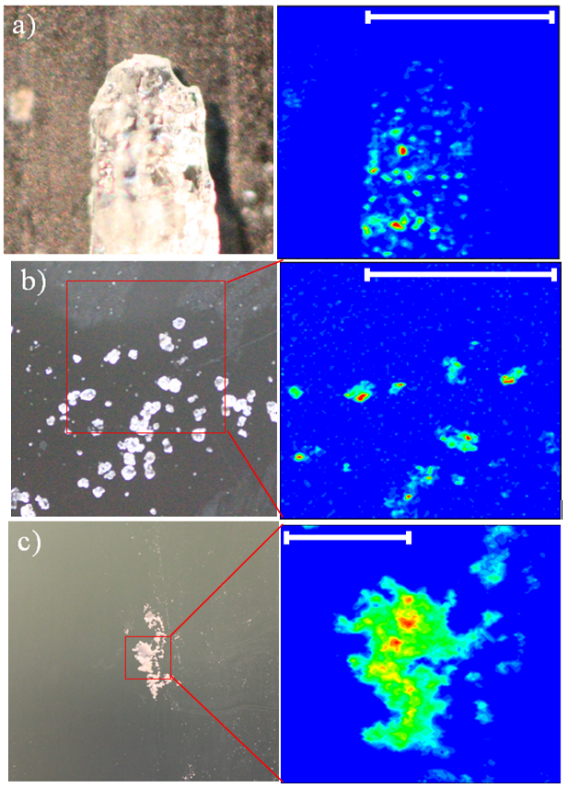

Figure 40. Images of potassium perchlorate and TATP. Potassium perchlorate images at 1.5×1.5 mm, 100×100 pixels obtained at 0.25 ms per pixel, showing average of 5 scans. (a) $KClO_4$ on aluminum substrate with a threshold correction of 1 STDev above the mean, (b) on a car windshield (6 mm thick), no threshold correction. (c) Image of TATP microparticles at 2×2 mm, 100×100 pixels at 0.25 ms per pixel on automotive glass (6 mm thick), showing average of 10 scans. The scale bar is 1 mm. Red square indicates the scanned region.

Detection results of ng quantities of sulfur are presented in the Figure 41. The system was optimized for the sulfur Raman line at 217cm^{-1} and was tested at two different scanning speeds, see Figure 41(c) and (d) for comparison. The picture of a sample is given in Figure 41(a). Given

that the sulfur density is 2.07 g/cm^3 the estimated masses for the sulfur particles in the red circles were calculated: 0.5 μg, 0.15 μg, 0.1 μg, and 0.4 μg.

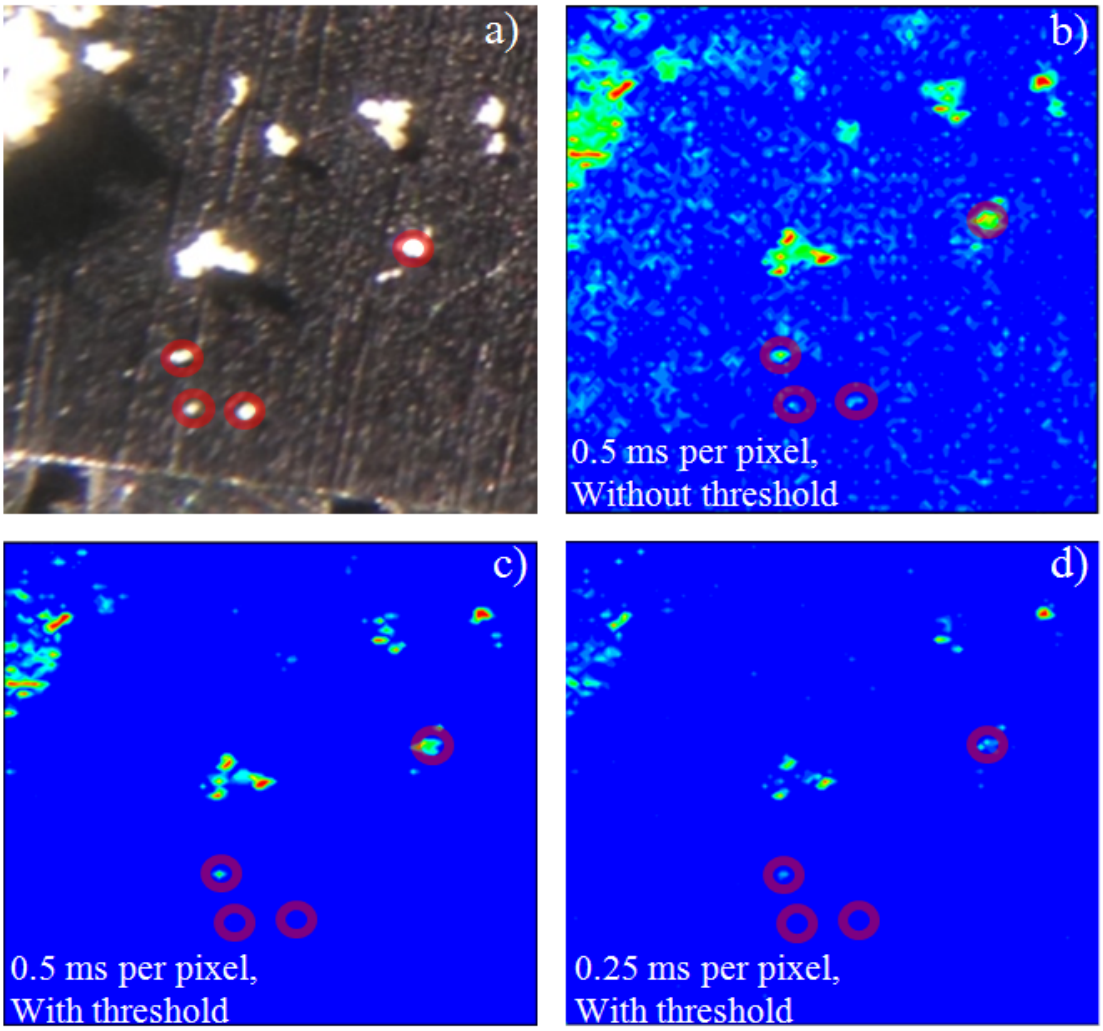

Figure 41. The 100x100 pxl, 1.5x1.5 mm images of sulfur powder, CARS signal on sulfur Raman line at 217 cm^{-1}. (a) Picture of sample; 1 mm scale from the ruler is shown in the bottom. (b) Image at 0.25 ms per pixel without threshold correction showing average of 20 scans, (c) with threshold correction and average of 20 scans. (d) Image at 2.5 ms per pixel with threshold correction and average of 10 scans. The particles shown by the circles correspond to crystals around 0.5 μg, 0.15 μg, 0.1 μg, and 0.4 μg from top to bottom and from left to right.

The speed of our method relies on using a fast photodiode at the expected Raman shift of the chemical being detected. These single photodiodes are inexpensive and multiple photodiodes can be used at Raman shifts of interest. When a full Raman spectrum is desired, we are able to obtain a stimulated Raman scan over the available bandwidth [152, 154, 170], in such cases the acquisition speed is limited

by the spectrometer 1 kHz for a fast acquisition system to 1 Hz for an optical spectrum analyzer (OSA) with rotating optics. A CARS spectrum with the three prominent Raman lines (scissors bending mode, rock mode, and symmetric stretch mode, A, B and C respectively) of liquid CCl_4 in a 1 mm cuvette is shown in Figure 42. The signal was collected in transmission by optical spectrum analyzer with a 1 Hz refresh rate.

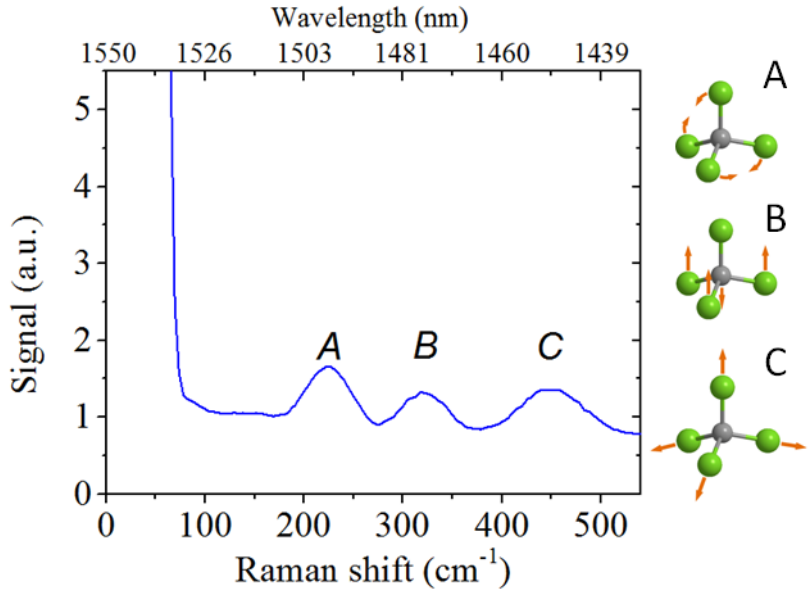

Figure 42. CARS spectrum of carbon tetrachloride. The different frequencies (A) 217 cm^{-1}, (B) 314 cm^{-1} and (C) 460 cm^{-1} correspond to the vibrational modes shown on the right. The wavelength axis (top) is not linear and is included for reference only.

3.4 Conclusion

In summary, an eye-safe laser based spectroscopic instrument capable of obtaining chemically resolved images of trace quantities has been demonstrated. A range of compounds deposited on a variety of unclean surfaces including bare metal, painted car panels, automotive glass, and nylon, were identified at a rate of 0.06 ms per pixel. This broadband CARS approach provides a Raman spectrum limited only by the bandwidth of the pump and Stokes spectrum, which, in this case, is limited to 540 cm^{-1}. When the backscatter CARS signal is detected by a spectrometer or an optical spectrum analyzer, we can acquire a CARS spectrum; in the absence of a spectrometer we are able to obtain a spectrum with a single photodiode by scanning the phase of the input laser. Both approaches have been demonstrated in previous

work from our group [152, 154, 170], where a 1 kHz laser system was used to acquire CARS spectra with excellent signal to noise ratio even with a single laser shot. In the present case, the 2 MHz system should accomplish the same signal to noise in ~1 ms. This approach for standoff detection requires raster scanning of the laser over the substrate. Using an array of photodiodes to detect a limited number of Raman lines would greatly enhance detection capabilities. The array of photodiodes would provide sufficient spectroscopic information (a 16-point spectrum at key spectral lines), that would permit identification with discrimination against false positives. A successful standoff sub-$\mu g/cm^2$ chemical sensing and imaging at high speed in the eye-safe spectral region on different substrates was demonstrated. Using an eye-safe industrial fiber based laser system greatly decreases the dimensions of the system making it a promising tool for implementing trace chemical detection.

Chapter 4 Femtosecond real-time probing of reactions

Over the past two decades, developments in laser technology and computational resources have brought us to a new level of photonic control and understanding of the most fundamental processes in physics, chemistry, and biology. In this chapter femtosecond transition-state (FTS) spectroscopy of sodium iodide, NaI, was studied taking advantage of modern lasers and pulse-shaping to better map the low-lying electronic states, some of which form predissociative wells through curve crossings. High-level ab initio multi-reference configuration interaction calculations including spin-orbit coupling terms and using large correlation-consistent basis sets were used to arrive at accurate ground- and excited-state potential energy curves of NaI. Density matrix calculations employing vibrational wave functions determined from the ab initio X 0^+ and A 0^+ potentials are used to simulate time dependent wave packet dynamics of NaI pumped to the A 0^+ state.

This chapter has been adapted with permission from ("Femtosecond real-time probing of reactions MMXVII: The predissociation of sodium iodide in the A 0^+ state," Chem. Phys. Lett.**, in press** (2017)).

4.1 Introduction

One of the initial publications on the femtosecond real-time observation of transition states in a chemical reaction [6] demonstrated how femtosecond laser pulses could open a window to explore the spectroscopic transformation of reagents into products. In the case of cyanogen iodide (ICN), dissociation of the I-CN bond occurred directly, see Figure 43. This bond breakage process does not always happen directly because there is a possibility of a crossing between the electronic states which results in interference. Observation of the wave packet oscillations during the dissociation of alkali halides [178] provided a clear example of predissociation, see Figure 44, showing that femtosecond pulses could reveal spectroscopic information that was very difficult to obtain by other methods. Among the alkali halides, sodium iodide became a paradigm molecule in investigating dissociation reactions after the development of femtosecond spectroscopy [179-184]. This, in turn, triggered substantial follow-up work further exploring, theoretically as well as experimentally, the dynamics of sodium iodide [185-191].

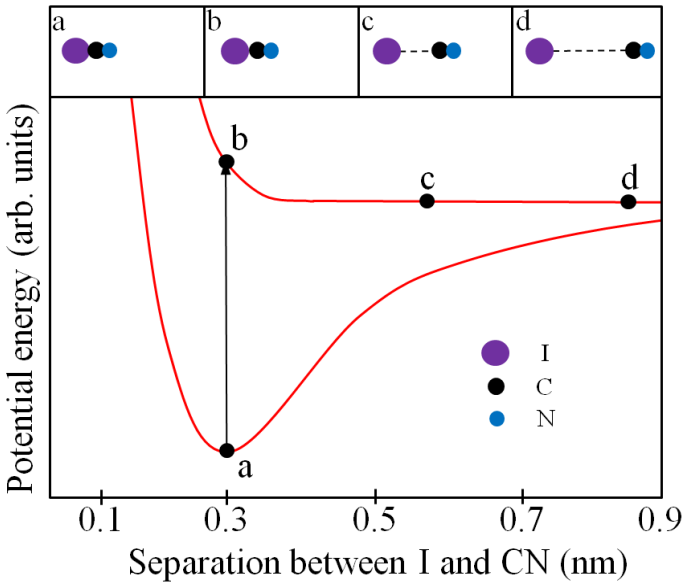

Figure 43. Photodissociation reaction of cyanogens iodide (ICN) into iodine and cyanide. Top insets correspond to the dynamics of I-CN bond at different positions a, b, c, and d on the potential-energy curves.

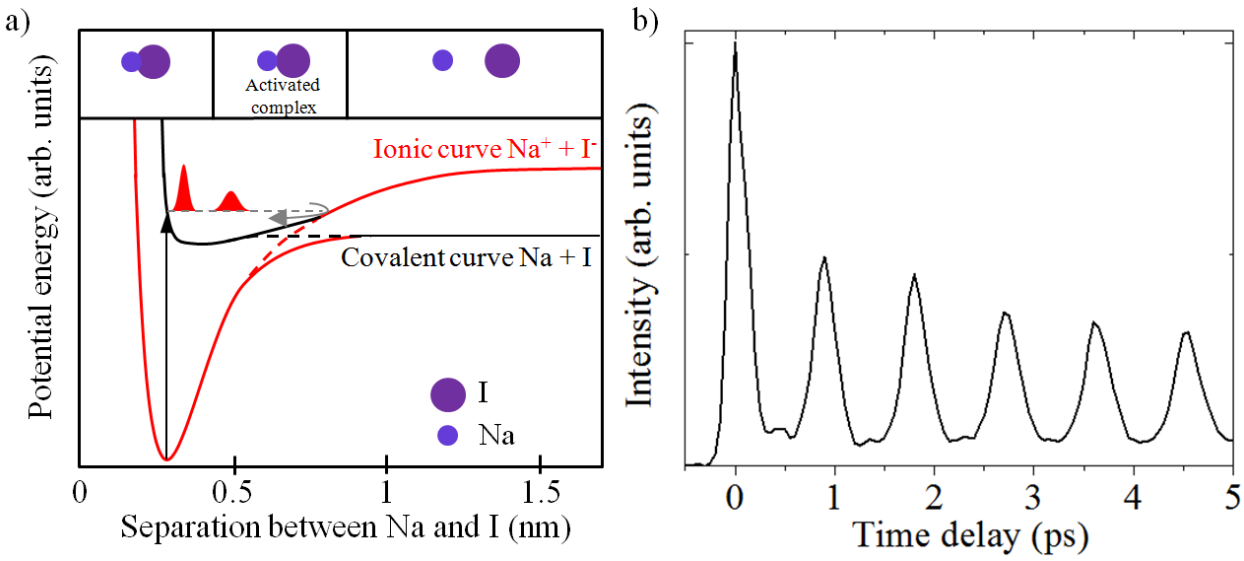

Figure 44. Femtosecond dynamics of sodium iodide molecule. (a) Potential-energy diagram showing the crossing between the ionic and covalent curves. Direct excitation from ground-state potential to the quasi-bound potential, shown by arrow. Sodium iodide can dissociate into sodium and iodide atoms when on a covalent curve or it can be in a high-energy bound state and alternate between two curves. The wave packet evolution, red pulses, oscillates within the adiabatic well. (b) Coherent excitation of activated complex can probe oscillations of the wave packet with FTS method.

A number of frequency- and time-resolved experiments have been aimed at mapping the ground and lower excited states of NaI. Nevertheless, the discrepancies in the description of the excited A 0^+ state, especially near the bottom of the A 0^+ well still remain. In this work a thorough examination of the lower vibrational energy levels in the A 0^+ state and their predissociation dynamics have been carried out. Both time- and frequency- resolved measurements were analyzed and ab initio electronic structure calculation were performed. The recent major advances in laser technology, pulse shaping techniques, and computational resources allows us to provide the most accurate description of the lower electronic states of NaI, especially the A 0^+ state, to date. First, we used the solid-state kilohertz repetition-rate Ti:Sapphire regeneratively amplified femtosecond laser that is much more stable than the 20 Hz system used by Zewail's group in 1988, which had 8 different laser dye circulators, with solutions that had to be refreshed on a weekly basis. Secondly, we utilized a pulse shaper and MIIPS technique which is capable of measuring and compressing the pulses to their transform-limited duration automatically [40, 50, 192, 193]. Thirdly, we used fast computers and better quantum chemistry algorithms compared to 1988. We

employ highly efficient version of the ab initio multireference configuration interaction (MRCI) methodology with the explicit inclusion of spin-orbit (SO) interactions, coupled with large and carefully optimized correlation-consistent basis sets, to arrive at accurate ground- and excited-state potential energy curves (PECs) of the NaI system. These energy curves are subsequently used to determine vibrational term values and wave functions. The MRCI method was chosen because it can be applied for highly accurate global potential energy surfaces calculations, for conical intersections and non-adiabatic effects.

4.2 Experimental and computational details

The experiments were performed using a regeneratively amplified Ti:Sapphire laser system (Spectra Physics, Spitfire) producing 40 fs pulses at a central wavelength of 798 nm with 0.8 mJ pulse energy at a repetition rate of 1 kHz. The experiments were run using the pump-probe method. The output pulses from the amplifier were split in a Mach-Zehnder interferometer with adjustable optical delay stage and were spatially recombined by a dichroic mirror, see Figure 45.

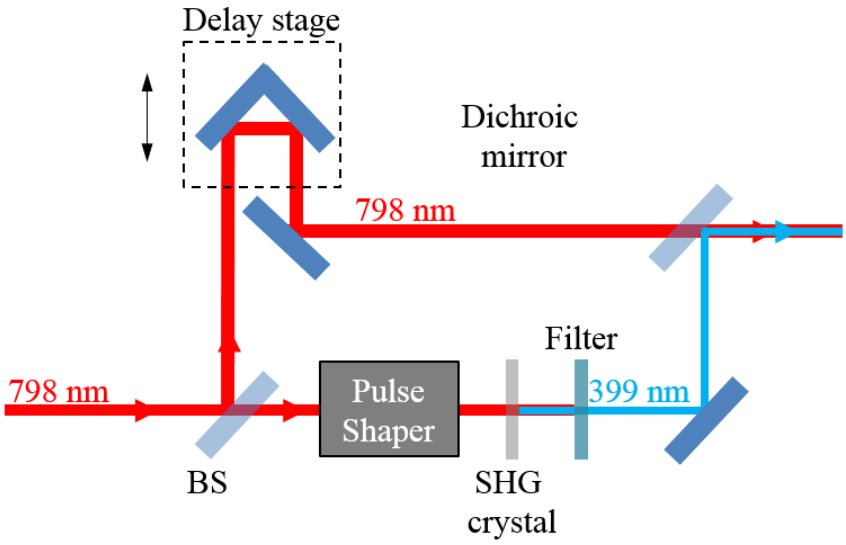

Figure 45. Mach-Zehnder interferometer. BS is a beam splitter.

The pump pulse with a central wavelength of 399 nm and transform-limited 30 fs pulse duration was prepared from the output of the pulse shaper [58] followed by a second harmonic generation crystal. The probe pulse with a central wavelength of 798 nm and 45 fs pulse duration was derived from a partial

reflection of the beam prior to entering the pulse shaper. For all the experiments, the polarization angle between pump and probe pulses was set at magic angle 54.74° in order to avoid contributions from rotational motion dynamics. Sodium iodide was sealed in vacuum inside a quartz cell; the quartz cell was heated in a cylindrical oven to 873 K, see Figure 46. The entire oven was insulated by ceramic bricks in order to thermally insulate that region of the optical table and keep the nearby laser system stable. For pump-probe experiments, the pump wavelength was derived from the second harmonic of the Ti:Sapphire laser resulting in 3.107 eV (25,063 cm^{-1}) pulses that reach the A 0^+ state by a single-photon transition. The probe wavelength was the fundamental of the laser at 798 nm, promoting the excited wave packet through a one-photon resonance to states correlating with the Na + I dissociation channel corresponding to sodium doublet. The pump and probe beams were focused into the cell by a 225 cm focal length lens.

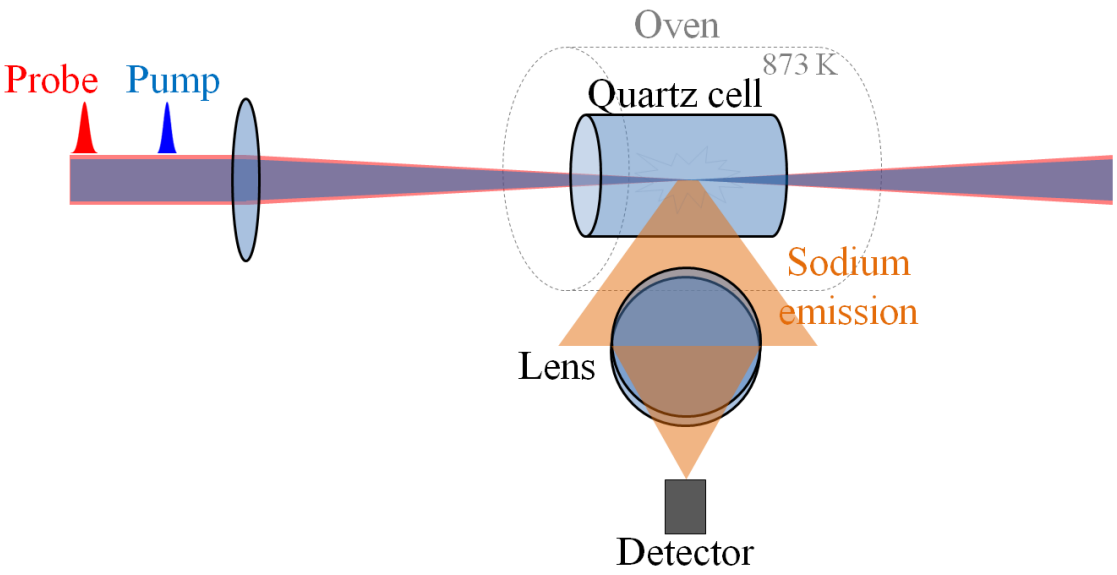

Figure 46. Schematic of the optical setup used in pump-probe experiment on NaI dissociation.

The fluorescence of sodium atoms (sodium doublet near 589.3 nm) was detected as a function of time-delay using a compact spectrometer (QE65000, Ocean Optics). Pump and probe laser intensities were attenuated until they had negligible contribution to the detected signal. For long time scans (greater than 5 ps) we used a conventional optical delay line. For short time scans (less than 5 ps) we used the pulse shaper to scan the arrival time of the pump pulse. Power dependence measurements were carried out to

ascertain that the signal arises from linear excitation from the ground X 0^+ state to the excited A 0^+ state. For experiments where the pump spectrum was tuned, we took advantage of the pulse shaper to introduce a phase that would cause the SHG spectrum to become sharper and to tune it to different wavelengths because of multiphoton intrapulse interference [40].

The electronic structure calculations of the PECs were performed using internally contracted MRCI approach [194-196] based on the complete active-space self-consistent field (CASSCF) [197, 198] reference wave functions resulting from the state-averaged (SA) CASSCF calculations, incorporating SO interactions at the MRCI theory level. The calculations were performed on a dense augmented polarized valence correlation-consistent aug-cc-pV*n*Z basis sets with *n*= T, Q, and 5 were employed [199]. In addition to the electronic structure calculations, we determined the vibrational term values of the X 0^+ and A 0^+ states using the MRCI/AVnZ + SO PECs by numerically integrating the radial Schrödinger equation for the Na and I nuclei using the Numerov–Cooley algorithm [200] found in Le Roy's Level 8.2 program [201].

4.3 Results

Excitation at 399 nm (3.107 eV) and probing at 798 nm (1.554 eV) would have been inconceivable 20 years ago given that the bottom of the A 0^+ state was thought to be near 3.15 eV [7]. Furthermore, probing required a resonance with a state correlating with excited state sodium (Na*), approximately 2 eV in excitation energy. Nevertheless, such a transient is shown in Figure 47 with time-delay steps between pump and probe of 50 fs. We observe oscillations with a mean vibrational period of 907 fs, corresponding to 36.77 cm^{-1} vibrational spacing. The oscillatory motion decays with a biexponential having lifetimes of 3.7 ± 0.3 ps (α = 0.45) and 21.2 ± 1.3 ps (α = 0.55), where α is the pre exponential factor. Fast Fourier-transform (FFT) and maximum entropy method (MEM) [202] analysis of the oscillations leads to the determination of the mean vibrational frequency of 1.1025 THz. High temporal resolution experimental data, shown in Figure 48, were obtained by using the pulse shaper to generate the time delay between pump and probe pulses.

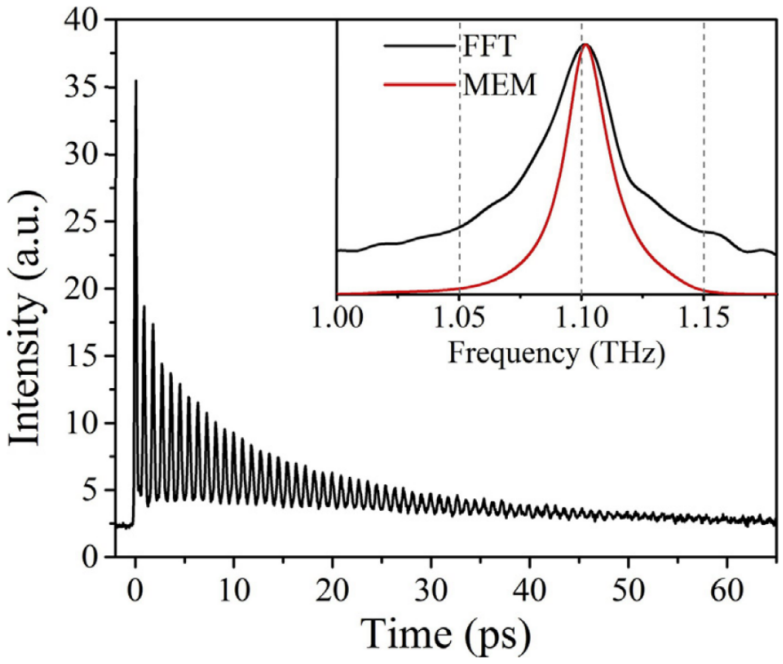

Figure 47. Experimental FTS transient obtained with 399 nm pump and 798 nm probe laser wavelengths. The inset shows FFT and MEM analysis of the time-resolved transient showing the average vibrational state contributions.

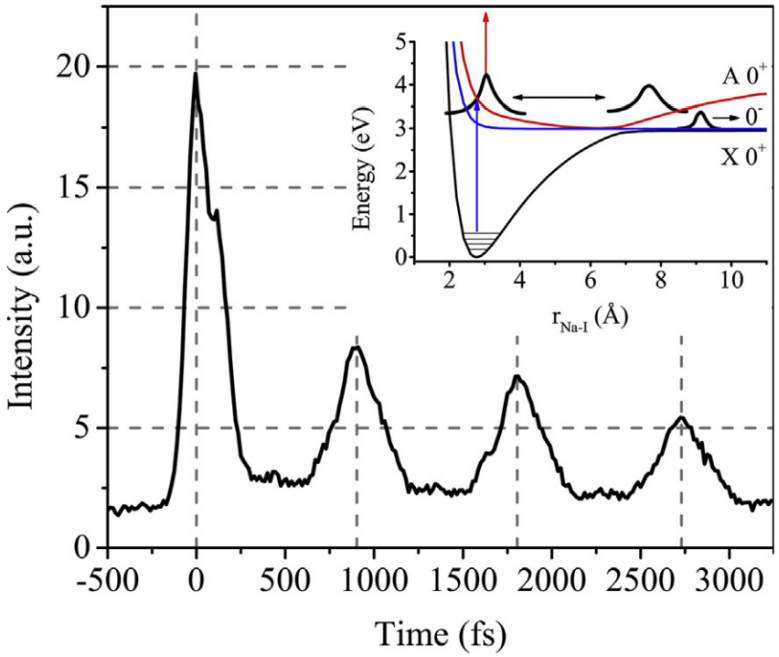

Figure 48. High resolution experimental FTS transient obtained with 399 nm pump and 798 nm probe laser wavelengths. In this case the probe laser was delayed by the pulse shaper in 15 fs steps. The inset shows the schematic of the relevant MRCI/AV5Z + SO potential energy curves contributing to the signal being detected. From this transient it is clear that probing takes place near the inner turning point of the A 0^+ potential.

The shaper allows us to generate arbitrary time steps that can be as small as 10 attoseconds. In this case, we scanned the probe pulse with a step size of 15 fs. The scan was carried out up to the first 3 ps. From this scan, we confirm that the oscillation period of the wave packet is 908 fs and we further observe that the timing is consistent going back to time zero, when pump and probe pulses are overlapped. We take this fact to confirm that probing with 798 nm pulses takes place near the inner turning point of the wave packet, very close to the Franck-Condon (FC) region where excitation takes place. Furthermore, analysis of the intensity of the time-zero feature indicates that approximately 56% of the excited molecules reach the A 0^+ state while the remaining 44% leaks through the crossing region.

The predissociation time for NaI has been one of the key dynamics measured. At the energy of excitation in this study probing the lower-energy part of the A 0^+ potential, the rate of escape from the A 0^+ state is expected to be significantly slower than that found by Zewail using 311 nm pulses. Here we explore within a limited range the wavelength dependence of the escape rate. We used two different wavelengths of excitation, 395 nm (blue) and 402 nm (red) pump wavelengths, while the 798 nm probe laser wavelength and bandwidth were unchanged. Frequency tuning was achieved by introducing a sinusoidal function using the pulse shaper and this resulted in the modified spectrum [40]. Results from those measurements with different excitation spectra are shown in Figure 49. The energy difference between the two pulses corresponds to 471 cm^{-1}. Biexponential fitting to the data finds a lifetime for the blue excitation of 2.2 ± 0.3 ps (α = 0.45) and 18.1 ± 1.1 ps (α = 0.55), while for the red wavelength the corresponding constants were 2.7 ± 0.5 ps (α = 0.45) and 20.0 ± 1.8 ps (α = 0.55). The difference in the predissociation rate amounts to 13%. FFT and MEM analysis show that the mean vibrational frequency that is associated with the blue pump is 1.102 THz whereas that with the red pump is slightly larger with a value of 1.104 THz.

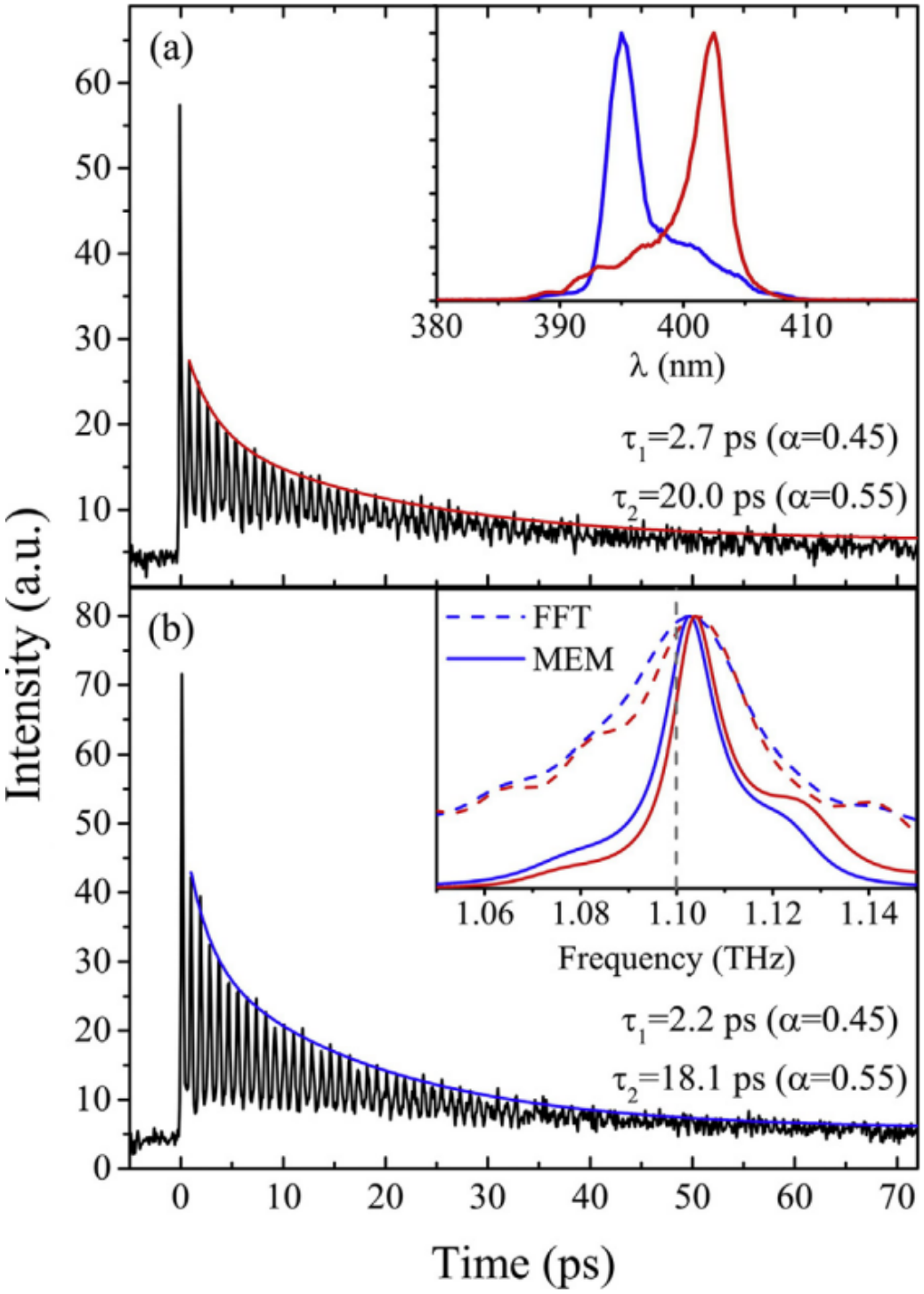

Figure 49. Experimental FTS transient obtained with (a) 402 nm (red spectrum in the inset of (a)) and (b) 395 nm (blue spectrum in the inset of (a)) pump wavelengths and 798 nm probe laser wavelengths with exponential fitting. The inset of (b) shows the FFT (dashed) and MEM (solid) from the 402 nm (red) and the 395 nm (blue) pump wavelength.

The MRCI/AV5Z + SO calculations have yielded potential energy curves for the grounded state (X 0^+), adiabatic potential curve for the state A 0^+, and the state B 0^+, see Figure 50. From an experimental point of view, it is useful to point out the large difference between the equilibrium bond lengths characterizing the X 0^+ and A 0^+ states, which is approximately 3.5 Å. For such a large difference between the respective r_e values, we can anticipate that the lowest vibrational levels of the A 0^+ state are not accessible from the lowest vibrational levels of the X 0^+ state.

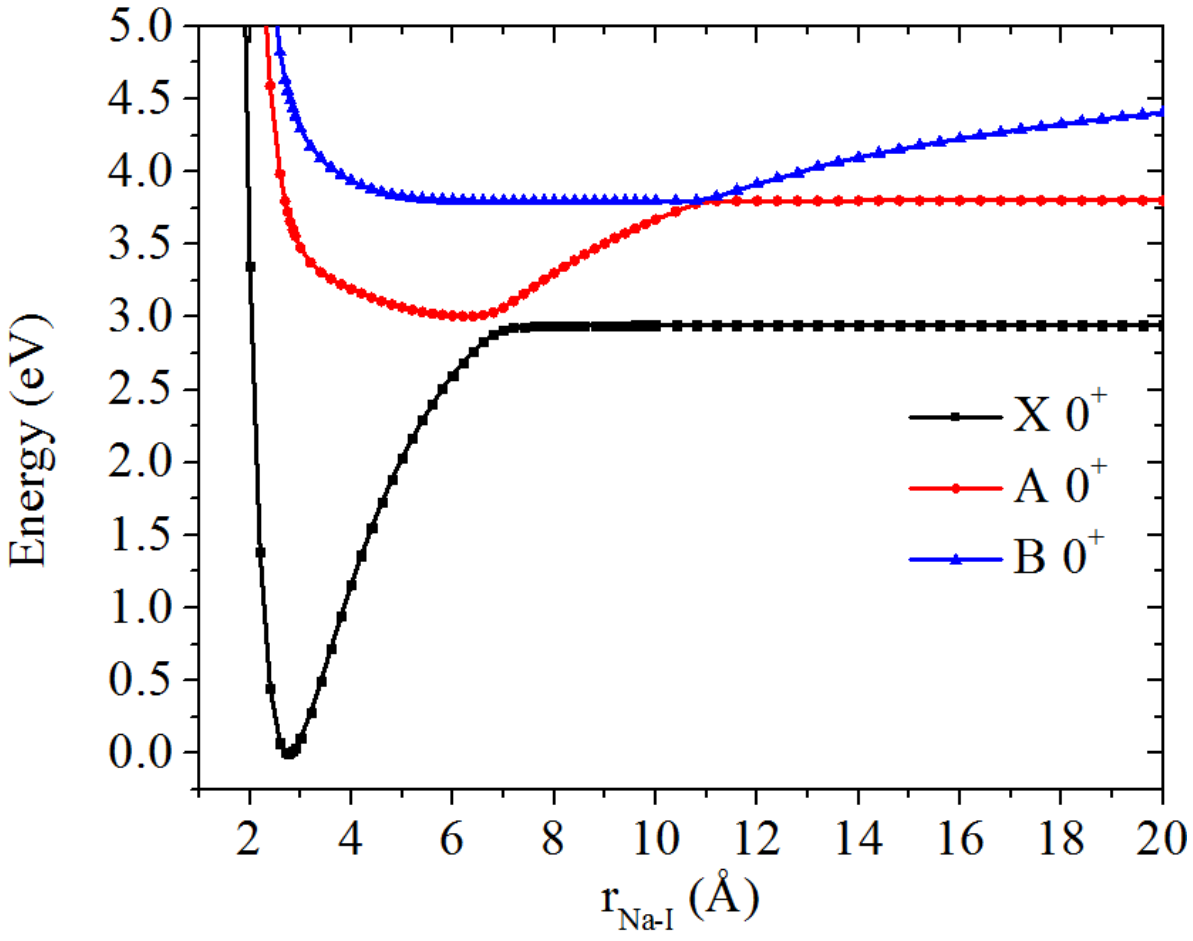

Figure 50. Potential energy curves of NaI obtained in the MRCI/AV5Z + SO calculations.

In addition to the vibrational energies, we also calculated the corresponding vibrational wave functions. From these, we calculated FC factors and, using a density matrix formalism, simulated the nuclear wave packet dynamics in the A 0^+ state. As anticipated, we have found that the large difference in r_e values characterizing the X 0^+ and A 0^+ PECs is so large that the FC factors for the excitations from the

lower v" states in the X 0^+ state to the lower v' states in the A 0^+ state are extremely small. We multiplied the calculated FC factors from theory and used a Boltzmann distribution of the v" states, taking into account that the experiment was conducted at 873 K, and found out that, on average, the majority of the excitations take place from v" = 8–10 to v'= 70–90. By computing the aforementioned density matrix, we determined the effective wave packet dynamics in the A 0^+ state and its evolution, which are shown in Figure 51.

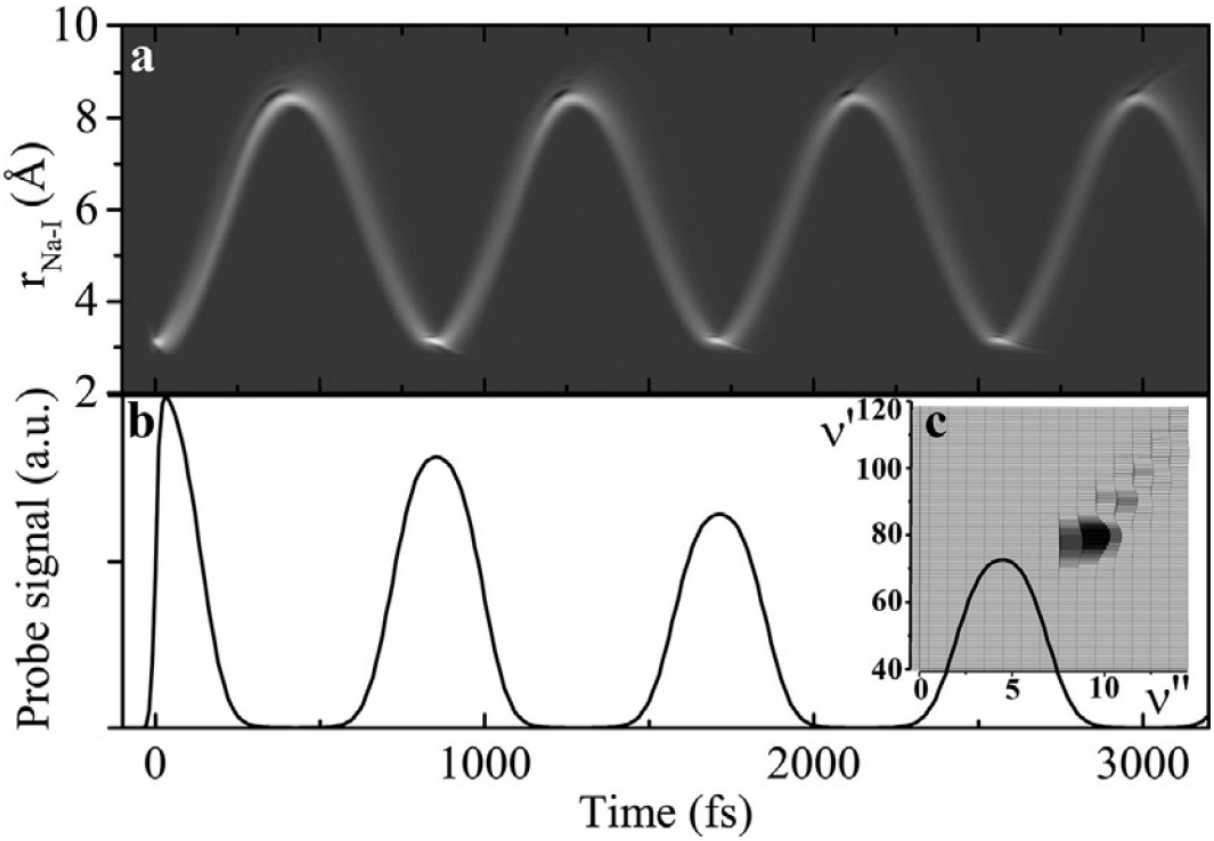

Figure 51. (a) Calculated wave packet dynamics using the density matrix formalism described in the text. Limited wave packet dephasing is observed given the low anharmonicity of the vibrational levels reached. (b) Pump-probe simulation of the wave packet dynamics with an additional exponential decay. (c) FC and Boltzmann population weighted transition probabilities between the ground and excited states given transform-limited pulses as used for obtaining experimental data in Figures 47 and 48.

4.4 Discussion

The NaI system and its predissociation have been studied in great depth for many years, especially after Berry published the initial PECs [203]. Zewail's work [7, 178-182, 184] provided the first observation of

quantum beats during the predissociation and showed that by tuning the energy of the pump one could map the relevant PECs. It was observed that for pump energies above 3.6 eV the oscillation period increased, indicating very large anharmonicity associated with the outer turning point of the Coulomb potential. Below 3.6 eV, the period was found to be wavelength independent. The shape of the A 0^+ state below 3.8 eV remained a mystery despite several time- and frequency-resolved spectroscopy measurements and ab initio calculations. This collaborative work with the Prof. Piecuch Research Group, Department of Chemistry at Michigan State University, combines technical and theoretical advances to provide important new information about the lower excited states of the NaI system, especially the A 0^+ state. We have begun by combining the information about the FC factors involving vibrational wave functions determined from best ab initio X 0^+ and A 0^+ potentials obtained in the MRCI/ AV5Z + SO calculations, accounting for the Boltzmann distribution of the vibrational states in the X 0^+ state at the experimental temperature, and the spectrum of the pump pulse. We have found that at the experimental temperature of 873 K the FC factors corresponding to the vibronic X 0^+ (v'') $\rightarrow$A 0^+ (v') transitions with low values of v'' and v' are so small that such transitions can safely be neglected. Significant excitations occur only when v'' is 8–10. In this case, the maximum transition probabilities involve v'= 70–90 levels. According to calculations, the wave packet is formed at the internuclear distance of about 3 Å, having an excess energy above the bottom of the A 0^+ well of about 3,200 cm^{-1}. The calculations clearly indicate that the very large difference in r_e values characterizing the X 0^+ and A 0^+ potentials makes the v'= 0–60 vibrational states inaccessible by a single photon excitation. These findings regarding vibrational levels in the A 0^+ state accessible in the experiment are consistent with the photoabsorption cross sections calculated by Alekseyev et al. [187]. These findings are also relevant to the work of Tiemann and co-workers, who thoroughly examined the bottom of the A 0^+ well [204]. In Tiemann et al.'s work, results from different experiments and calculations were critically evaluated to arrive at the A 0^+ potential that is very similar to the one calculated here. For example, the r_e value characterizing the A 0^+ state determined by Tiemann et al. of 6.052 Å is in very good agreement with MRCI/AV5Z + SO calculations, which give 6.260 Å. The avoided crossing between the X 0^+ and A 0^+ states resulting from MRCI/AV5Z + SO

calculations occurs at 6.8 Å, in good agreement with the previously reported information as well, while the energy gap between the two states at this distance is only somewhat larger than the values reported in Ref. [187].

Finally, the density matrix dynamics wave packet simulations based on MRCI/AV5Z + SO potentials, taking into account information about the spectra of pump pulses employed in these experiments and thermal population of the initial vibrational states in the X 0^+ state, were carried out to simulate the observed wave packet dynamics in the A 0^+ state. It was found that the wave packet evolution is very harmonic, which agrees with the fact that a very harmonic region of the A 0^+ potential is excited (see Figure 51). This leads to reduced wave packet dephasing and the possible role it could play in determining the escape of the wave packet from the well. The dynamics calculations in this work are in very good agreement with experiment. The period obtained in the wave packet dynamics simulations based on the ab initio potentials, calculated in this work, is 850 fs (see Figure 51). This is only about 6% faster than the period found experimentally (see Figure 48). While this small difference can be attributed to the numerical precision of the calculations reported in this work, we believe that one of the main reasons for the observed discrepancy is the aforementioned strong interaction between the X 0^+ and A 0^+ states near the avoided crossing, which may translate into effective broadening of the A 0^+ potential well, allowing the penetration of a wider range of Na-I distances by the wave packet during oscillations i.e., longer periods, while increasing the rates of escape. The relatively large rotational temperature of the NaI molecules after excitation may play a role here too.

In this work, the programmable femtosecond pulses were utilized to obtain high-quality time-resolved data, which were then used to guide theoretical calculations in the sense of determining what level of theory is required to reach reasonable agreement with experiment. Careful investigation of sodium iodide was performed, with a focus on the A 0^+ state. The nature of this state and its contribution to the dynamics of the system is still interesting and not conclusively understood, despite intense efforts from a number of groups. The new insights from the present joint experimental and theoretical

investigation help to explain some of the mystery and perhaps more importantly lay the groundwork for future experiments directly probing the bottom of the A 0^+ well.

Chapter 5 Conclusions and Outlook

The work in this thesis is one more step towards understanding and controlling ultrafast laser matter interaction using recent advances in laser technology, photonic control devices, computational resources, and effective quantum chemistry algorithms. This chapter summarizes the research projects and main results presented throughout this dissertation. In particular, I studied 1) generation of rectangular-shaped pulses using phase-only modulation of fundamental spectrum, 2) two successive projects on the characterization of pulse-to-pulse stability of high-repetition rate pulsed laser sources, 3) an eye-safe approach for standoff trace detection of chemicals based on coherent Raman scattering, and 4) femtosecond transition-state spectroscopy of sodium iodide using modern lasers, pulse-shaping, and high-level ab initio multi-reference configuration interaction calculations.

5.1 Square-shaped pulse generation

An analytical solution was derived to generate square-shaped pulses in the time domain for essentially any spectrum using phase-only modulation. The experimental test of this approach was carried out on a Ti:Sapphire laser system producing 40 fs laser pulses with a Gaussian spectrum. We demonstrated the conversion of 40 fs pulses into pulses of 150 times longer duration with sharp front and trailing edges. This method does not cause any spectral bandwidth loss and is absolutely reversible. Square-shaped pulses have many applications, especially in the mitigation of self-action processes in optical fibers and effective pumping for OPCPA systems which, in turn, can be used for seeding free-electron lasers. Having an analytical solution for the spectral phase can be used for designing dispersive optics for stretching/compressing specifically manufactured for the particular spectral profile.

5.2 Pulse-to-pulse stability measurements of high-repetition rate pulsed lasers

We identified a parameter that could be easily measured to determine quantitatively the noise characteristics of a laser source. The measurement is based on the dependence of an integrated nonlinear optical process on a spectral phase, such as chirp, can be used to determine the expected performance of an ultrafast laser source. The proposed measurement is particularly useful when performance is compromised by random noise in the laser. The measurement bypasses autocorrelation based methods which are dominated by the coherence time of the pulses leading to a coherent spike. The fidelity parameter $\langle F \rangle$ is expressed in terms of values that can be practically measured in the laboratory. Experimental measurements on a commercial Ti:Sapphire oscillator and a regenerative amplifier were presented. Fidelity measurements could be used to benchmark the performance of ultrafast lasers. In addition, fidelity can be measured actively and used as a feedback for active improvement of a laser source. We found that one is able to determine the physical mechanism (spectral amplitude or phase fluctuations) responsible for noise by examining the shape of the fidelity curve. We have provided a direct correlation between the fidelity value and the expected attenuation of second order processes such

as SHG, three-photon excited fluorescence, or THG. In the future, the fidelity measurements may be tested on other pulsed laser systems to determine the pulse-to-pulse stability.

5.3 Coherent Raman spectroscopy for standoff detection

Chemical identification of trace quantities of explosives is determined by coherent Raman spectroscopy. While spontaneous Raman spectroscopy has been used for chemical detection for decades, there are multiple advantages to our system. First, the system described in Chapter 3 uses an eye-safe laser operating at long wavelengths. Spontaneous Raman is very inefficient and the inverse wavelength to the fourth dependence makes it impossible to use at wavelengths longer than 1400 nm. Here, we show that stimulated Raman process does not have this wavelength restriction and is enhanced by approximately a factor of a million over spontaneous Raman. Therefore, this system provides robust signals at high-speed scanning rates. Second, the justification of the system performance is given in terms of Einstein's coefficients of stimulated and spontaneous emission. Lastly, the system can detect various traces of chemicals on car panels, car windshields and nylon.

Having demonstrated promise, we hope to extend the coherent Raman excitation bandwidth beyond the present 540 cm^{-1} limit and to increase selectivity by taking advantage of optical parametric amplification technology for the generation of a broad spectrum. We can multiplex several detectors to capture multiple CARS signals with every laser shot. Alternatively, we can use a fast spectrometer to acquire complete Raman spectra at kilohertz rates. Therefore, we believe our approach can serve as a fast screening of a wide variety of chemicals. If a CARS spectrum is needed for further identification the system can incorporate a spectrometer that could acquire such a spectrum in a fraction of a second.

5.4 Femtosecond transition-state spectroscopy on sodium iodide

Ultrafast photochemical dynamics in NaI were studied in Chapter 4 by detecting laser-induced fluorescence. The bond dissociation dynamics of NaI was described in detail. Photodissoiation dynamics were accomplished by using a short femtosecond pump pulse of ~ 30 fs to initiate a quantum mechanical wave-packet in the excited state and a 40 fs probe pulse used to promote the wave packet to an excited

state from which excited state sodium atoms fluoresce. The excited-state dynamics of the lower vibrational level A 0^+, led to the observation of wave packet dynamics traversing the curve crossing region. One of the important extensions of the work will be to probe the wavelength region where the B 0^+ state contributes to the wave packet dynamics. Excitation of the B 0^+ state will also allow us to explore multi-pulse strategies to reach the bottom of the A 0^+ well.

APPENDICES

Appendix A: Matlab code for square-shaped pulse generation

The Matlab code for the phase-only generation of a square-shaped pulse with pulse duration of *T* is presented below. In the numerical simulation, the duration, *T*, was chosen to be 3,000 fs. The method works well for a stretching ratio greater than 10.

```
clc;
clear all;

ii=(-1)^(0.5); %imaginary unit
lamda0=800; % central wavelength [nm]
pi=3.14159; % constant
c=300; % speed of light [nm/fs]
taup=40; % initial pulse duation in FWHM [fs]
tau0=taup*(2*(log(2))^0.5)^(-1); %Gaussian convolution factor, see G. Agrawal Nonlinear fiber optics
2nd edition
n=4096; %number of points

%Defining the temporal range
np=100; % factor for time axis range
tmax=taup*np; % time axis range
tmin=-tmax;
dt=(tmax-tmin)/(n-1); % time step
t=tmin+dt*(0:n-1); % time range

GaussT=exp(-((t.^2)/(2*tau0^2))); % Gaussian pulse envelop
Intt=GaussT.^2; % Gaussian intensity profile
figure (1)
set(gcf, 'Color', [1,1,1]);
plot(t,Intt,'LineWidth',5)
set(gca,'FontSize',16)
xlim([-100,100]);
title('Figure 1. Pulse intensity profile','FontSize', 16);
xlabel('Time (fs)','FontSize', 16);
ylabel('Intensity (arb.units)','FontSize', 16);
%_____

omega0=2*pi*c/lamda0; % the central frequency [rad]
w=2*pi*(-n/2:1:n/2-1)/(dt*n);% frequency range centered at zero
w=omega0+w; % frequency range centered at omega0
Spec=fftshift(fft(GaussT)); % Fourier transform to obtain spectrum

lamda=2*pi*c./w;% wavelength range
Intw=(abs(Spec).^2)/max(abs(Spec).^2);% normalized spectrum
figure(2)
set(gcf, 'Color', [1,1,1]);
plot(lamda,Intw,'r','LineWidth',5);
set(gca,'FontSize',16);
xlim([760,840]); % wavelength range for Ti:Sapphire laser
```

```
title('Figure 2. Spectrum of a Ti:Sapphire laser','FontSize',16);
xlabel('Wavelength (nm)','FontSize',16);
ylabel('Intensity (arb.units)','FontSize',16);

Intw=fliplr(Intw);% spectral array is flipped to match frequency range

Intw=Intw./trapz(w,Intw); % normalization
MAXind=find(Intw == max(Intw(:))); % find index of the maximal value in spectrum
coeff=3000; % desired pulse duration for square pulse [fs]

Int1=cumtrapz(w,coeff*Intw); % first integral
Int1=Int1-Int1(MAXind);% DC component subtracted


Int2=cumtrapz(w,Int1); % second integral
Int2=Int2-Int2(MAXind);% DC component subtracted

figure(3)

subplot(1,2,1) % plot first integral
set(gca,'FontSize',16)
set(gcf, 'Color', [1,1,1]);
hold on
plot(w,Int1,'LineWidth',5)
title('Figure 3. First integral','FontSize',16);
xlabel('Frequency (rad)','FontSize',16);
ylabel('Signal (arb.units)');
plot(w,Intw*225-1500,'r','LineWidth',5);
xlim([2.2,2.5]);
hold off
legend('First integral','Spectrum','FontSize',14);

subplot(1,2,2) % plot second integral
set(gca,'FontSize',16)
set(gcf, 'Color', [1,1,1]);
hold on
plot(w,Int2,'LineWidth',5)
title('Figure 3. Second integral','FontSize',16);
xlabel('Frequency (rad)','FontSize',16);
ylabel('Signal (arb.units)','FontSize',16);
plot(w,Intw*15,'r','LineWidth',5);
xlim([2.2,2.5]);
hold off
legend('Phase','Spectrum','FontSize',14);

PhaseOmega=Int2;

Eomega=(Intw.^0.5).*exp(ii*PhaseOmega); %  spectral field with a phase

Et=fftshift(fft(Eomega)); % Fourier transform to time domain
Intensity=((abs(Et)).^2)/(max(((abs(Et)).^2)));% Intensity profile
```

```
figure (4)
set(gca,'FontSize',16)
set(gcf, 'Color', [1,1,1]);
hold on
plot(t,Intensity,'b','LineWidth',5)
title('Figure 4. Square-shaped pulse','FontSize',16);
xlabel('Time (fs)','FontSize',16);
ylabel('Intensity (arb.units)','FontSize',16);
xlim([-2500 2500]);
plot(t,Intt,'k','LineWidth',5)
hold off
legend('Stretched pulse','Initial pulse','FontSize',14);
```

The results are shown in Figures (52)-(55).

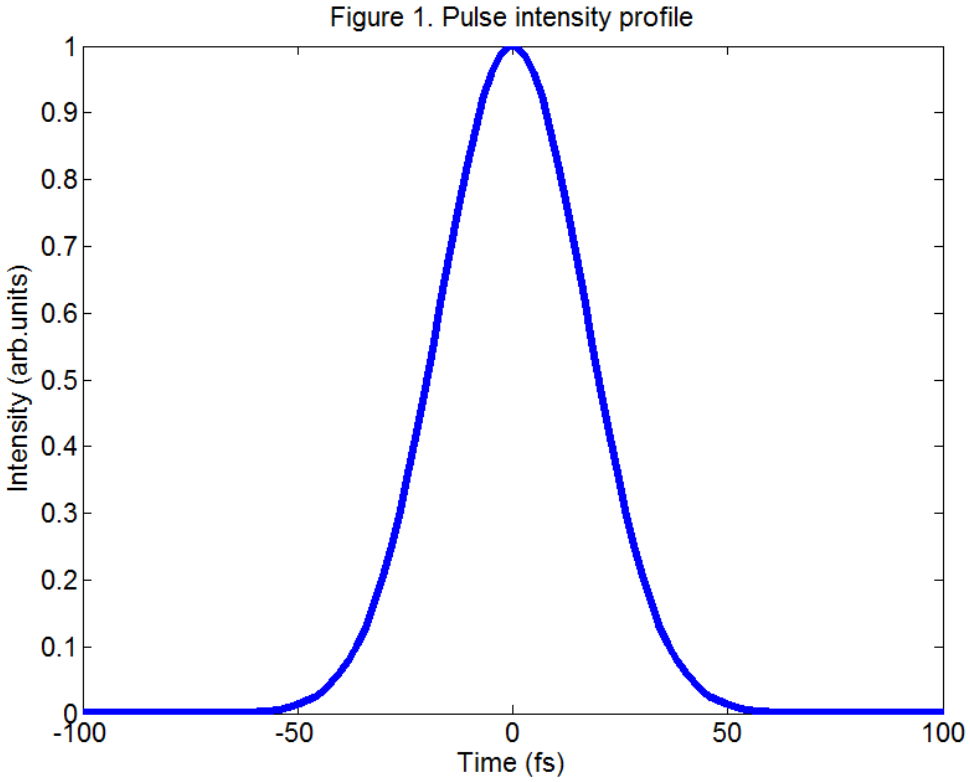

Figure 52. Temporal profile of the 40 fs laser pulse measured at FWHM.

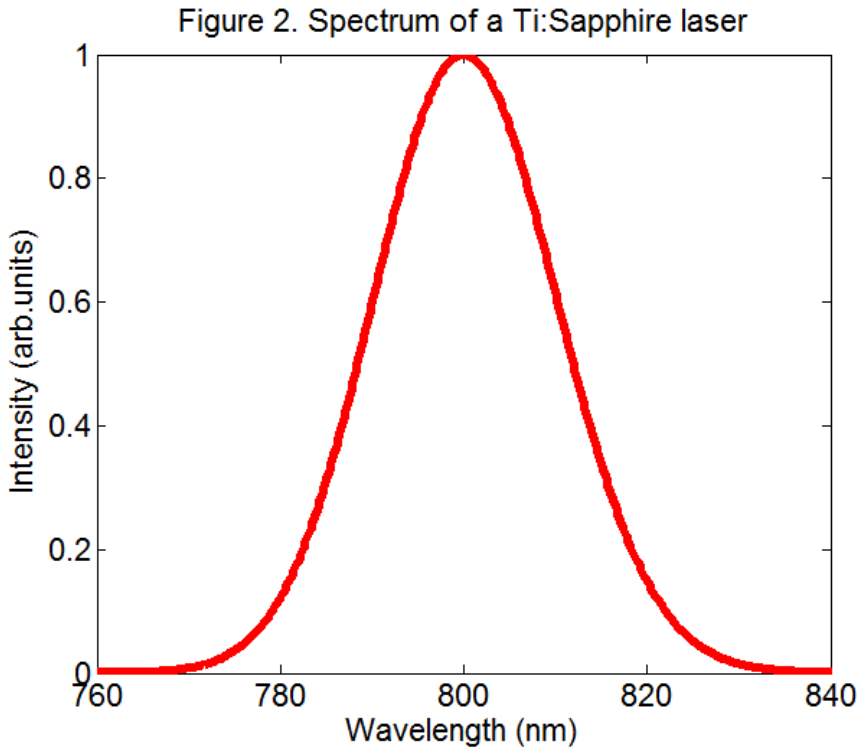

Figure 53. Laser spectrum corresponding to a 40 fs laser pulse measured at FWHM with the central wavelength of 800 nm.

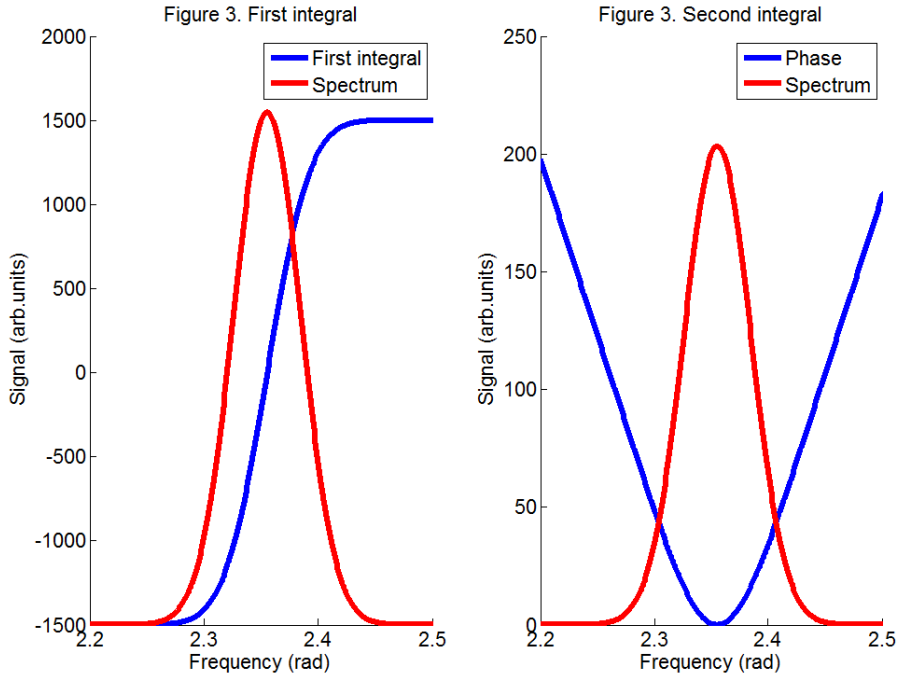

Figure 54. The blue line corresponds to the first (left) and the second (right) integrals of the laser spectrum shown in Figure 53.

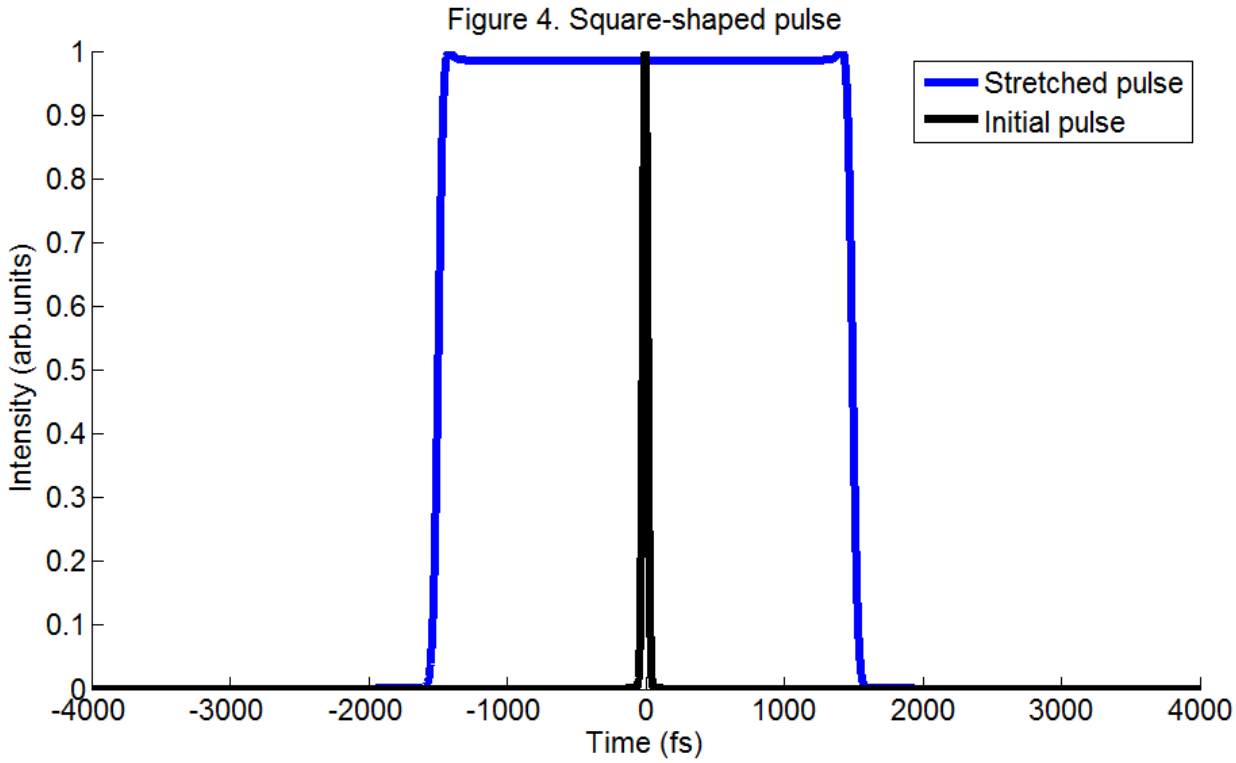

Figure 55. Square-shaped pulse profile in time domain (blue). Initial pulse (black) is shown for reference.

The analytical solution proposed for the generation of the square-shaped pulses in Chapter 2 can also be applied in the generation of positively or negatively skewed pulses with a prominent trailing or leading pulse pedestal in the time domain. Such pulses can be utilized in studies related to the dissociative ionization [55]. This work by M. Nairat et al. showed that an ion yield can be significantly increased if one uses high-order spectral phase to generate a pulse temporal profile with a pedestal. At pulse intensities of less than 10^{15} W/cm^2 the influence of the pedestal is negligible, but at higher power levels, as shown by U. Lev et al. [205], the pedestal facilitates the dissociation process by pre-aligning the molecule along the electric field. The Matlab code is shown below.

```
clc;
clear all;

ii=(-1)^(0.5); %imaginary unit
lamda0=800; % central wavelength [nm]
pi=3.14159; % constant
c=300; % speed of light [nm/fs]
```

```
taup=40; % initial pulse duation in FWHM [fs]
tau0=taup*(2*(log(2))^0.5)^(-1); %Gaussian convolution factor, see G. Agrawal Nonlinear fiber optics
2nd edition
n=4096; %number of points

%Defining the temporal range
np=100; % factor for time axis range
tmax=taup*np; % time axis range
tmin=-tmax;
dt=(tmax-tmin)/(n-1); % time step
t=tmin+dt*(0:n-1); % time range

GaussT=exp(-((t.^2)/(2*tau0^2))); % Gaussian pulse envelop
Intt=GaussT.^2; % Gaussian intensity profile
%_____

omega0=2*pi*c/lamda0; % the central frequency [rad]
w=2*pi*(-n/2:1:n/2-1)/(dt*n);% frequency range centered at zero
w=omega0+w; % frequency range centered at omega0
Spec=fftshift(fft(GaussT)); % Fourier transform to obtain spectrum

lamda=2*pi*c./w;% wavelength range
Intw=(abs(Spec).^2)/max(abs(Spec).^2);% normalized spectrum

Intw=fliplr(Intw);% spectral array is flipped to match frequency range

Intw=Intw./trapz(w,Intw); % normalization
MAXind=find(Intw == max(Intw(:))); % find index of the maximal value in spectrum
coeff=3000; % desired pulse duration for square pulse [fs]

Int1=cumtrapz(w,coeff*Intw); % first integral
Int1=Int1-Int1(MAXind);% DC component subtracted

Int2=cumtrapz(w,Int1); % second integral
Int2=Int2-Int2(MAXind);% DC component subtracted

PhaseOmega=Int2;

shift=40;
PhaseOmega_no_l=PhaseOmega(shift:end);
PhaseOmega_r=PhaseOmega(length(PhaseOmega)-shift:end)+(PhaseOmega(length(PhaseOmega))-
PhaseOmega(length(PhaseOmega)-shift));
PhaseOmega_leftShift=cat(2,PhaseOmega_no_l,PhaseOmega_r);
PhaseOmega_leftShift=PhaseOmega_leftShift(2:end-1);

Eomega_skewL=(Intw.^0.5).*exp(ii*PhaseOmega_leftShift);
Et=fftshift(fft(Eomega_skewL)); % Fourier transform to time domain
Intensity=((abs(Et)).^2)/(max(((abs(Et)).^2)));% Intensity profile

figure (5)
set(gca,'FontSize',16)
```

```
set(gcf, 'Color', [1,1,1]);
hold on
plot(t,Intensity,'b','LineWidth',5)
title('Figure 5. Triangle-shaped pulse','FontSize',16);
xlabel('Time (fs)','FontSize',16);
ylabel('Intensity (arb.units)','FontSize',16);
xlim([-2500 2500]);
plot(t,Intt,'k','LineWidth',5)
hold off
legend('Negative skew','Initial pulse','FontSize',14);

PhaseOmega_no_r=PhaseOmega(1:end-shift);
PhaseOmega_l=PhaseOmega(1:shift)+(PhaseOmega(1)-PhaseOmega(shift));
PhaseOmega_rightShift=cat(2,PhaseOmega_l,PhaseOmega_no_r);

Eomega_skewR=(Intw.^0.5).*exp(ii*PhaseOmega_rightShift);
Et=fftshift(fft(Eomega_skewR)); % Fourier transform to time domain
Intensity=((abs(Et)).^2)/(max(((abs(Et)).^2)));% Intensity profile
figure (6)
set(gca,'FontSize',16)
set(gcf, 'Color', [1,1,1]);
hold on
plot(t,Intensity,'b','LineWidth',5)
title('Figure 6. Triangle-shaped pulse','FontSize',16);
xlabel('Time (fs)','FontSize',16);
ylabel('Intensity (arb.units)','FontSize',16);
xlim([-2500, 2500]);
plot(t,Intt,'k','LineWidth',5)
hold off
legend('Positive skew ','Initial pulse','FontSize',14);
```

The results are shown in Figures (56) and (57).

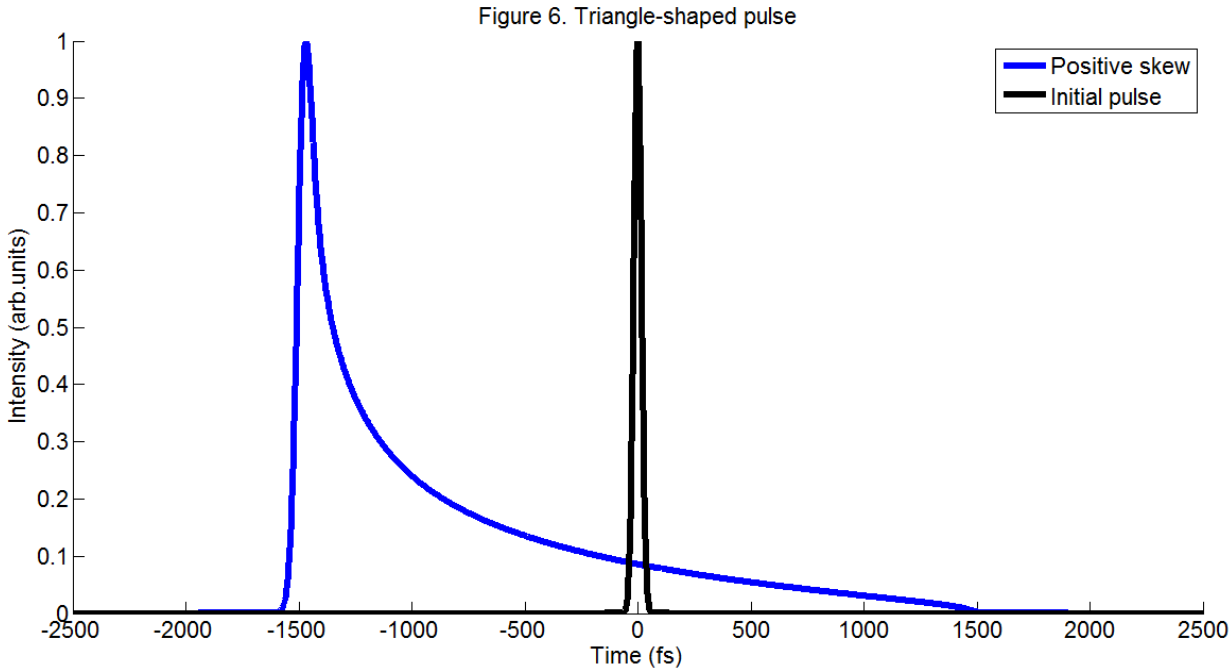

Figure 56. Positively skewed pulse profile in time domain (blue). Initial pulse (black) is shown for reference.

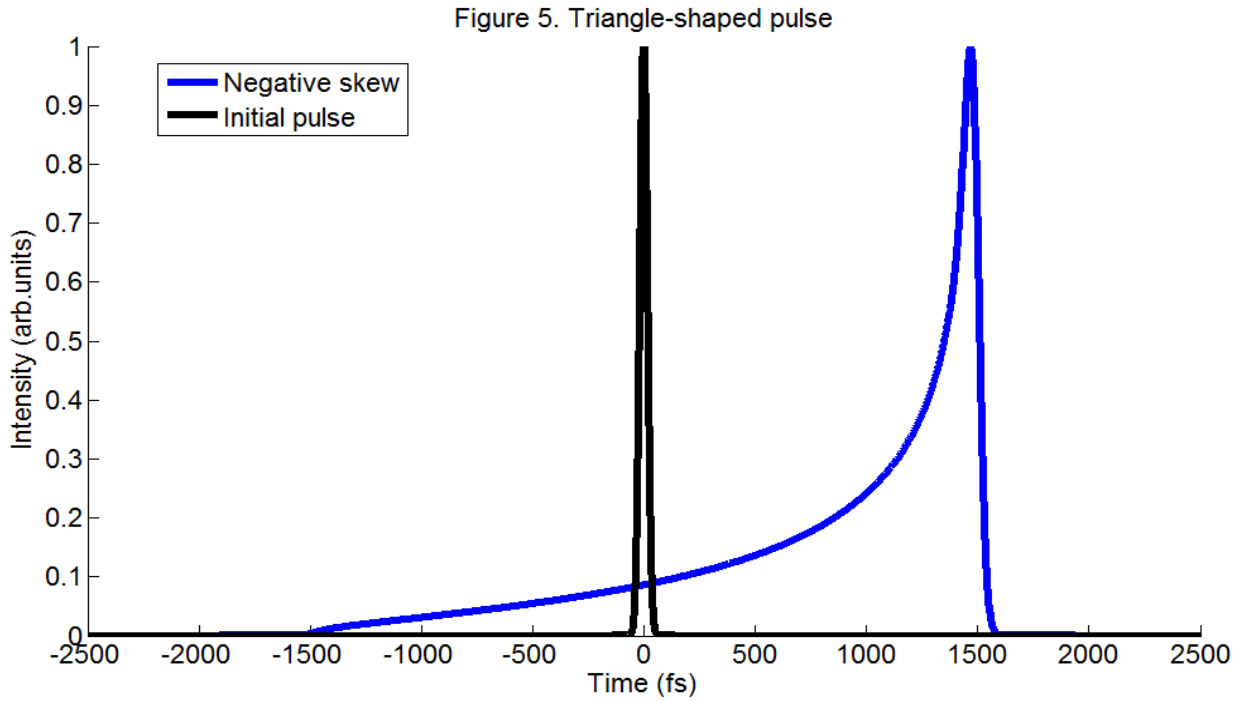

Figure 57. Negatively skewed pulse profile in time domain (blue). Initial pulse (black) is shown for reference.

The algorithm of square-shaped pulse generation works for the non-Gaussian spectral shapes as well. As a proof of concept the spectrum shown in Figure 58 has a dip in the middle. The stretched pulse duration, *T*, is 3,000 fs.

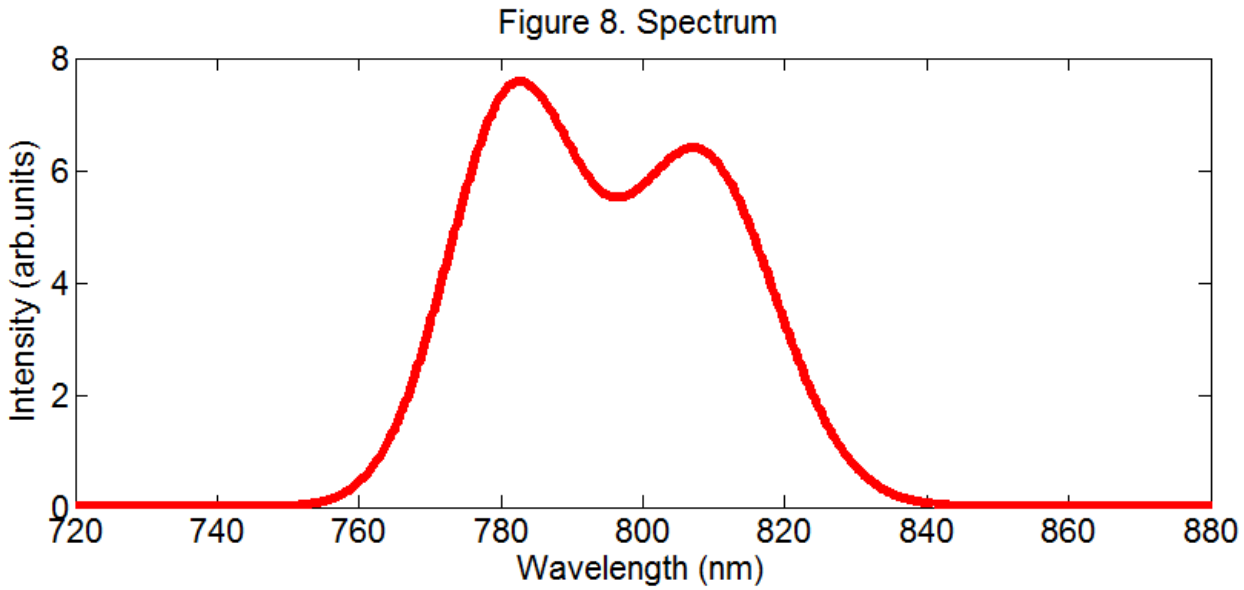

Figure 58. Non-Gaussian shape spectrum of a pulse.

The Matlab code is shown below.

```
clc;
clear all;

ii=(-1)^(0.5); %imaginary unit
lamda0=800; % central wavelength [nm]
pi=3.14159; % constant
c=300; % speed of light [nm/fs]
taup=40; % initial pulse duation in FWHM [fs]
tau0=taup*(2*(log(2))^0.5)^(-1); %Gaussian convolution factor, see G. Agrawal Nonlinear fiber optics
2nd edition
n=4096; %number of points

%Defining the temporal range
np=100; % factor for time axis range
tmax=taup*np; % time axis range
tmin=-tmax;
dt=(tmax-tmin)/(n-1); % time step
t=tmin+dt*(0:n-1); % time range

GaussT=exp(-((t.^2)/(2*tau0^2))); % Gaussian pulse envelop
Intt=GaussT.^2; % Gaussian intensity profile
%_____
```

```
omega0=2*pi*c/lamda0; % the central frequency [rad]
w=2*pi*(-n/2:1:n/2-1)/(dt*n);% frequency range centered at zero
w=omega0+w; % frequency range centered at omega0
Spec=fftshift(fft(GaussT)); % Fourier transform to obtain spectrum

lamda=2*pi*c./w;% wavelength range
Intw=(abs(Spec).^2)/max(abs(Spec).^2);% normalized spectrum

Intw=fliplr(Intw);% spectral array is flipped to match frequency range
shift=100;
Intw=(abs(Spec).^2)/max(abs(Spec).^2); %normalized spectrum
%--------Generate spectrum with a dip-----------------------
Intw_l=Intw(1:shift);
Intw_rightShift=1.2.*cat(2,Intw(shift+1:end),Intw_l);
Intw2=Intw_rightShift+Intw;
Intw2=Intw2/max(Intw2);
shift=30;
Intw2_r=Intw2(length(Intw2)-shift+1:end);
Intw2=cat(2,Intw2_r,Intw2(1:length(Intw2)-shift));
%------------------------------------------------------------
coeff=3000; % desired pulse duration for square pulse [fs]
Intw2=Intw2./trapz(w,Intw2); % normalization
Intw2=fliplr(Intw2);
MAXind2=find(Intw2 == max(Intw2(:)));% find index of the maximal value in spectrum
MAXind2=MAXind2-40;

Int12=cumtrapz(w,coeff*Intw2); % first integral
Int12=Int12-Int12(MAXind2);% DC component subtracted

Int22=cumtrapz(w,Int12); % second integral
Int22=Int22-Int22(MAXind2);% DC component subtracted

PhaseOmega2=Int22;

Eomega2=(Intw2.^0.5).*exp(ii*PhaseOmega2); %  spectral field with a phase

Et2=fftshift(fft(Eomega2)); % Fourier transform to time domain
Intensity2=((abs(Et2)).^2)/(max(((abs(Et2)).^2)));% Intensity profile

figure (8)
subplot(1,2,1);
set(gca,'FontSize',16)
set(gcf, 'Color', [1,1,1]);
plot(lamda,Intw2,'r','LineWidth',5);
set(gca,'FontSize',16);
xlim([720,880]); % wavelength range for Ti:Sapphire laser
title('Figure 8. Spectrum ','FontSize',16);
xlabel('Wavelength (nm)','FontSize',16);
ylabel('Intensity (arb.units)','FontSize',16);
subplot(1,2,2);
set(gca,'FontSize',16)
```

```
set(gcf, 'Color', [1,1,1]);
plot(t,Intensity2,'b','LineWidth',5)
title('Figure 8. Square-shaped pulse','FontSize',16);
xlabel('Time (fs)','FontSize',16);
ylabel('Intensity (arb.units)','FontSize',16);
xlim([-2500 2500]);
```

The result is shown in Figure 59.

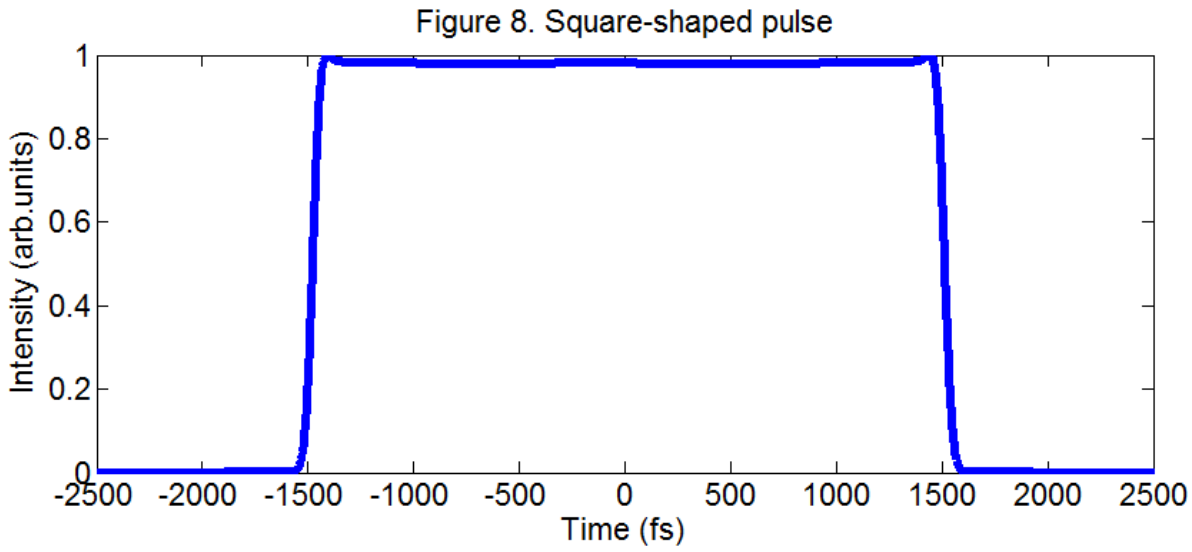

Figure 59. Stretched pulse profile for the spectrum shown in Figure 58.

Appendix B: Sample preparation and substrates

Sulfur (octasulfur, S_8). To control the particle size we used 100 μm and 50 μm size sieves, and selected the particles that were between 50-100 μm. The resulting particles were deposited on a substrate by fingerprinting, by sprinkling on a surface or pressing down onto a surface. Pictures of the substrates are presented in Figure 60.

Potassium perchlorate ($KClO_4$). Stock solid salt was crushed to small crystals, with sizes ranging from 100 μm to 500 μm. The resulting crystals were pressed down onto a substrate.

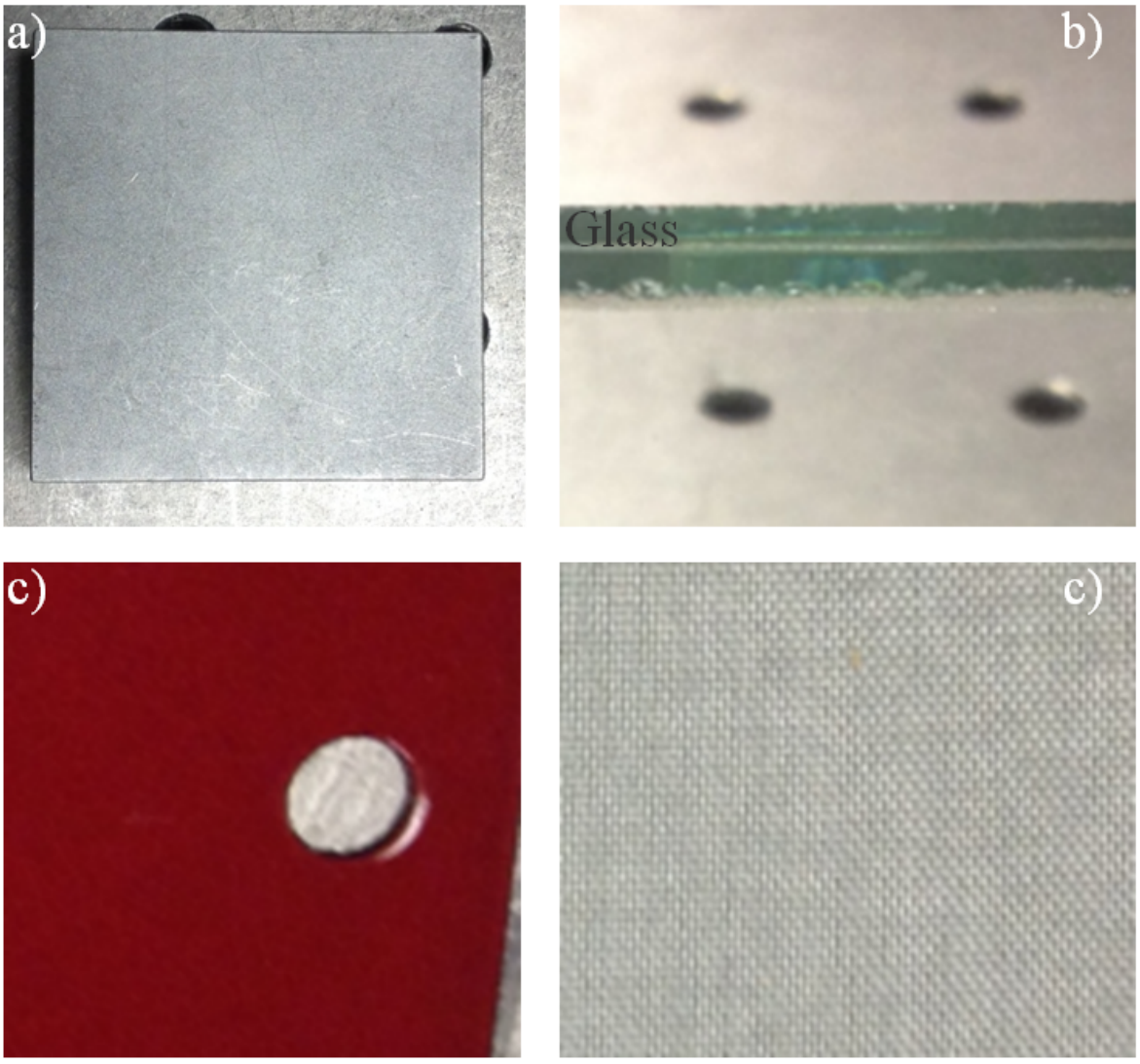

Figure 60. Substrates used in this work: a) Aluminum block. b) Car windshield (laminated glass) with protective polymer interlayer, total thickness 6 mm. c) Car body plate with red metallic paint. d) Nylon fabric.

TATP ($C_9H_{18}O_6$). Triacetone triperoxide impregnated microspheres were gently heated to 150°C for four minutes. The TATP sublimed crystals were sprinkled on a piece of car windshield.

Appendix C: List of publications and conference proceedings

1. G. Rasskazov, A. Ryabtsev, D. Pestov, B. Nie, V.V. Lozovoy, and M. Dantus, "Anomalous laser-induced group velocity dispersion in fused silica," Opt. Express **21**, 17695 (2013).

2. D. Pestov, A. Ryabtsev, G. Rasskazov, V.V. Lozovoy, and M. Dantus, "Real-time single-shot measurement and correction of pulse phase and amplitude for ultrafast lasers," Opt. Eng. **53**, 051511 (2014).

3. G. Rasskazov, A. Ryabtsev, V.V. Lozovoy and M. Dantus, "Laser-induced dispersion control," Opt. Lett. **39,** 3208 (2014).

4. V.V. Lozovoy, G. Rasskazov, D. Pestov, and M. Dantus, "Quantifying noise in ultrafast laser sources and its effect on nonlinear applications," Opt. Express **23**, 12037 (2015).

5. G. Rasskazov, V.V. Lozovoy, and M. Dantus, "Spectral amplitude and phase noise characterization of titanium-sapphire lasers," Opt. Express **23**, 23597 (2015).

6. V.V. Lozovoy, G. Rasskazov, A. Ryabtsev, and M. Dantus, "Phase-only synthesis of ultrafast stretched square pulses," Opt. Express **23**, 27105 (2015).

7. G. Rasskazov, A. Ryabtsev, V.V. Lozovoy, and M. Dantus, "Mitigating self-action processes with chirp or binary phase shaping," Opt. Lett. **41**, 131 (2016).

8. G. Rasskazov, A. Ryabtsev, K. Charan, T. Wang, C. Xu, and M. Dantus, "Characterization and adaptive compression of a multi-soliton laser source," Opt. Express **25**, 320 (2017).

9. G. Rasskazov, A. Ryabtsev, and M. Dantus, "Eye-safe near-infrared trace explosives detection and imaging," Opt. Express **25,** 5832 (2017).

10. G. Rasskazov, M. Nairat, I. Magoulas, V. V. Lozovoy, P. Piecuch, and M. Dantus, "Femtosecond real-time probing of reactions MMXVII: The predissociation of sodium iodide in the A 0^+ state," Chem. Phys. Lett. (in print) (2017).

11. D. Pestov, G. Rasskazov, A. Ryabtsev, I. Pastirk, M. Dantus, "Shaper-based approach to real-time correction of ultrashort pulse phase drifts and transient pulse dispersion measurements", *XVIIIth International Conference on Ultrafast Phenomena, EPJ Web of Conferences* **41**, 11007 (2013).

12. G. Rasskazov, A. Ryabtsev, V. V. Lozovoy, M. Dantus, "Laser-induced dispersion control", *Conference on Lasers and Electro-Optics Europe - Technical Digest*, 6989393 (2014).

13. G. Rasskazov, V. V. Lozovoy, M. Dantus, "Deviations from theory by femtosecond lasers due to noise", *Conference on Lasers and Electro-Optics: Applications and Technology*, JW2A. **77** (2015).

14. G. Rasskazov, A. Ryabtsev, K. Charan, T. Wang, C. Xu, and M. Dantus, "Multi-soliton pulse characterization and compression," *International Conference on Ultrafast Phenomena, OSA Technical Digest*, paper UTh4A.27 (2016).

BIBLIOGRAPHY

BIBLIOGRAPHY

1. T. H. Maiman, "Stimulated optical radiation in ruby," Nature **187**, 493-494 (1960).

2. G. N. Lewis, "The atom and the molecule," JACS **38**, 762-785 (1916).

3. A. H. Zewail, "Femtochemistry. Past, present, and future," Pure Appl. Chem. **72**, 2219-2231 (2000).

4. "Fundamental physical constants," retrieved http://physics.nist.gov/cgi-bin/cuu/Value?plkt.

5. R. G. W. Norrish and G. Porter, "Chemical reactions produced by very high light intensities," Nature **164**, 658-658 (1949).

6. M. Dantus, M. J. Rosker, and A. H. Zewail, "Real-time femtosecond probing of transition-states in chemical-reactions," J. Phys. Chem. **87**, 2395-2397 (1987).

7. P. Cong, G. Roberts, J. L. Herek, A. Mohktari, and A. H. Zewail, "Femtosecond Real-Time Probing of Reactions. 18. Experimental and Theoretical Mapping of Trajectories and Potentials in the NaI Dissociation Reaction," J. Phys. Chem. **100**, 7832–7848 (1996).

8. M. Gruebele and A. H. Zewail, "Ultrafast reaction dynamics," Phys. Today **43**, 24-33 (1990).

9. T. Brabec and F. Krausz, "Intense few-cycle laser fields: frontiers of nonlinear optics," Rev. Mod. Phys. **72**, 545-591 (2000).

10. M. Hentschel, R. Kienberger, C. Spielmann, G. A. Reider, N. Milosevic, T. Brabec, P. Corkum, U. Heinzmann, M. Drescher, and F. Krausz, "Attosecond metrology," Nature **414**, 509-513 (2001).

11. F. Krausz and M. Ivanov, "Attosecond physics," Rev. Mod. Phys. **81**, 163-234 (2009).

12. B. Xu, Y. Coello, V. V. Lozovoy, D. Ahmasi Harris, and M. Dantus, "Pulse shaping of octave spanning femtosecond laser pulses," Opt. Express **14**, 10939-10944 (2006).

13. B. Schrader, "*Infrared and Raman Spectroscopy*," (VCH Weinheim, 1995).

14. J. P. Ogilvie, D. Débarre, X. Solinas, J.-L. Martin, E. Beaurepaire, and M. Joffre, "Use of coherent control for selective two-photon fluorescence microscopy in live organisms," Opt. Express **14**, 759-766 (2006).

15. P. D. Maker and R. W. Terhune, "Study of optical effects due to an induced polarization third order in the electric field strength," Phys. Rev. **137**, A801-A818 (1965).

16. I. Saytashev, B. Xu, M. T. Bremer, and M. Dantus, "Simultaneous selective two-photon microscopy using MHz rate pulse shaping and quadrature detection of the time-multiplexed signal," in *Ultrafast Phenomena XIX: Proceedings of the 19th International Conference, Okinawa Convention Center, Okinawa, Japan, July 7-11, 2014*, K. Yamanouchi, S. Cundiff, R. de Vivie-Riedle, M. Kuwata-Gonokami, and L. DiMauro, eds. (Springer International Publishing, Cham, 2015), pp. 817-820.

17. P. H. Bucksbaum, "The future of attosecond spectroscopy," Science **317**, 766 (2007).

18. A. D. Bandrauk and M. L. Sink, "Photodissociation in intense laser fields: predissociation analogy," J. Chem. Phys. **74**, 1110-1117 (1981).

19. B. M. Garraway and K. A. Suominen, "Adiabatic passage by light-induced potentials in molecules," Phys. Rev. Lett. **80**, 932-935 (1998).

20. M. DiDomenico, "Small-signal analysis of internal (coupling-type) modulation of lasers," J. Appl. Phys. **35**, 2870-2876 (1964).

21. B. E. Lemoff and C. P. J. Barty, "Cubic-phase-free dispersion compensation in solid-state ultrashort-pulse lasers," Opt. Lett. **18**, 57-59 (1993).

22. L. Chinlon, "Studies of relaxation oscillations in organic dye lasers," IEEE J. Quantum Electron. **11**, 602-609 (1975).

23. J. Giordmaine, M. Duguay, and J. Hansen, "Compression of optical pulses," IEEE J. Quantum Electron. **4**, 252-255 (1968).

24. J. D. Kafka, M. L. Watts, D. J. Roach, M. S. Keirstead, H. W. Schaaf, and T. Baer, "Pulse compression of a mode-locked Ti:Sapphire laser," in *Ultrafast Phenomena VII: Proceedings of the 7th International Conference, Monterey, CA, May 14–17, 1990*, C. B. Harris, E. P. Ippen, G. A. Mourou, and A. H. Zewail, eds. (Springer Berlin Heidelberg, Berlin, Heidelberg, 1990), pp. 66-68.

25. D. E. Spence, P. N. Kean, and W. Sibbett, "60-fsec pulse generation from a self-mode-locked Ti:sapphire laser," Opt. Lett. **16**, 42-44 (1991).

26. U. Keller, W. H. Knox, and H. Roskos, "Coupled-cavity resonant passive modelocked (RPM) Ti:Sapphire laser," in *Ultrafast Phenomena VII: Proceedings of the 7th International Conference, Monterey, CA, May 14–17, 1990*, C. B. Harris, E. P. Ippen, G. A. Mourou, and A. H. Zewail, eds. (Springer Berlin Heidelberg, Berlin, Heidelberg, 1990), pp. 69-71.

27. A. Sommerfeld, "*Wave propagation and Group Velocity*," (Academic Press: San Diego, 1960), Chap. 2.

28. R. L. Fork, O. E. Martinez, and J. P. Gordon, "Negative dispersion using pairs of prisms," Opt. Lett. **9**, 150-152 (1984).

29. R. L. Fork, C. H. Brito Cruz, P. C. Becker, and C. V. Shank, "Compression of optical pulses to six femtoseconds by using cubic phase compensation," Opt. Lett. **12**, 483-485 (1987).

30. B. Proctor and F. Wise, "Quartz prism sequence for reduction of cubic phase in a mode-lockedTi:Al_2O_3 laser," Opt. Lett. **17**, 1295-1297 (1992).

31. E. Treacy, "Optical pulse compression with diffraction gratings," IEEE J. Quantum Electron. **5**, 454-458 (1969).

32. D. Strickland and G. Mourou, "Compression of amplified chirped optical pulses," Opt. Commun. **56**, 219-221 (1985).

33. C. Froehly, B. Colombeau, and M. Vampouille, "II Shaping and analysis of picosecond light pulses," in *Progress in Optics*, (1983), pp. 63-153.

34. A. M. Weiner and J. P. Heritage, "Picosecond and femtosecond Fourier pulse shape synthesis," Rev. Phys. Appl. (Paris) **22**, 1619-1628 (1987).

35. D. Grischkowsky and A. C. Balant, "Optical pulse compression based on enhanced frequency chirping," Appl. Phys. Lett. **41**, 1-3 (1982).

36. A. M. Weiner, D. E. Leaird, J. S. Patel, and J. R. Wullert, "Programmable femtosecond pulse shaping by use of a multielement liquid-crystal phase modulator," Opt. Lett. **15**, 326-328 (1990).

37. A. M. Weiner, D. E. Leaird, J. S. Patel, and J. R. Wullert, "Programmable shaping of femtosecond optical pulses by use of 128-element liquid crystal phase modulator," IEEE J. Quantum Electron. **28**, 908-920 (1992).

38. M. M. Wefers and K. A. Nelson, "Programmable phase and amplitude femtosecond pulse shaping," Opt. Lett. **18**, 2032-2034 (1993).

39. D. Yelin, D. Meshulach, and Y. Silberberg, "Adaptive femtosecond pulse compression," Opt. Lett. **22**, 1793-1795 (1997).

40. K. A. Walowicz, I. Pastirk, V. V. Lozovoy, and M. Dantus, "Multiphoton intrapulse interference. 1. Control of multiphoton processes in condensed phases," J. Phys. Chem. A **106**, 9369-9373 (2002).

41. J. X. Tull, M. A. Dugan, and W. S. Warren, "High-resolution, ultrafast laser pulse shaping and its applications," in *Advances in magnetic and optical resonance*, S. W. Warren, ed. (Academic Press, 1997), pp. 1-II.

42. E. Zeek, K. Maginnis, S. Backus, U. Russek, M. Murnane, G. Mourou, H. Kapteyn, and G. Vdovin, "Pulse compression by use of deformable mirrors," Opt. Lett. **24**, 493-495 (1999).

43. J. L. Krause, R. M. Whitnell, K. R. Wilson, Y. Yan, and S. Mukamel, "Optical control of molecular dynamics: molecular cannons, reflectrons, and wave-packet focusers," J. Chem. Phys. **99**, 6562-6578 (1993).

44. W. S. Warren, "Chemistry with photons," Science **262**, 1008 (1993).

45. V. V. Lozovoy and M. Dantus, "Systematic control of nonlinear optical processes using optimally shaped femtosecond pulses," Chem. Phys. Chem. **6**, 1970-2000 (2005).

46. R. Trebino, "*Frequency-Resolved Optical Gating*," (Springer, 2002).

47. J.-K. Rhee, J. A. Arns, W. S. Colburn, T. S. Sosnowski, and T. B. Norris, "Chirped-pulse amplification of 85-fs pulses at 250 kHz with third-order dispersion compensation by use of holographic transmission gratings," Opt. Lett. **19**, 1550-1552 (1994).

48. C. Iaconis and I. A. Walmsley, "Spectral phase interferometry for direct electric-field reconstruction of ultrashort optical pulses," Opt. Lett. **23**, 792-794 (1998).

49. D. Meshulach, D. Yelin, and Y. Silberberg, "Adaptive real-time femtosecond pulse shaping," JOSA B **15**, 1615-1619 (1998).

50. V. V. Lozovoy, I. Pastirk, and M. Dantus, "Multiphoton intrapulse interference. IV. Ultrashort laser pulse spectral phase characterization and compensation," Opt. Lett. **29**, 775-777 (2004).

51. B. von Vacano, T. Buckup, and M. Motzkus, "In situ broadband pulse compression for multiphoton microscopy using a shaper-assisted collinear SPIDER," Opt. Lett. **31**, 1154-1156 (2006).

52. A. Galler and T. Feurer, "Pulse shaper assisted short laser pulse characterization," Appl. Phys. B **90**, 427-430 (2008).

53. A. M. Weiner, J. P. Heritage, and J. A. Salehi, "Encoding and decoding of femtosecond pulses," Opt. Lett. **13**, 300-302 (1988).

54. M. Saruwatari, "Progress toward ultrahigh-bit-rate all-optical TDM transmission systems," in *Proceedings of IEE/LEOS Summer Topical Meetings: Integrated Optoelectronics*, 1994), 45-46.

55. M. Nairat, V. V. Lozovoy, and M. Dantus, "Order of magnitude dissociative ionization enhancement observed for pulses with high order dispersion," J. Phys. Chem. A **120**, 8529-8536 (2016).

56. B. Xu, J. M. Gunn, J. M. D. Cruz, V. V. Lozovoy, and M. Dantus, "Quantitative investigation of the multiphoton intrapulse interference phase scan method for simultaneous phase measurement and compensation of femtosecond laser pulses," JOSA B **23**, 750-759 (2006).

57. Y. Coello, B. Xu, T. L. Miller, V. V. Lozovoy, and M. Dantus, "Group-velocity dispersion measurements of water, seawater, and ocular components using multiphoton intrapulse interference phase scan," Appl. Opt. **46**, 8394-8401 (2007).

58. Y. Coello, V. V. Lozovoy, T. C. Gunaratne, B. Xu, I. Borukhovich, C.-h. Tseng, T. Weinacht, and M. Dantus, "Interference without an interferometer: a different approach to measuring, compressing, and shaping ultrashort laser pulses," JOSA B **25**, A140-A150 (2008).

59. D. Pestov, V. V. Lozovoy, and M. Dantus, "Single-beam shaper-based pulse characterization and compression using MIIPS sonogram," Opt. Lett. **35**, 1422-1424 (2010).

60. R. W. Boyd, "*Nonlinear optics*," (Academic Press, 1992).

61. Y. R. Shen, "*The principles of nonlinear optics*," (John Wiley & Sons, 1984).

62. R. R. Gattass and E. Mazur, "Femtosecond laser micromachining in transparent materials," Nat. Photon. **2**, 219-225 (2008).

63. M. Ams, G. D. Marshall, P. Dekker, M. Dubov, V. K. Mezentsev, I. Bennion, and M. J. Withford, "Investigation of ultrafast laser-photonic material interactions: challenges for directly written glass photonics," IEEE J. Sel. Topics Quantum Electron. **14**, 1370-1381 (2008).

64. B. S. Chris, B. André, and M. Eric, "Laser-induced breakdown and damage in bulk transparent materials induced by tightly focused femtosecond laser pulses," Meas. Sci. Technol. **12**, 1784 (2001).

65. B. C. Stuart, M. D. Feit, S. Herman, A. M. Rubenchik, B. W. Shore, and M. D. Perry, "Nanosecond-to-femtosecond laser-induced breakdown in dielectrics," Phys. Rev. B **53**, 1749-1761 (1996).

66. R. Hellwarth, J. Cherlow, and T.-T. Yang, "Origin and frequency dependence of nonlinear optical susceptibilities of glasses," Phys. Rev. B **11**, 964-967 (1975).

67. S. A. Akhmanov, V. A. Vysloukh, and A. S. Chirkin, "*Optics of femtosecond laser pulses*," (American Institute of Physics, 1992).

68. E. L. Buckland and R. W. Boyd, "Electrostrictive contribution to the intensity-dependent refractive index of optical fibers," Opt. Lett. **21**, 1117-1119 (1996).

69. R. R. Alfano and S. L. Shapiro, "Observation of self-phase modulation and small-scale filaments in crystals and glasses," Phys. Rev. Lett. **24**, 592-594 (1970).

70. F. Shimizu, "Frequency broadening in liquids by a short light pulse," Phys. Rev. Lett. **19**, 1097-1100 (1967).

71. S. Tzortzakis, L. Sudrie, M. Franco, B. Prade, A. Mysyrowicz, A. Couairon, and L. Bergé, "Self-guided propagation of ultrashort IR laser pulses in fused silica," Phys. Rev. Lett. **87**, 213902 (2001).

72. P. L. Kelley, "Self-focusing of optical beams," Phys. Rev. Lett. **15**, 1005-1008 (1965).

73. R. L. Fork, W. J. Tomlinson, C. V. Shank, C. Hirlimann, and R. Yen, "Femtosecond white-light continuum pulses," Opt. Lett. **8**, 1-3 (1983).

74. R. R. Alfano and S. L. Shapiro, "Emission in the region 4000 to 7000 Å via four-photon coupling in glass," Phys. Rev. Lett. **24**, 584-587 (1970).

75. R. Y. Chiao, E. Garmire, and C. H. Townes, "Self-trapping of optical beams," Phys. Rev. Lett. **13**, 479-482 (1964).

76. N. G. Bondarenko, I. V. Eremina, and V. I. Talanov, "Broadening of spectrum in self-focusing of light in crystals," JETP Lett. **12**, 85-87 (1970).

77. B. Min, T. J. Kippenberg, and K. J. Vahala, "Compact, fiber-compatible, cascaded Raman laser," Opt. Lett. **28**, 1507-1509 (2003).

78. R. Stolen, "Phase-matched-stimulated four-photon mixing in silica-fiber waveguides," IEEE J. Quantum Electron. **11**, 100-103 (1975).

79. R. L. Carman, R. Y. Chiao, and P. L. Kelley, "Observation of degenerate stimulated four-photon interaction and four-wave parametric amplification," Phys. Rev. Lett. **17**, 1281-1283 (1966).

80. P. Baldeck and R. Alfano, "Intensity effects on the stimulated four photon spectra generated by picosecond pulses in optical fibers," J. Lightwave Technol. **5**, 1712-1715 (1987).

81. C. Lin and R. H. Stolen, "New nanosecond continuum for excited-state spectroscopy," Appl. Phys. Lett. **28**, 216-218 (1976).

82. M. Nisoli, S. De Silvestri, O. Svelto, "Generation of high-energy 10-fs pulses by a new pulse compression technique," Appl. Phys. Lett. **68**, 2793-2795 (1996).

.83. J. H. Kim, M.-K. Chen, C.-E. Yang, J. Lee, K. Shi, Z. Liu, S. Yin, K. Reichard, P. Ruffin, E. Edwards, C. Brantley, and C. Luo, "Broadband supercontinuum generation covering UV to mid-

IR region by using three pumping sources in single crystal sapphire fiber," Opt. Express **16**, 14792-14800 (2008).

84. N. G. R. Broderick, H. L. Offerhaus, D. J. Richardson, R. A. Sammut, J. Caplen, and L. Dong, "Large mode area fibers for high power applications," Opt. Fiber Technol. **5**, 185-196 (1999).

85. X. Liu, C. Xu, W. H. Knox, J. K. Chandalia, B. J. Eggleton, S. G. Kosinski, and R. S. Windeler, "Soliton self-frequency shift in a short tapered air–silica microstructure fiber," Opt. Lett. **26**, 358-360 (2001).

86. J. K. Ranka, R. S. Windeler, and A. J. Stentz, "Visible continuum generation in air–silica microstructure optical fibers with anomalous dispersion at 800 nm," Opt. Lett. **25**, 25-27 (2000).

87. J. Broeng, D. Mogilevstev, S. E. Barkou, and A. Bjarklev, "Photonic crystal fibers: a new class of optical waveguides," Opt. Fiber Technol. **5**, 305-330 (1999).

88. J. C. Knight, T. A. Birks, P. S. J. Russell, and D. M. Atkin, "All-silica single-mode optical fiber with photonic crystal cladding," Opt. Lett. **21**, 1547-1549 (1996).

89. P. Kaiser and H. W. Astle, "Low-loss single-material fibers made from pure fused silica," Bell Syst. Tech. J. **53**, 1021-1039 (1974).

90. G. P. Agrawal, "*Nonlinear Fiber Optics*," (Academic Press, 2001).

91. A. M. Heidt, "Pulse preserving flat-top supercontinuum generation in all-normal dispersion photonic crystal fibers," JOSA B **27**, 550-559 (2010).

92. L. F. Mollenauer, R. H. Stolen, and J. P. Gordon, "Experimental observation of picosecond pulse narrowing and solitons in optical fibers," Phys. Rev. Lett. **45**, 1095-1098 (1980).

93. A. Hasegawa and F. Tappert, "Transmission of stationary nonlinear optical pulses in dispersive dielectric fibers. I. Anomalous dispersion," Appl. Phys. Lett. **23**, 142-144 (1973).

94. M. Chemnitz, J. Wei, C. Jain, B. P. Rodrigues, T. Wieduwilt, J. Kobelke, L. Wondraczek, and M. A. Schmidt, "Octave-spanning supercontinuum generation in hybrid silver metaphosphate/silica step-index fibers," Opt. Lett. **41**, 3519-3522 (2016).

95. J. M. Dudley, G. Genty, and S. Coen, "Supercontinuum generation in photonic crystal fiber," Rev. Mod. Phys. **78**, 1135-1184 (2006).

96. J. M. Dudley and S. Coen, "Coherence properties of supercontinuum spectra generated in photonic crystal and tapered optical fibers," Opt. Lett. **27**, 1180-1182 (2002).

97. P. M. Pellegrino, E. L. Holthoff, and M. E. Farrell, "*Laser-based optical detection of explosives*," (CRC Press Taylor & Francis Group, 2015).

98. C. Krafft, B. Dietzek, M. Schmitt, and J. Popp, "Raman and coherent anti-Stokes Raman scattering microspectroscopy for biomedical applications," J. Biomed. Opt **17**, 0408011-04080115 (2012).

99. J. Rothhardt, S. Hädrich, T. Gottschall, J. Limpert, A. Tünnermann, M. Rothhardt, M. Becker, S. Brückner, and H. Bartelt, "Generation of flattop pump pulses for OPCPA by coherent pulse stacking with fiber Bragg gratings," Opt. Express **17**, 16332-16341 (2009).

100. V. V. Lozovoy, G. Rasskazov, D. Pestov, and M. Dantus, "Quantifying noise in ultrafast laser sources and its effect on nonlinear applications," Opt. Express **23**, 12037-12044 (2015).

101. I. V. Yakovlev, "Stretchers and compressors for ultra-high power laser systems," Quantum Electron. **44**, 393-414 (2014).

102. A. Vaupel, N. Bodnar, B. Webb, L. Shah, and M. Richardson, "Concepts, performance review, and prospects of table-top, few-cycle optical parametric chirped-pulse amplification," Opt. Eng. **53** 051507 (2014).

103. A. Dubietis, G. Jonušauskas, and A. Piskarskas, "Powerful femtosecond pulse generation by chirped and stretched pulse parametric amplification in BBO crystal," Opt. Commun. **88**, 437-440 (1992).

104. O. E. Martinez, "Design of high-power ultrashort pulse amplifiers by expansion and recompression," IEEE J. Quantum Electron. **23**, 1385-1387 (1987).

105. E. B. Treacy, "Optical pulse compression with diffraction gratings," IEEE J. Quantum Electron. **QE-5**, 454-458 (1969).

106. A. M. Weiner, J. P. Heritage, and R. N. Thurston, "Synthesis of phase-coherent, picosecond optical square pulses," Opt. Lett. **11** (1986).

107. M. M. Wefers and K. A. Nelson, "Analysis of programmable ultrashort waveform generation using liquid-crystal spatial light modulators," J. Opt. Soc. Am. B **12**, 1343-1362 (1995).

108. A. Rundquist, A. Efimov, and D. H. Reitze, "Pulse shaping with the Gerchberg-Saxton algorithm," JOSA B: Opt. Phys. **19**, 2468-2478 (2002).

109. T. Oksenhendler and N. Forget, "Pulse shaping techniques theory and experimental implementation for femtosecond pulses," Adv. Solid State Lasers: Dev. Appl., 630 (2010).

110. I. Will and G. Klemz, "Generation of flat-top picosecond pulses by coherent pulse stacking in a multicrystal birefringent filter," Opt. Express **16**, 14922-14937 (2008).

111. V. V. Lozovoy, B. Xu, Y. Coello, and M. Dantus, "Direct measurement of spectral phase for ultrashort laser pulses," Opt. Express **16**, 592-597 (2008).

112. Y. Coello, V. V. Lozovoy, T. C. Gunaratne, B. Xu, I. Borukhovich, C. H. Tseng, T. Weinacht, and M. Dantus, "Interference without an interferometer: a different approach to measuring, compressing, and shaping ultrashort laser pulses," JOSA B: Opt. Phys. **25**, A140-A150 (2008).

113. B. Xu, J. M. Gunn, J. M. Dela Cruz, V. V. Lozovoy, and M. Dantus, "Quantitative investigation of the multiphoton intrapulse interference phase scan method for simultaneous phase measurement and compensation of femtosecond laser pulses," JOSA B: Opt. Phys. **23**, 750-759 (2006).

114. F. Fu, R. Wang, P. Zhu, L. Zhao, T. Jiang, C. Lu, S. Liu, L. Shi, L. Yan, H. Deng, C. Feng, Q. Gu, D. Huang, B. Liu, D. Wang, X. Wang, M. Zhang, Z. Zhao, G. Stupakov, D. Xiang, and J. Zhang, "Demonstration of nonlinear-energy-spread compensation in relativistic electron bunches with corrugated structures," Phys. Rev. Lett. **114** (2015).

115. P. H. Williams, G. Hirst, B. D. Muratori, H. L. Owen, and S. L. Smith, "Electron beam dynamics in 4GLS," in *Proceedings of the IEEE Particle Accelerator Conference*, 2007), 1103-1105.

116. F. V. Hartemann, W. J. Brown, D. J. Gibson, S. G. Anderson, A. M. Tremaine, P. T. Springer, A. J. Wootton, E. P. Hartouni, and C. P. J. Barty, "High-energy scaling of Compton scattering light sources," Phys. Rev. ST Accel. Beams **8**, 1-28 (2005).

117. A. Paul, E. A. Gibson, X. Zhang, A. Lytle, T. Popmintchev, X. Zhou, M. M. Murnane, I. P. Christov, and H. C. Kapteyn, "Phase-matching techniques for coherent soft X-ray generation," IEEE J. Quantum Electron. **42**, 14-26 (2006).

118. P. K. Upputuri, L. Gong, and H. Wang, "Chirped time-resolved CARS microscopy with square-pulse excitation," Opt. Express **22**, 9611-9626 (2014).

119. E. B. Treacy, "Measurement of picosecond pulse substructure using compression techniques," Appl. Phys. Lett. **14**, 112-114 (1969).

120. P. Xi, Y. Andegeko, L. R. Weisel, V. V. Lozovoy, and M. Dantus, "Greater signal, increased depth, and less photobleaching in two-photon microscopy with 10 fs pulses," Opt. Commun. **281**, 1841-1849 (2008).

121. W. Denk, J. H. Strickler, and W. W. Webb, "Two-photon laser scanning fluorescence microscopy," Science **248**, 73-76 (1990).

122. R. C. Greenhow and A. J. Schmidt, "Picosecond light pulses," in *Advances in Quantum Electronics: Volume 2*, D. W. Goodwin eds (Academic Press, 2013) **2**, 158-286 (1974).

123. R. Trebino, Frequency-resolved optical gating: the measurement of ultrashort laser pulses (2002).

124. M. Rhodes, G. Steinmeyer, J. Ratner, and R. Trebino, "Pulse-shape instabilities and their measurement," Laser Photon. Rev. **7**, 557-565 (2013).

125. Y. Li, L. F. Lester, D. Chang, C. Langrock, M. M. Fejer, and D. J. Kane, "Characteristics and instabilities of mode-locked quantum-dot diode lasers," Opt. Express **21**, 8007-8017 (2013).

126. J. Ratner, G. Steinmeyer, T. C. Wong, R. Bartels, and R. Trebino, "Coherent artifact in modern pulse measurements," Opt. Lett. **37**, 2874-2876 (2012).

127. J. N. Ames, S. Ghosh, R. S. Windeler, A. L. Gaeta, and S. T. Cundiff, "Excess noise generation during spectral broadening in a microstructured fiber," Appl. Phys. B: Lasers Opt. **77**, 279-284 (2003).

128. B. Nie, G. Parker, V. V. Lozovoy, and M. Dantus, "Energy scaling of Yb fiber oscillator producing clusters of femtosecond pulses," Opt. Eng. **53**, 051505 (2014).

129. M. Horowitz, Y. Barad, and Y. Silberberg, "Noiselike pulses with a broadband spectrum generated from an erbium-doped fiber laser," Opt. Lett. **22**, 799-801 (1997).

130. C. M. Miller, "Intensity modulation and noise characterization of high-speed semiconductor lasers," IEEE LTS **2**, 44-50 (1991).

131. D. E. McCumber, "Intensity fluctuations in the output of cw laser oscillators. I," Phys. Rev. **141**, 306-322 (1966).

132. M. C. Cox, N. J. Copner, and B. Williams, "High sensitivity precision relative intensity noise calibration standard using low noise reference laser source," IEE Proc.: Sci. Meas. Technol. **145**, 163-165 (1998).

133. S. A. Diddams, M. Kirchner, T. Fortier, D. Braje, A. M. Weiner, and L. Hollberg, "Improved signal-to-noise ratio of 10 GHz microwave signals generated with a mode-filtered femtosecond laser frequency comb," Opt. Express **17**, 3331-3340 (2009).

134. R. W. Schoonover, B. J. Davis, R. A. Bartels, and P. S. Carney, "Optical interferometry with pulsed fields," J. Mod. Opt. **55**, 1541-1556 (2008).

135. A. F. J. Runge, C. Aguergaray, N. G. R. Broderick, and M. Erkintalo, "Coherence and shot-to-shot spectral fluctuations in noise-like ultrafast fiber lasers," Opt. Lett. **38**, 4327-4330 (2013).

136. D. von der Linde, "Characterization of the noise in continuously operating mode-locked lasers," Appl. Phys. B **39**, 201-217 (1986).

137. W. A. Gardner, A. Napolitano, and L. Paura, "Cyclostationarity: half a century of research," Signal Process. **86**, 639-697 (2006).

138. B. J. Davis, "Observable coherence theory for statistically periodic fields," Phys. Rev. A **76**, 043843 (2007).

139. V. Torres-Company, H. Lajunen, and A. T. Friberg, "Coherence theory of noise in ultrashort-pulse trains," JOSA B **24**, 1441-1450 (2007).

140. B. Lacaze and M. Chabert, "Theoretical spectrum of noisy optical pulse trains," Appl. Opt. **47**, 3231-3240 (2008).

141. T. Pfeifer, Y. Jiang, S. Dusterer, R. Moshammer, and J. Ullrich, "Partial-coherence method to model experimental free-electron laser pulse statistics," Opt. Lett. **35**, 3441-3443 (2010).

142. M. Miranda, C. L. Arnold, T. Fordell, F. Silva, B. Alonso, R. Weigand, A. L'Huillier, and H. Crespo, "Characterization of broadband few-cycle laser pulses with the d-scan technique," Opt. Express **20**, 18732-18743 (2012).

143. V. Loriot, G. Gitzinger, and N. Forget, "Self-referenced characterization of femtosecond laser pulses by chirp scan," Opt. Express **21**, 24879-24893 (2013).

144. R. Gaudiuso, M. Dell'Aglio, O. De Pascale, G. S. Senesi, and A. De Giacomo, "Laser induced breakdown spectroscopy for elemental analysis in environmental, cultural heritage and space applications: a review of methods and results," Sensors (Basel, Switzerland) **10**, 7434-7468 (2010).

145. R. J. Hall and A. C. Eckbreth, "*Coherent Anti-Stokes Raman Spectroscopy (CARS): Application to Combustion Diagnostics*," (Academic, 1984).

146. J. Kasparian, M. Rodriguez, G. Méjean, J. Yu, E. Salmon, H. Wille, R. Bourayou, S. Frey, Y. B. André, A. Mysyrowicz, R. Sauerbrey, J. P. Wolf, and L. Wöste, "White-light filaments for atmospheric analysis," Science **301**, 61 (2003).

147. P. M. Pellegrino, E. L. Holthoff, and M. E. Farrel, "*Laser-based optical detection of explosives*," (CRC Press Taylor & Francis Group, 2015).

148. R. G. Ewing, D. A. Atkinson, G. A. Eiceman, and G. J. Ewing, "A critical review of ion mobility spectrometry for the detection of explosives and explosive related compounds," Talanta **54**, 515-529 (2001).

149. E. S. Forzani, D. Lu, M. J. Leright, A. D. Aguilar, F. Tsow, R. A. Iglesias, Q. Zhang, J. Lu, J. Li, and N. Tao, "A hybrid electrochemical−colorimetric sensing platform for detection of explosives," JACS **131**, 1390-1391 (2009).

150. M. C. Kemp, C. Baker, and I. Gregory, "Stand-off explosives detection using terahertz technology," in *Stand-off detection of suicide bombers and mobile subjects*, H. Schubert and A. Rimski-Korsakov, eds. (Springer Netherlands, Dordrecht, 2006), pp. 151-165.

151. M. C. Kemp, C. Baker, and I. Gregory, "*Stand-off detection of suicide bombers and mobile subjects*," (Springer, 2006), Chap. 18.

152. H. Li, D. A. Harris, B. Xu, P. J. Wrzesinski, V. V. Lozovoy, and M. Dantus, "Coherent mode-selective Raman excitation towards standoff detection," Opt. Express **16**, 5499-5504 (2008).

153. O. Katz, A. Natan, Y. Silberberg, and S. Rosenwaks, "Standoff detection of trace amounts of solids by nonlinear Raman spectroscopy using shaped femtosecond pulses," Appl. Phys. Lett. **92**, 171116 (2008).

154. M. T. Bremer, P. J. Wrzesinski, N. Butcher, V. V. Lozovoy, and M. Dantus, "Highly selective standoff detection and imaging of trace chemicals in a complex background using single-beam coherent anti-Stokes Raman scattering," Appl. Phys. Lett. **99**, 101109 (2011).

155. M. T. Bremer and M. Dantus, "Standoff explosives trace detection and imaging by selective stimulated Raman scattering," Appl. Phys. Lett. **103**, 061119 (2013).

156. R. Glenn and M. Dantus, "Single broadband phase-shaped pulse stimulated Raman spectroscopy for standoff trace explosive detection," JPCL **7**, 117-125 (2016).

157. F. C. DeLucia, A. C. Samuels, R. S. Harmon, R. A. Walters, K. L. McNesby, A. LaPointe, R. J. Winkel, and A. W. Miziolek, "Laser-induced breakdown spectroscopy (LIBS): a promising versatile chemical sensor technology for hazardous material detection," IEEE Sensors J. **5**, 681-689 (2005).

158. M. Gaft and L. Nagli, "UV gated Raman spectroscopy for standoff detection of explosives," Opt. Mater. **30**, 1739-1746 (2008).

159. A. Tripathi, E. D. Emmons, P. G. Wilcox, J. A. Guicheteau, D. K. Emge, S. D. Christesen, and A. W. Fountain, "Semi-automated detection of trace explosives in fingerprints on strongly interfering surfaces with Raman chemical imaging," Appl. Spectrosc. **65**, 611-619 (2011).

160. B. Zachhuber, G. Ramer, A. Hobro, E. t. H. Chrysostom, and B. Lendl, "Stand-off Raman spectroscopy: a powerful technique for qualitative and quantitative analysis of inorganic and organic compounds including explosives," Anal. Bioanal. Chem. **400**, 2439-2447 (2011).

161. M. L. Lewis, I. R. Lewis, and P. R. Griffiths, "Anti-Stokes Raman spectrometry with 1064-nm excitation: an effective instrumental approach for field detection of explosives," Appl. Spectrosc. **58**, 420-427 (2004).

162. R. Furstenberg, C. A. Kendziora, J. Stepnowski, S. V. Stepnowski, M. Rake, M. R. Papantonakis, V. Nguyen, G. K. Hubler, and R. A. McGill, "Stand-off detection of trace explosives via resonant infrared photothermal imaging," Appl. Phys. Lett. **93**, 224103 (2008).

163. C. W. Van Neste, L. R. Senesac, and T. Thundat, "Standoff spectroscopy of surface adsorbed chemicals," Anal. Chem. **81**, 1952-1956 (2009).

164. F. Fuchs, C. Wild, Y. Rahmouni, W. Bronner, B. Raynor, K. Köhler, and J. Wagner, "Remote sensing of explosives using mid-infrared quantum cascade lasers," Proc. SPIE **6739**, 673904-673909 (2007).

165. C. W. V. Neste, L. R. Senesac, D. Yi, and T. Thundat, "Standoff detection of explosive residues using photothermal microcantilevers," Appl. Phys. Lett. **92**, 134102 (2008).

166. C. W. V. Neste, L. R. Senesac, and T. Thundat, "Standoff photoacoustic spectroscopy," Appl. Phys. Lett. **92**, 234102 (2008).

167. C. A. Kendziora, R. Furstenberg, M. Papantonakis, V. Nguyen, J. Byers, and R. Andrew McGill, "Infrared photothermal imaging spectroscopy for detection of trace explosives on surfaces," Appl. Opt. **54**, F129-F138 (2015).

168. American, National, Standards, and Institute, "American national standard for safe use of lasers," ANSI Z 136.1 −2007, Orlando, Laser Institute of America (2007).

169. S. A. Asher and C. R. Johnson, "Raman spectroscopy of a coal liquid shows that fluorescence interference is minimized with ultraviolet excitation," Science **225**, 311 (1984).

170. D. Oron, N. Dudovich, and Y. Silberberg, "Single-pulse phase-contrast nonlinear Raman spectroscopy," Phys. Rev. Lett. **89**, 273001 (2002).

171. H. Lotem, R. T. Lynch, and N. Bloembergen, "Interference between Raman resonances in four-wave difference mixing," Phys. Rev. A **14**, 1748-1755 (1976).

172. J.-X. Cheng and X. S. Xie, "Coherent anti-Stokes Raman scattering microscopy: instrumentation, theory, and applications," J. Phys. Chem. B **108**, 827-840 (2004).

173. J. L. Oudar, R. W. Smith, and Y. R. Shen, "Polarization-sensitive coherent anti-Stokes Raman spectroscopy," Appl. Phys. Lett. **34**, 758-760 (1979).

174. R. P. Lucht, M. A. Maris, and R. E. Palmer, "Simultaneous acquisition of pure rotational and vibrational nitrogen spectra using three-laser coherent anti-Stokes Raman spectroscopy," Opt. Lett. **12**, 386-388 (1987).

175. D. Pestov, G. O. Ariunbold, X. Wang, R. K. Murawski, V. A. Sautenkov, A. V. Sokolov, and M. O. Scully, "Coherent versus incoherent Raman scattering: molecular coherence excitation and measurement," Opt. Lett. **32**, 1725-1727 (2007).

176. F. M. Mitschke and L. F. Mollenauer, "Discovery of the soliton self-frequency shift," Opt. Lett. **11**, 659-661 (1986).

177. K. Wang, N. G. Horton, K. Charan, and C. Xu, "Advanced fiber soliton sources for nonlinear deep tissue imaging in biophotonics," IEEE J. Sel.Topics Quantum Electron. **20**, 50-60 (2014).

178. T. S. Rose, M. J. Rosker, and A. H. Zewail, "Femtosecond real-time observation of wave packet oscillations (resonance) in dissociation reactions," J. Chem. Phys. **88**, 6672-6673 (1988).

179. V. Engel, H. Metiu, R. Almeida, R. A. Marcus, and A. H. Zewail, "Molecular state evolution after excitation with an ultra-short laser pulse: A quantum analysis of NaI and NaBr dissociation," Chem. Phys. Lett. **152**, 1-7 (1988).

180. T. S. Rose, M. J. Rosker, and A. H. Zewail, "Femtosecond real-time probing of reactions. IV. The reactions of alkali halides," J. Chem. Phys. **91**, 7415-7436 (1989).

181. A. Materny, J. L. Herek, P. Cong, and A. H. Zewail, "Femtosecond Real-Time Probing of Reactions. 16. Dissociation with Intense Pulses," J. Phys. Chem. **98**, 3352-3360 (1994).

182. J. L. Herek, A. Materny, and A. H. Zewail, "Femtosecond control of an elementary unimolecular reaction from the transition-state region," Chem. Phys. Lett. **228**, 15-25 (1994).

183. P. Cong, G. Roberts, J. L. Herek, A. Mohktari, and A. H. Zewail, "Femtosecond real-time probing of reactions. 18. Experimental and theoretical mapping of trajectories and potentials in the NaI dissociation reaction," J. Phys. Chem. **100**, 7832-7848 (1996).

184. K. B. Møller, N. E. Henriksen, and A. H. Zewail, "On the role of coherence in the transition from kinetics to dynamics: Theory and application to femtosecond unimolecular reactions," J. Chem. Phys. **113**, 10477-10485 (2000).

185. J. Wang, A. J. Blake, D. G. McCoy, and L. Torop, "Analytical potential curves for the X $1\Sigma^+$ and 0^+ states of NaI," Chem.Phys. Lett. **175**, 225-230 (1990).

186. C. Meier, V. Engel, and J. S. Briggs, "Long time wave packet behavior in a curve-crossing system: The predissociation of NaI," J. Chem. Phys. **95**, 7337-7343 (1991).

187. A. B. Alekseyev, H.-P. Liebermann, R. J. Buenker, N. Balakrishnan, H. R. Sadeghpour, S. T. Cornett, and M. J. Cavagnero, "Spin–orbit effects in photodissociation of sodium iodide," J. of Chem. Phys. **113**, 1514-1523 (2000).

188. W. S. Kim, H. S. Choi, B. C. Nam, E. O. Chi, K. W. Lee, and N. H. Hur, "Effect of subsidiary phase on the magnetic and transport properties of $Sr1_{.6}La_{1.4}Mn_2O_7$," Physica status solidi (a) **185**, 401-411 (2001).

189. C. Kumar Modal and S. P. Bhattacharyya, "Time-dependent Fourier grid Hamiltonian method for studying the curve crossing dynamics: Dynamics of predissociation of NaI," Int. J. Quantum Chem. **88**, 310-316 (2002).

190. D. M. Koch, Q. K. Timerghazin, G. H. Peslherbe, B. M. Ladanyi, and J. T. Hynes, "Nonadiabatic Trajectory Studies of NaI (H_2O)n Photodissociation Dynamics," J. Phys. Chem. A **110**, 1438-1454 (2006).

191. Q. K. Timerghazin, D. M. Koch, and G. H. Peslherbe, "Accurate ab initio potential for the Na+···I• complex," J. Chem. Phys. **124**, 034313 (2006).

192. B. Xu, J. M. Gunn, J. M. D. Cruz, V. V. Lozovoy, and M. Dantus, "Quantitative investigation of the multiphoton intrapulse interference phase scan method for simultaneous phase measurement and compensation of femtosecond laser pulses," J. Opt. Soc. Am. B **23**, 750-759 (2006).

193. V. V. Lozovoy, I. Pastirk, K. A. Walowicz, and M. Dantus, "Multiphoton intrapulse interference. II. Control of two- and three-photon laser induced fluorescence with shaped pulses," J. Chem. Phys. **118**, 3187-3196 (2003).

194. H. J. Werner and P. J. Knowles, "An efficient internally contracted multiconfiguration–reference configuration interaction method," J. Chem. Phys. **89**, 5803-5814 (1988).

195. P. J. Knowles and H.-J. Werner, "An efficient method for the evaluation of coupling coefficients in configuration interaction calculations," Chem. Phys. Lett. **145**, 514-522 (1988).

196. P. J. Knowles and H.-J. Werner, "Internally contracted multiconfiguration-reference configuration interaction calculations for excited states," Theoretica chimica acta **84**, 95-103 (1992).

197. K. Ruedenberg, M. W. Schmidt, M. M. Gilbert, and S. T. Elbert, "Are atoms intrinsic to molecular electronic wavefunctions? I. The FORS model," Chem. Phys. **71**, 41-49 (1982).

198. B. O. Roos, "The complete active space self-consistent field method and its applications in electronic structure calculations," in *Advanced Chemical Physics* (John Wiley & Sons, Inc., 2007), pp. 399-445.

199. B. P. Prascher, D. E. Woon, K. A. Peterson, T. H. Dunning, and A. K. Wilson, "Gaussian basis sets for use in correlated molecular calculations. VII. Valence, core-valence, and scalar relativistic basis sets for Li, Be, Na, and Mg," Theor. Chem. Acc. **128**, 69-82 (2011).

200. J. W. Cooley, "An improved eigenvalue corrector formula for solving the Schrödinger equation for central fields," Math. Comp. **15**, 363-374 (1961).

201. R. J. Le Roy, "LEVEL: A computer program for solving the radial Schrödinger equation for bound and quasibound levels," J. Quant. Spectros. Radia. Transfer **186**, 167-178 (2017).

202. J. P. Burg, "Maximum entropy spectral analysis," in Modern Spectrum Analysis, edited by D. G. Childers, IEEE Press Selected Reprint Series (Wiley, 1978), pp. 34-41.

203. R. S. Berry, "Interaction of vibrational and electronic motion in alkali halide molecules," J. Chem. Phys. **27**, 1288-1295 (1957).

204. J. Lindner, H. Bluhm, A. Fleisch, and E. Tiemann, "Low vibrational levels of the ionic–covalent coupled state $A0^+$ of NaI and its potential function," Can. J. Phys. **72**, 1137-1144 (1994).

205. U. Lev, L. Graham, C. B. Madsen, I. Ben-Itzhak, B. D. Bruner, B. D. Esry, H. Frostig, O. Heber, A. Natan, V. S. Prabhudesai, S. Schwalm, Y. Silberberg, D. Strasser, I. D. Williams, and D. Zajfman, "Quantum control of photodissociation using intense, femtosecond pulses shaped with third order dispersion," J. Phys. B: At. Mol. Opt. Phys. **48** (2015).